UNIVERSITAT POLITÈCNICA DE CATALUNYA BARCELONATECH

DOCTORAL THESIS

Multirate mass transfer and biofilm growth modeling in porous media

*Author:*Jingjing Wang

Supervisors: Prof. Jesús Carrera Ramírez
Prof. Maarten Willem Saaltink
Dr. Cristina Valhondo

A thesis submitted for the degree of Doctor of Philosophy in Geotechnical Engineering, Department of Civil and Environmental Engineering, Universitat Politecnica de Catalunya (UPC)

June, 2021

Barcelona, Spain

The author would like to acknowledge the financial support of the project NITREM (NITrogen REMoval from waste rock) initiated and funded by EIT (European Institute of Innovation and Technology), and the Water-JPI European Union project MARadentro.

Acknowledgements

The PhD thesis has been a challenging experience for me. Not only my academic research in Geoscience, but also my life abroad. During the four years, I would like to express my thanks for the people mentioned below, without them I won't be able to finish my thesis.

First of all, I would like to express my heartfelt gratitude to my supervisor Jesús Carrera. I would like to thank Jesús for providing me the opportunity to achieve my PhD in Spain, for trusting me in the research topic, giving me unconditional support and encouragement during the whole process. Without his support, I won't have the chance to achieve my PhD career. For me he is not only my supervisor, but also my friend and family.

I would like to acknowledge the role of my advisor Maarten Saaltink. Thanks for his responsible guidance and participate in each discussion. For this, I respect and love him lots. I would also like to thank my co-supervisor Cristian Valhondo. It's her independence, sense of responsibility and excellent ability that inspires me to perform well in the face of challenges.

I would like to thank the people in Groundwater Hydrology Group (UPC, IDAEA-CSIC). They are excellent researchers and kind friends. I would like to specially thank the former and current members of the group that have helped me in one way or another. Thanks the people in office 1428, Alba, Quim, Rotman, Sonia, Nacho, Pedro. Thanks my friends Andrea and Tybaud for going through the PhD experience together, we witness the growth of each other, and we all achieve the PhD. Thanks the friends I have known in CSIC Alessandro, Vivien, Alec, Lazaro, Tomas, Silvia, Kevin, Miguel, Carolina, Robert, Francesco, Jordi, Julia, Berta, Yoar, Laura, S., Laura M., Lidia, Lucia, Ashkan, Ahmad, Max, Jiaqi, Joan, Sara, Carlos, Marco, Juan, Enric, Jordi, Josep. Thanks the people in UPC Michela, Laura V. A., Sonia, Oriol, Arnau, Guillem, Paula, Lurdes, Xavier, Daniel, Albert. I would especially like to thank Tere for her help in my living and working in Barcelona.

I would also like to thank the experiences through my PhD. Thanks the training courses I have attended, including the 4th Cargèse summer school: flow and transport in porous and fractured media, the short course of applied reactive transport modelling (Bordeaux, France), and the short course of reactive transport in natural and engineered systems (Barcelona, Spain). Thanks the international conferences I have attended, including the EGU general assembly (Vienna, Austria), the Goldschmidt (Barcelona, Spain) and InterPore 2021 online (Edinburgh, United Kingdom). These experiences promote me to be more professional on my research topic.

Finally, I would like to thank my family and friends in China for their love, encouragement and support. Thanks for every video and voice call that we have had on WeChat. A special thanks to myself for my persistence, brave and endeavor on the way of my PhD. These impressive experience promote my maturity and growth both in my life and research work.

To my family

Abstract

Reactive transport modeling is a methodological tool to study the coupled physical, chemical and biological processes in Earth system. It is complex not only because of the nature of the equations, but also because of the effects of the porous medium heterogeneity on reactive transport. This thesis aims to deepen the understanding of reactive transport processes in order to explain the biochemical degradation process in porous media, with special emphasis on the role of biofilm and its growth.

First, we propose a general and efficient numerical solution of reactive transport in multicontinuum media using Multirate Mass Transfer (MRMT) approach. To overcome the non-linearity of the problem, induced by non-linear kinetics, we use the Newton-Raphson method to get the global solution. We solve the system of equations in block form, which allow us to reduce the unknowns to those of mobile zones and to, thus improving efficiency. The solution is validated by comparison with analytical solution for linear kinetics. The code is developed in Object-oriented way, which enables the code reusability and data polymorphism.

Second, we investigate the conditions for chemical localization (i.e., the occurrence of reactions that would not be possible in single continuum media). To this end, we write the multicontinuum transport equations in dimensionless form to find that reactive transport in multicontinuum media is governed by three characteristic times: the distribution of residence times in immobile zones, and the characteristic reaction and transport times. To study the interplay between these three characteristic times, we simulate three chemical systems: conservative, single reaction and sequential reaction. Results demonstrate that reactions driven by species that result from previous reactions will localize in immobile zones whose residence time is comparable to reaction times. Furthermore, immobile zones with residence times much smaller than those for transport can be lumped together (assuming that very fast reactions are assumed in equilibrium), which greatly reduces computations.

Third, we perform simulations of reactive transport incorporating biochemical reactions that not only oxidize organic carbon, but also produce biomass, thus causing biofilm growth. Biofilm growth is known to cause clogging (i.e., reduction of permeability), which has concentrated most research on the topic. But it also causes a significant change in the pore space geometry and connectivity, which leads to not only an overall increase in mean residence time in immobile regions, but also on its distribution. As discussed above, this is critical to (bio)chemical localization, especially considering that microbial mediated reactions tend to concentrate in biofilms. We propose a model for the evolution of residence time distribution in immobile zones in response to biofilm growth. We test this model by comparison with laboratory experiments extracted from the literature, where tracer tests have been performed at various stages of growth. Results show that the dynamic MRMT model is capable of reproducing the salient features of these experiments.

Resumen

El modelado de transporte reactivo es una herramienta metodológica para estudiar los procesos físicos, químicos y biológicos acoplados en el sistema terrestre. Es complejo no solo por la naturaleza de las ecuaciones, sino también por los efectos de la heterogeneidad del medio poroso sobre el transporte reactivo. Esta tesis tiene como objetivo profundizar en el conocimiento de los procesos de transporte reactivo para explicar el proceso de degradación bioquímica en medios porosos, con especial énfasis en el papel del biofilm y su crecimiento.

En primer lugar, proponemos una solución numérica general y eficiente de transporte reactivo en medios multicontinuum utilizando el enfoque de Transferencia de Masa Multivelocidad (MRMT). Para superar la no linealidad del problema, inducida por una cinética no lineal, utilizamos el método de Newton-Raphson para obtener la solución global. Resolvemos el sistema de ecuaciones en forma de bloque, lo que nos permite reducir las incógnitas a las de zonas móviles y a, mejorando así la eficiencia. La solución se valida por comparación con la solución analítica para cinética lineal. El código se desarrolla de forma orientada a objetos, lo que permite la reutilización del código y el polimorfismo de los datos.

En segundo lugar, investigamos las condiciones para la localización química (es decir, la ocurrencia de reacciones que no serían posibles en un medio continuo único). Con este fin, escribimos las ecuaciones de transporte multicontinuum en forma adimensional para encontrar que el transporte reactivo en medios multicontinuum se rige por tres tiempos característicos: la distribución de los tiempos de residencia en zonas inmóviles, y los tiempos de reacción y transporte característicos. Para estudiar la interacción entre estos tres tiempos característicos, simulamos tres sistemas químicos: conservador, reacción única y reacción secuencial. Los resultados demuestran que las reacciones impulsadas por especies que resultan de reacciones previas se localizarán en zonas inmóviles cuyo tiempo de residencia es comparable a los tiempos de reacción. Además, las zonas inmóviles con tiempos de residencia mucho más pequeños que los de transporte pueden agruparse (asumiendo que se asumen reacciones muy rápidas en equilibrio), lo que reduce en gran medida los cálculos.

En tercer lugar, realizamos simulaciones de transporte reactivo incorporando reacciones bioquímicas que no solo oxidan el carbono orgánico, sino que también producen biomasa, lo que provoca el crecimiento de biopelículas. Se sabe que el crecimiento de biopelículas causa obstrucciones (es decir, reducción de la permeabilidad), lo que ha concentrado la mayor parte de la investigación sobre el tema. Pero también provoca un cambio significativo en la geometría del espacio poroso y la conectividad, lo que conduce no solo a un aumento general del tiempo medio de residencia en las regiones inmóviles, sino también a su distribución. Como se discutió anteriormente, esto es crítico para la localización (bio) química, especialmente considerando que las reacciones mediadas por microbios tienden a concentrarse en biopelículas. Proponemos un modelo para la evolución de la distribución del tiempo de residencia en zonas inmóviles en respuesta al crecimiento de biopelículas. Probamos este modelo comparándolo con experimentos de laboratorio extraídos de la literatura, donde se han realizado pruebas de trazadores en varias etapas de crecimiento. Los resultados muestran que el modelo MRMT dinámico es capaz de reproducir las características más destacadas de estos experimentos.

Resum

La modelització del transport reactiu és una eina metodològica per estudiar els processos físics, químics i biològics acoblats en el sistema terrestre. És complex no només per la naturalesa de les equacions, sinó també pels efectes de l'heterogeneïtat mitjana porosa sobre el transport reactiu. Aquesta tesi té com a objectiu aprofundir en la comprensió dels processos de transport reactiu per explicar el procés de degradació bioquímica en medis porosos, amb especial èmfasi en el paper del biofilm i el seu creixement.

En primer lloc, proposem una solució numèrica general i eficient de transport reactiu en medis multicontinuos mitjançant l'enfocament de transferència de massa multirata (MRMT). Per superar la no linealitat del problema, induïda per cinètiques no lineals, fem servir el mètode de Newton-Raphson per obtenir la solució global. Resolem el sistema d'equacions en forma de blocs, que ens permeten reduir les incògnites a les de les zones mòbils i a, millorant així l'eficiència. La solució es valida comparant-la amb una solució analítica de cinètica lineal. El codi es desenvolupa de manera orientada a objectes, que permet la reutilització del codi i el polimorfisme de dades.

En segon lloc, investigem les condicions per a la localització química (és a dir, l'aparició de reaccions que no serien possibles en un mitjà continu). Amb aquest objectiu, escrivim les equacions de transport multicontinu en forma adimensional per trobar que el transport reactiu en mitjans multicontinuos es regeix per tres temps característics: la distribució dels temps de residència en zones immòbils i els temps de reacció i transport característics. Per estudiar la interacció entre aquests tres temps característics, simulem tres sistemes químics: conservador, de reacció única i reacció seqüencial. Els resultats demostren que les reaccions impulsades per espècies que resulten de reaccions anteriors es localitzaran en zones immòbils el temps de residència és comparable als temps de reacció. A més, les zones immòbils amb temps de residència molt menors que les del transport es poden agrupar (suposant que s'assumeixen reaccions molt ràpides en equilibri), cosa que redueix considerablement els càlculs.

En tercer lloc, realitzem simulacions de transport reactiu que incorporen reaccions bioquímiques que no només oxiden el carboni orgànic, sinó que també produeixen biomassa, provocant així el creixement del biofilm. Se sap que el creixement del biofilm causa l'obstrucció (és a dir, la reducció de la permeabilitat), que ha concentrat la majoria de les investigacions sobre el tema. Però també provoca un canvi significatiu en la geometria i la connectivitat de l'espai dels porus, que condueix no només a un augment global del temps mitjà de residència en regions immòbils, sinó també a la seva distribució. Com s'ha comentat anteriorment, això és fonamental per a la localització (bio) química, sobretot tenint en compte que les reaccions mediàtiques microbianes tendeixen a concentrar-se en biofilms. Proposem un model per a l'evolució de la distribució del temps de residència en zones immòbils en resposta al creixement del biofilm. Provem aquest model en comparació amb experiments de laboratori extrets de la literatura, on s'han realitzat proves de traçador en diverses etapes de creixement. Els resultats mostren que el model dinàmic MRMT és capaç de reproduir les característiques més destacades d'aquests experiments.

摘要

反应运移模型是地球系统中研究物理、化学和生物耦合过程的一种方法工具。反应运移是复杂的，不仅在于其控制方程本身的复杂性，而且受多孔介质非均质性的影响。本论文旨在加深对反应运移过程的理解，以解释多孔介质中的生物化学降解过程，尤其是生物膜的生长及其作用。

首先，我们利用多速率传质(MRMT)方法提出了多连续介质中反应运移的一种通用且高效的数值解。为克服非线性动力学反应导致问题的非线性，我们采用牛顿-拉夫森方法迭代求得全局解。利用分块的形式求解方程组，将未知量的个数减少为可移动区域的个数，从而提高计算效率。通过与线性动力学解析解的比较，验证了该方法的正确性。采用面向对象的方式开发程序，实现了代码的可重用性和数据多态性。

其次，我们研究了局部化学反应的条件，即在单一连续介质中不可能发生的反应的发生。为此，我们推导了多连续介质中的反应运移方程的无量纲形式，发现多连续介质中的反应运移受控于三个特征时间:不可移动区停留时间的分布，反应时间和运移时间。为研究这三种特征时间之间的相互作用，我们模拟了三种化学体系:保守反应、单反应和顺序反应。结果表明，由前一的反应导致的物种驱动的反应将定位于停留时间与反应时间相当的不可移动区域。此外，可将停留时间比运移时间小的多的不可移动区域视作可移动区域（假设非常快的反应处于平衡状态），从而很大的减少了计算。

最后，我们模拟了有微生物参与的反应运移，涉及的生物化学反应不仅能够氧化有机碳，而且能够为微生物的生长提供碳源，从而导致生物膜的生长。众所周知，生物膜的生长会导致生物堵塞（即渗透性的降的），大多研究致力于该方向。但生物膜的生长也会导致孔隙几何形状和连通性发生显著变化，不仅导致不可移动区域平均停留时间的增加，而且改变其分布。如上所述，这对于研究局部（生物）化学过程至关重要，特别是在考虑微生物介导的反应时，其往往集中在生物膜中。我们提出了一个停留时间在不可移动区域中随生物膜生长的演化模型。通过与文献中提取的实验数据进行对比，在生长的不同阶段进行示踪实验，来测试该模型。结果表明，该模型能够较好地再现实验的显著性特征。

Contents

List of figures

List of tables

1 Introduction

This thesis is motivated by projects dealing with water renationalization by Soil Aquifer treatment (SAT) and degradation processes in the subsurface.

The hydrogeology research group has worked recently on a methodology to enhance water quality improvement processes during soil passage (Valhondo et al., 2020). The approach consists of installing a reactive barrier at the bottom of infiltration basins in SAT system to favor the adsorption of organic pollutants and their degradation. To this end, the reactive barrier consists of a mixture of sand (to ensure high permeability and to guarantee structural strength), organic matter (woodchips or vegetable compost, to provide sorption sites for neutral compounds and as a source of organic carbon to promote reducing conditions), clay (to provide sorption sites for cationic compounds). Ideally, having a broad range of sorption sites and redox conditions should ensure the removal of most organic contaminants. Many of them hardly degrade under aerobic conditions, but require reducing conditions (Christensen et al., 2001).

Another type of application is the removal of nitrates from mine tailing's seepage. An efficient passive technology to reduce nitrate concentration consists of circulating the nitrate loaded water through a tank containing woodchips, which ensures denitrification conditions (Nordström et al., 2021; Nordström & Herbert, 2019; Nordström & Herbert, 2018; Nordström & Herbert, 2017).

Both approaches have been successfully tested in the field (Nordström et al., 2021; Valhondo et al., 2020; Valhondo, Martínez-Landa, et al., 2020; Nordström & Herbert, 2018; Valhondo et al., 2018). However, quantitative interpretation of results is difficult because degradation reactions occur in the biofilm, which evolves overtime. Microbial communities grow, which causes degradation rates to take place more efficiently, but also risks clogging. Quantitative interpretation of results is required for proper understanding and for upscaling observation from pilot to large scale and from relatively short (2 years) to long term operation.

Quantitative interpretation is made by means of numerical models, which is challenging for several reasons. First, degradation reactions take place within the biofilm, which hosts the vast majority of microorganisms (Flemming et al., 2007; Morales et al., 2010; Flemming & Wingender, 2010; Satpathy et al., 2016; Flemming & Wuertz, 2019; Wu et al., 2019), but where water does not flow (Costerton et al., 1995; Flemming et al., 2007; Flemming & Wingender, 2010). Obviously, mobile-immobile representations of porous media are required. Many such representations are available (Le Borgne et al., 2008). But such representations are primarily motivated to reproduce the impact of heterogeneity, which leads to a broad range of residence times because of the variability of water velocity in different flow paths, but not necessarily because of the time it takes to reach actual immobile zones. Second, as a result of the above, the experience about simulating reactive transport in this kind of model representations is limited (Donado et al., 2009; Willmann et al., 2010). Worse, the computational demand increases dramatically because the number of unknowns is multiplied by the number of immobile zones used for representing the broad range of residence times. This may lead to computationally unfeasible problems when the chemical system is complex. And, third, these immobile regions evolve in time as a result of biofilm growth. Many studies exists on Its effect on hydrological parameters, such as permeability, porosity and retention curve (e.g., Taylor et al., 1990; Morales et al., 2010; Carles Brangarí et al., 2017; Lopez-Peña et al., 2019). Its effects on the parameters controlling mass exchange between mobile and immobile zones have been studied and modelled much less.

To address these challenges, I have opted for a multi-rate-mass-transfer (MRMT) approach (Haggerty & Gorelick, 1995;), because it localizes chemical data, thus making it possible to use conventional chemical calculation tools, which I have also developed as part of the thesis. In this context, I have made several contributions. Each of them is described in one chapter, which will hopefully be published. This implies that every chapter can be read independently, but also that a portion of the mathematical description is repeated in every chapter.

Chapter 2 contains a new method to solve MRMT problems. The method benefits from the fact that immobile zones are connected to independent mobile nodes. This leads to a highly sparse system matrix, which facilitates solution. In fact, the final system only contains the mobile zone concentrations because immobile zones concentrations are expressed as a function of mobile zone concentrations. The resulting algorithm is very fast.

Chapter 3 analyses the interplay of immobile zones residence times, transport time and reaction times with two goals: first, to minimize the number of immobile zones, and second, to identify the conditions for chemical localization (i.e., the occurrence of reactions that would not take place if all the water was mobile).

Finally, Chapter 4 contains a proposal for biofilm growth. To date, biofilm growth models emphasize clogging (i.e., the reduction of permeability as the pore space becomes filled by biofilm. Here, I emphasize that the residence time distribution changes in response to biofilm growth. This change is relevant for proper representation of the evolution of redox states that occur both during artificial recharge across a reactive barrier and during flow through a woodchips porous medium, which motivated this thesis.

2 A general and efficient numerical solution of reactive transport with multirate mass transfer *

The presence of low permeability regions within porous media impacts solute transport and the distribution of species concentrations. Therefore, (bio)chemical reactions are equally affected. Multirate Mass Transfer (MRMT) models can be used to represent this anomalous transport process. MRMT conceptualizes the medium as a set of multiple continua: one mobile zone and multiple immobile zones. It simulates species transport in mobile and immobile zones simultaneously, which are related by first-order mass exchange. Numerical modeling of reactive transport in this kind of multicontinua media is complex and demanding because of the high dimensionality of the problem. In this paper, we establish the governing equations of reactive transport in multicontinuum media incorporating chemical kinetics into the governing equations. We propose a general numerical solution of reactive transport with MRMT by applying direct substitution approach (DSA) based on Newton-Raphson method. The efficiency of the proposed algorithm benefits of the block structure of the system, which allows us to eliminate immobile zones equations and leads to significant savings in CPU time. We test the validity of the developed solution by comparison with other numerical and analytical solutions.

* This chapter is based on the paper Wang et al., 2021. A general and efficient numerical solution of reactive transport with multirate mass transfer, submitted to *Computers & Geosciences*, under 2-nd review.

2.1 Introduction

Solute transport is often anomalous in the sense that observed concentrations display numerous non-Fickian features, such as asymmetric spatial distributions or heavy tailed break-through curves (BTCs) (Kosakowski et al., 2001; Zinn et al., 2004; Zhang et al., 2007; Le Borgne & Gouze, 2008). Many methods have been developed to address anomalous transport, including continuous time random walk (CTRW) (Berkowitz & Scher, 1998; Dentz et al., 2004; Cortis & Berkowitz, 2004; Dentz et al., 2015), fractional advection-dispersion equations (FADE) (Benson et al., 2000; Schumer et al., 2003; Marseguerra & Zoia, 2008), memory functions (Carrera et al., 1998; Haggerty et al., 2000; Willmann et al., 2008; Gouze et al., 2008a), multiple interacting continua (MINC) (Pruess & Narasimhan, 1985; De Dreuzy et al., 2013), structured interacting continua (SINC) (Babey et al., 2015; Rapaport et al., 2017), multirate mass transfer (MRMT) (Haggerty and Gorelick, 1995; Wang et al., 2005; Salamon et al., 2006; Benson & Meerschaert, 2009), and others. These methods are essentially equivalent (Dentz & Berkowitz, 2003; Silva et al., 2009) in that they can be viewed as representing solute mass exchange between a mobile zone and several immobile zones with negligible water velocity. The above references demonstrate that all these methods are relevant for realistic solute transport, which is a pre-condition for realistic reactive transport. But MRMT, MINC and SINC are advantageous because they localize concentrations. That is, concentrations are computed and available at mobile and immobile zones at each point in space, which facilitates reactive calculations. In this study we use MRMT for its simplicity and generality, but our results can be relevant as well for MINC and SINC.

MRMT consists of viewing the medium as the superposition of mobile and immobile zones (Figure 2.1a). Typically, the immobile zones represent areas where water does not flow or flows very slowly. Numerous (actually a distribution of) immobile zones are needed to reproduce the distribution of residence time in the immobile regions. Numerical solutions can be viewed as adding extra nodes to every mobile node (Figure 2.1b).

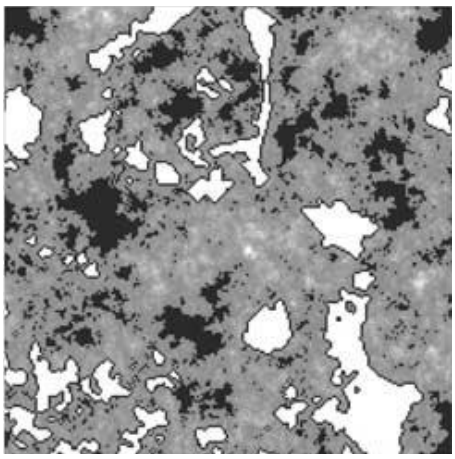

(a)

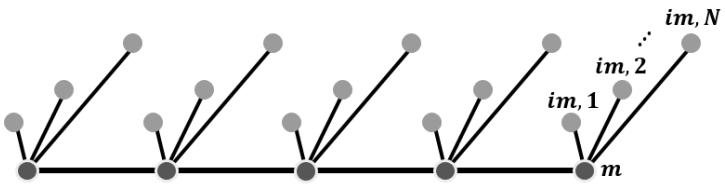

(b)

Figure 2.1 (a) Illustration of MRMT model in porous media, white areas bounded by black curves represent mobile zone, the black areas represent solid matrix, and the gray areas represent immobile zones, dark gray corresponding to a lower possibility of visit, while light gray denotes a higher

possibility to visit (Gouze et al., 2008b). (b) Numerical discretization of mobile and immobile zones, each circle (labelled m for mobile, and im for immobile) is a node.

MRMT or any other method to address anomalous transport is relevant for a broad range of reactive transport problems. A clear example is reactive transport in fractured media (see Deng & Spycher, 2019, for a review). Groundwater flow in fractures is much higher than in the rock matrix. Mass transfer between the fracture and the matrix is by molecular diffusion and can lead to mineral- dissolution-precipitation depending on the distance or connection to the fracture. Another important example is mass exchange between pore water and biofilms (e.g., Chen-Charpentier, 1999; Tiwari & Bowers, 2001; Gaebler & Eberl, 2018; Brangarí et al., 2018). Biological reactions mainly take place in biofilms composed of cellular material and extracellular polymeric substances (EPS). As hydraulic conductivity of biofilms is very low, mass transfer is controlled by diffusion and shape and size of the biofilm.

A broad range of residence times may be relevant in many reactive transport problems. Simulating them is relevant not only for proper reproduction of (conservative tracers) breakthrough curves, but also for reproducing geochemical localization (Soler-Sagarra et al., 2016). Localization refers to reactions that occur in some portions of the domain, but which would not occur with the concentrations averaged over all portions of the domain (i.e., in single porosity models). General reactive transport codes must be coupled to MRMT to simulate these problems.

MRMT is computationally costly because it involves multiplying the number of unknowns by the number of immobile zones plus one. This is especially true for implicit solvers, which require building a system of equations with size equal to the number of unknowns. Therefore, it is not surprising that developers have sought "tricks" to reduce this cost. The types of tricks depend on the method. One option is to solve diffusion into the immobile region and then perform a convolution to acknowledge the time variability of concentrations in the mobile zone (Carrera et al., 1998; Wang et al., 2005; Silva et al., 2009). This is tedious, so many others (Haggerty & Gorelick, 1995; Berkowitz et al., 2006; Berkowitz et al., 2008) propose using a Laplace transform, which transforms the convolution into a regular product. But these tricks require that the transport problem is linear. Therefore, they would not be valid for general non-linear reactive transport.

MRMT is still feasible if all reactions are fast (i.e., simulated as equilibrium reactions) and identical because transport of components is linear (Donado et al., 2009; Willmann et al., 2010). However, MRMT is most important for reactive transport problems with kinetic reactions, because of both the broad range of residence times (Haggerty et al., 2000) and chemical localization (Soler-Sagarra et al., 2016).

However, solving MRMT for general reactive transport including kinetics cannot take advantage of the above "tricks". It needs to be solved in the way in Figure 2.1b by using general purpose codes, such as PFLOTRAN (Lichtner et al., 2015; Hammond et al., 2014; Iraola et al., 2019), OpenGeoSys (Olaf Kolditz et al., 2012; O. Kolditz et al., 2012; Bilke et al., 2019), PHREEQC (Parkhurst & Appelo, 2013), CrunchFlow (Steefel et al., 2015; Beisman et al., 2015), CHEPROO (Bea et al., 2009), Retraso (Saaltink et al., 2004) and PHT3D (Prommer et al., 2001; Prommer et al., 2003; Steefel et al., 2015), which is costly. Therefore, it would be desirable to have a general, yet efficient method to solve reactive transport with MRMT.

The objective of this paper is to propose an accurate and efficient numerical approach of MRMT for general reactive transport. In part one, we establish the mathematical governing equations. In part two, we formulate the traditional and proposed numerical solutions. In part three, we verify the accuracy of proposed formulation by comparing with the traditional one and available analytical solutions. We also analyze the efficiency of the proposed algorithm.

2.2 Governing Equations

The immobile zones are fully defined by the distribution of mass exchange rates between mobile and immobile zones. $f(\alpha)$ is the probability density of immobile zones that transfer mass at a given exchange rate α (Haggerty et al., 2000).

The total concentration $\boldsymbol{c}(x,t)$ (i.e., mass of solute per unit volume of medium) at a given point is the weighted sum of mobile $\boldsymbol{c}_m(x,t)$ and immobile $\boldsymbol{c}_{im}(x,\alpha,t)$ concentrations, written as

$$\boldsymbol{c}(x,t) = \phi_m \boldsymbol{c}_m(x,t) + \phi_{im} \int_0^\infty f(\alpha)\boldsymbol{c}_{im}(x,\alpha,t)\, d\alpha \tag{2.1}$$

where ϕ_m and ϕ_{im} are porosity of mobile zone and porosity of immobile zone, respectively. As we deal with reactive transport with several chemical species and reactions, $\boldsymbol{c}$, $\boldsymbol{c}_m$ and $\boldsymbol{c}_{im}$ are vectors containing the concentrations of several species.

The governing mass balance equation to simulate species transport in mobile zone is defined as follows (Willmann et al., 2008)

$$\phi_m \frac{\partial \boldsymbol{c}_m(x,t)}{\partial t} = L_t[\boldsymbol{c}_m(x,t)] - \phi_{im} \int_0^\infty \alpha[\boldsymbol{c}_m(x,t) - \boldsymbol{c}_{im}(x,\alpha,t)] f(\alpha)\, d\alpha + \phi_m \boldsymbol{r}_m(x,t) \tag{2.2}$$

where $L_t[\boldsymbol{c}_m(x,t)] = -\boldsymbol{q}\nabla \boldsymbol{c}_m + \nabla \cdot (\phi_m \boldsymbol{D} \nabla \boldsymbol{c}_m)$ is the transport operator, which accounts for advection and dispersion, $\boldsymbol{D}$ is the dispersion and diffusion tensor, $\boldsymbol{q}$ is Darcy flux, $\boldsymbol{r}_m(x,t)$ is a vector of sink-source term that represents the mass added or removed by chemical reactions in mobile zone per unit volume of water per unit time.

Mass in immobile zones exchange with the mobile zone as

$$\frac{\partial \boldsymbol{c}_{im}(x,\alpha,t)}{\partial t} = \alpha[\boldsymbol{c}_m(x,t) - \boldsymbol{c}_{im}(x,\alpha,t)] + \boldsymbol{r}_{im}(x,\alpha,t) \tag{2.3}$$

Different distributions can be used for the mass exchange rate α. The (truncated-) power law distribution (Haggerty et al., 2000; Haggerty et al., 2002; Schumer et al., 2003; Benson & Meerschaert, 2009) is commonly used. Integrating equation (2.3) with weight $f(\alpha)$ in terms of $d\alpha$, and multiplying by ϕ_{im}, then adding it into equation (2.2), yields the governing equation for the total concentrations,

$$\phi_m \frac{\partial \boldsymbol{c}_m(x,t)}{\partial t} + \phi_{im} \int_0^\infty f(\alpha) \frac{\partial \boldsymbol{c}_{im}(x,\alpha,t)}{\partial t} d\alpha = L_t[\boldsymbol{c}_m(x,t)] + \boldsymbol{r}(x,t) \tag{2.4}$$

in which, $\boldsymbol{r}(x,t)$ is the total reaction rate (now per unit volume of porous medium) that integrates reaction in both mobile and immobile zones,

$$\boldsymbol{r}(x,t) = \phi_m \boldsymbol{r}_m(x,t) + \phi_{im} \int_0^\infty f(\alpha)\boldsymbol{r}_{im}(x,\alpha,t)\, d\alpha \tag{2.5}$$

For any chemical system, reaction rates $\boldsymbol{r}(x,t)$ at any point can be written as,

$$\boldsymbol{r}(x,t) = \boldsymbol{S}_e^T \boldsymbol{r}_e(x,t) + \boldsymbol{S}_k^T \boldsymbol{r}_k(x,t) \tag{2.6}$$

where $\boldsymbol{S}_e$ and $\boldsymbol{S}_k$ are the stoichiometric matrices describing equilibrium and kinetic reactions respectively, $\boldsymbol{r}_e$ and $\boldsymbol{r}_k$ represent the vectors of reaction rates (Saaltink et al., 1998).

The component matrix $\boldsymbol{U}$ is introduced to eliminate equilibrium reactions in equation (2.6), and to reduce the number of unknowns (Saaltink et al., 1998; Molins et al., 2004). $\boldsymbol{U}$ is the kernel of $\boldsymbol{S}_e^T$, satisfying $\boldsymbol{U}\boldsymbol{S}_e^T = \boldsymbol{0}$. Multiply equation (2.2) and (2.3) by component matrix $\boldsymbol{U}$, we obtain the simplified governing equation in terms of components that is written as,

$$\phi_m \frac{\partial \boldsymbol{u}_m(x,t)}{\partial t} = L_t[\boldsymbol{u}_m(x,t)] - \phi_{im} \int_0^\infty \alpha[\boldsymbol{u}_m(x,t) - \boldsymbol{u}_{im}(x,\alpha,t)] f(\alpha)\, d\alpha + \phi_m \boldsymbol{U}\boldsymbol{S}_k^T \boldsymbol{r}_{k,m}(x,t) \tag{2.7}$$

$$\frac{\partial \boldsymbol{u}_{im}(x,\alpha,t)}{\partial t} = \alpha[\boldsymbol{u}_m(x,t) - \boldsymbol{u}_{im}(x,\alpha,t)] + \boldsymbol{U}\boldsymbol{S}_k^T \boldsymbol{r}_{k,im}(x,\alpha,t) \tag{2.8}$$

where component vector $\boldsymbol{u} = \boldsymbol{U}\boldsymbol{c}$ is the product of component matrix and concentration vector.

2.2.1 Numerical Equations

We solve the non-linear coupled reactive transport governing equation (2.7) and (2.8) by applying Newton-Raphson method, i.e., direct substitution approach (DSA) (Steefel & Lasaga, 1994; Saaltink et al., 1998; Saaltink et al., 2001; Molins et al., 2004; Liu et al., 2019). Therefore, we define the system equations in both mobile and immobile zones simultaneously. The details are given in Appendix A. To explain the algorithm, we write the equation system in the form $\boldsymbol{g}(\boldsymbol{x}) = 0$:

$$\boldsymbol{g}_m = \phi_m \frac{\partial \boldsymbol{u}_m(x,t)}{\partial t} - L_t[\boldsymbol{u}_m(x,t)] + \sum_{j=1}^{N} \boldsymbol{F}_j - \phi_m \boldsymbol{r}_m(x,t) = 0 \tag{2.9}$$

$$\boldsymbol{g}_{im,j} = \frac{\partial \boldsymbol{u}_{im,j}(x,t)}{\partial t} - \alpha_j\left[\boldsymbol{u}_m(x,t) - \boldsymbol{u}_{im,j}(x,t)\right] - \boldsymbol{r}_{im,j}(x,t) = 0, \qquad j = 1, \cdots, N \tag{2.10}$$

where N is the number of immobile zones for each nodes and $\boldsymbol{F}_j$ is the exchange rate between mobile and immobile zone.

The Newton-Raphson method is based on solving the linearized form of the equations, i.e.,

$$\boldsymbol{g}^{i+1} = \boldsymbol{g}\left(\boldsymbol{x}^{i+1}\right) \approx \boldsymbol{g}\left(\boldsymbol{x}^{i}\right) + \frac{\partial \boldsymbol{g}(\boldsymbol{x})}{\partial \boldsymbol{x}}\left(\boldsymbol{x}^{i+1} - \boldsymbol{x}^{i}\right) = 0 \tag{2.11}$$

In our case, this can be written as,

$$\begin{bmatrix} \left(\frac{\partial \boldsymbol{g}_m}{\partial \boldsymbol{u}_m^{k+1}}\right)^i & \left(\frac{\partial \boldsymbol{g}_m}{\partial \boldsymbol{u}_{im,1}^{k+1}}\right)^i & \cdots & \left(\frac{\partial \boldsymbol{g}_m}{\partial \boldsymbol{u}_{im,N}^{k+1}}\right)^i \\ \left(\frac{\partial \boldsymbol{g}_{im,1}}{\partial \boldsymbol{u}_m^{k+1}}\right)^i & \left(\frac{\partial \boldsymbol{g}_{im,1}}{\partial \boldsymbol{u}_{im,1}^{k+1}}\right)^i & \cdots & 0 \\ \vdots & \vdots & \ddots & \vdots \\ \left(\frac{\partial \boldsymbol{g}_{im,N}}{\partial \boldsymbol{u}_m^{k+1}}\right)^i & 0 & \cdots & \left(\frac{\partial \boldsymbol{g}_{im,N}}{\partial \boldsymbol{u}_{im,N}^{k+1}}\right)^i \end{bmatrix} \begin{bmatrix} \left(\boldsymbol{u}_m^{k+1}\right)^{i+1} - \left(\boldsymbol{u}_m^{k+1}\right)^i \\ \left(\boldsymbol{u}_{im,1}^{k+1}\right)^{i+1} - \left(\boldsymbol{u}_{im,1}^{k+1}\right)^i \\ \vdots \\ \left(\boldsymbol{u}_{im,N}^{k+1}\right)^{i+1} - \left(\boldsymbol{u}_{im,N}^{k+1}\right)^i \end{bmatrix} = -\begin{bmatrix} (\boldsymbol{g}_m)^i \\ \left(\boldsymbol{g}_{im,1}\right)^i \\ \vdots \\ \left(\boldsymbol{g}_{im,N}\right)^i \end{bmatrix} \tag{2.12}$$

in which, $\boldsymbol{u}_m$ is the column vector containing all components in mobile zone at all nodes, and $\boldsymbol{u}_{im,j}$ is the column vector containing all the components in jth immobile zone at all nodes, the matrix at the left hand side is the Jacobian matrix $\left(\partial \boldsymbol{g}/\partial \boldsymbol{u}^{k+1}\right)^i$ consisting of the derivatives of system equations with respect to the unknown components in both mobile and immobile zones at all nodes.

The important feature of equation (2.12) is the block diagonal form of the lower portion of the Jacobian, which allows us to rewrite it into blocks representing the mobile and immobile zones separately and leads to

$$\begin{bmatrix} \boldsymbol{A} & \boldsymbol{B} \\ \boldsymbol{C} & \boldsymbol{D} \end{bmatrix} \begin{bmatrix} \boldsymbol{x} \\ \boldsymbol{y} \end{bmatrix} = \begin{bmatrix} \boldsymbol{a} \\ \boldsymbol{b} \end{bmatrix} \tag{2.13}$$

Block $\boldsymbol{D}$ is a block diagonal matrix with $N_n \times N$ blocks of size $N_u \times N_u$ (N_n being the number of mesh nodes and N_u the number of components). This characteristic can be used to solve system equations by

defining Schur complement of block $\boldsymbol{D}$, that is $\boldsymbol{A}-\boldsymbol{B}\boldsymbol{D}^{-1}\boldsymbol{C}$. In this way, solutions can be efficiently solved by

$$\left(\boldsymbol{A}-\boldsymbol{B}\boldsymbol{D}^{-1}\boldsymbol{C}\right)\boldsymbol{x}=\left(\boldsymbol{a}-\boldsymbol{B}\boldsymbol{D}^{-1}\boldsymbol{b}\right) \tag{2.14}$$

$$\boldsymbol{y}=\boldsymbol{D}^{-1}(\boldsymbol{b}-\boldsymbol{C}\boldsymbol{x}) \tag{2.15}$$

The traditional approach is to solve equation (2.12) as one large system with a size equal to $N_n \times N_u \times N$. We propose to split the solution into two parts, first solving equation (2.15), followed by equation (2.14). We conjecture that this is much less costly, because equation (2.14) is N times smaller than that of the traditional approach of equation (2.12) and, because the block diagonal structure of matrix $\boldsymbol{D}$ permits the calculation of its inverse for each immobile zone of each node separately. The approach is valid not only for MRMT, but also for MINC of SINC. The difference lies in that, if these methods are adopted, then matrix $\boldsymbol{D}$ must include all immobile zones connected to a node, instead of each immobile zone separately**.** Note that both solution approaches are mathematically equivalent, which means that the convergence of the Newton-Rapson method will be identical for both.

2.2.2 Algorithms

We apply two nested Newton-Raphson iteration loops to solve the nonlinear system in each time step, the outside one is used to solve components transport, the inner one is used for chemical speciation calculation in each iteration. The algorithm proceeds as follows:

Step 0: Set $i=0$, and initialize components $\left(\boldsymbol{u}^{k+1}\right)^{i}=0$.

Step 1: Compute functions $\boldsymbol{g}^{i}$**.**

Step 2: Compute the derivative of functions to construct Jacobian matrix $\left(\frac{\partial \boldsymbol{g}}{\partial \boldsymbol{u}^{k+1}}\right)^{i}$.

Step 3: Solve system equation (2.14) and (2.15) to get solutions $\Delta\boldsymbol{u}^{k+1}=\left(\boldsymbol{u}^{k+1}\right)^{i+1}-\left(\boldsymbol{u}^{k+1}\right)^{i}$.

Step 4: Compute solutions at next iteration step, $\left(\boldsymbol{u}^{k+1}\right)^{i+1}=\left(\boldsymbol{u}^{k+1}\right)^{i}+\Delta\boldsymbol{u}^{k+1}$.

Step 5: Execute speciation calculation of primary species concentrations $\left(\boldsymbol{c_1}^{k+1}\right)^{i}$ and secondary species concentrations $\left(\boldsymbol{c_2}^{k+1}\right)^{i}$ from components $\left(\boldsymbol{u}^{k+1}\right)^{i}$ according to equations of components and mass action law iteratively. Then calculate the derivatives of $\left(\frac{\partial \boldsymbol{r}(\boldsymbol{u}^{k+1})}{\partial \boldsymbol{c_1}^{k+1}}\right)^{i}$ and $\left(\frac{\partial \boldsymbol{c_1}^{k+1}}{\partial \boldsymbol{u}^{k+1}}\right)^{\boldsymbol{i}}$. Furthermore, compute the derivatives of kinetics with respect to components $\left(\frac{\partial \boldsymbol{r}_{k,m}^{k+1}}{\partial \boldsymbol{u}_{m}^{k+1}}\right)^{i}$ and $\left(\frac{\partial \boldsymbol{r}_{k,im,j}^{k+1}}{\partial \boldsymbol{u}_{im,j}^{k+1}}\right)^{i}$ to facilitate the calculation of function derivatives $\left(\frac{\partial \boldsymbol{g}}{\partial \boldsymbol{u}^{k+1}}\right)^{i}$.

Step 6: Convergence check. If $\left(\boldsymbol{u}^{k+1}\right)^{i+1}$ close to $\left(\boldsymbol{u}^{k+1}\right)^{i}$ or $\boldsymbol{g}^{i+1}\approx\boldsymbol{0}$, then stop. Otherwise, set $i=i+1$, and return to step 1.

2.3 Accuracy Verification and Efficiency Analysis

2.3.1 Accuracy Verification

To test the accuracy of the proposed solution, we perform 1D simulations of (1) non-reactive transport test, (2) multicomponent reactive transport for MRMT in chemical equilibrium and (3) kinetics. All these models are under the same MRMT model, with $L=100.0$ m, $\phi_m=0.1$, $\phi_{im}=0.1$, $q=1.0$m/s, $D=10.0\text{m}^2/\text{s}$, and a power law distribution of mass exchange rates, the corresponding residence time

(that is the inverse of the mass exchange rate, $\tau \equiv 1/\alpha$) distribution, $P(\tau) \propto \tau^{-\beta}$, with exponent $\beta = 3/2$.

2.3.1.1 Non-reactive solute

We compared our method with that of Silva et al. (2009), which differs from our method in that it writes the concentrations of the immobile zones as an explicit function of those of the mobile zones. This can be done only for non-reactive transport. In Figure 2.2**,** the break-through curve of solute at distance $x = 100.0$ m is displayed. It is a typical BTC, the characteristic advection time t_{adv} is between $\phi_m x/q$ and $(\phi_m + \phi_{im})x/q$, and the concentrations decrease for times longer than the characteristic advection time, at the late times the power law tail is reproduced as $c(t) \propto t^{-\beta-1}$. The blue solid line is the numerical formulation proposed by Silva et al. (2009), and the square red line is the numerical solution of our proposed method. As can be seen, these two numerical solutions are almost identical. The small differences may be due to the explicit calculation of the concentrations of the immobile zones by the method of Silva et al. (2009).

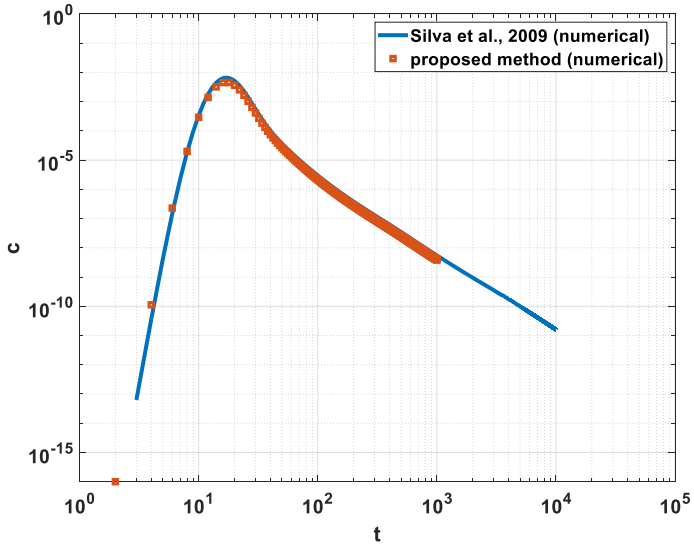

Figure 2.2 Comparison between the results of the non-reactive transport model calculated by the proposed method and the method of Silva et al. (2009).

2.3.1.2 Equilibrium gypsum dissolution

Figure 2.3 displays component (left) concentrations and (right) reaction rates for a case physically identical to the above one, but transporting Ca^{2+} and SO_4^{2-} in equilibrium with gypsum $CaSO_4 = Ca^{2+} + SO_4^{2-}$ for which we apply the mass action law: $a_{Ca^{2+}} a_{SO_4^{2-}} = K$, where a is activity and K is an equilibrium constant ($logK(25℃) = -4.4823$). Activities are calculated from concentrations by means of the extended Debye Hückel equation. We compare the numerical results of our proposed method with the analytical solution of Donado et al., (2009). As we can see the numerical results are consistent with analytical solutions. A clear separation between BTCs in mobile and immobile zones is presented due to the physical mass transfer limitations, components both in mobile and immobile zones are retarded at late time. Notice that the reaction rates are negative, that means calcium ion and sulfate ion are oversaturated and precipitated into gypsum. The analytical solutions of reaction rates in mobile and immobile zones, which are given by

$$\boldsymbol{r}_{im}(x,t) = \int_0^\infty f(\alpha) \left\{ \frac{\partial \boldsymbol{c}_{im}(x,\alpha,t)}{\partial t} - \alpha[\boldsymbol{c}_m(x,t) - \boldsymbol{c}_{im}(x,\alpha,t)] \right\} d\alpha \tag{2.16}$$

(2.17)

$$\boldsymbol{r}_m(x,t) = -\frac{\partial \boldsymbol{c}_{m,2}(x,t)}{\partial \boldsymbol{u}_m(x,t)}\left[\frac{\phi_{im}}{\phi_m}\int_0^{\infty} f(\alpha)\frac{\partial \boldsymbol{u}_{im}(x,\alpha,t)}{\partial t}d\alpha\right] + \frac{\phi_{im}}{\phi_m}\int_0^{\infty} f(\alpha)\frac{\partial \boldsymbol{c}_{im,2}(x,\alpha,t)}{\partial \boldsymbol{u}_{im}(x,\alpha,t)}\frac{\partial \boldsymbol{u}_{im}(x,\alpha,t)}{\partial t}d\alpha - \frac{\partial^2 \boldsymbol{c}_{m,2}(x,t)}{\partial \boldsymbol{u}_m^2(x,t)}\nabla^T \boldsymbol{u}_m(x,t)\boldsymbol{D}\nabla \boldsymbol{u}_m(x,t) - \frac{\phi_{im}}{\phi_m}\boldsymbol{r}_{im}(x,t)$$

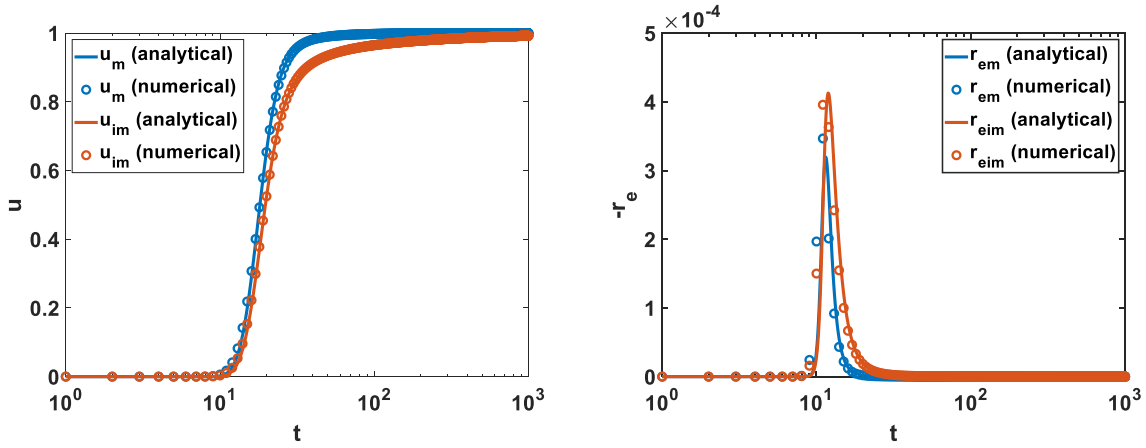

Figure 2.3 Distribution of (left) components u_m and u_{im}, (right) reaction rates r_m and r_{im} versus time at distance $x = 100.0$m. The blue color represents state variables in the mobile zone, and the red color represents state variables in immobile zones. The solid lines are the analytical solutions and the circle dot lines are the proposed numerical solutions.

2.3.1.3 Kinetic reaction

To test the performance of our proposed solution in chemical kinetics, we choose a simple first-order kinetics. In this case, the analytical solution can be found in the Laplace domain (the solution is deduced in Appendix B). Then we simulate the distribution of components and kinetic rates both in mobile and immobile zones over time with the component degradation rate $\kappa = 0.01$. As we can see the proposed numerical solutions agree with the analytical solution as displayed in Figure 2.4. Comparing the evolution of components in chemical equilibrium (Figure 2.4 left), the presence of chemical reactions decreases the concentrations of the components both in mobile and immobile zones.

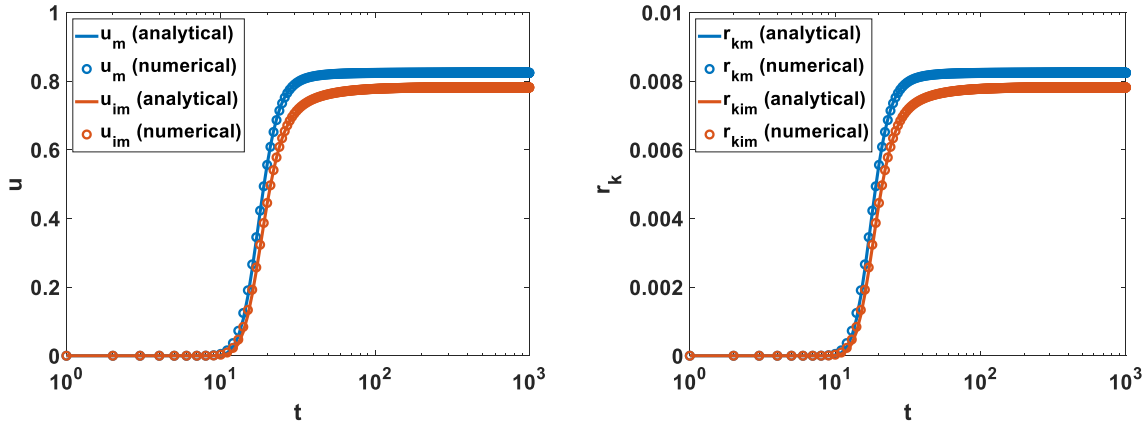

Figure 2.4 Distribution of (left) components u_m and u_{im}, (right) reaction rates r_m and r_{im} versus time at distance $x = 100.0$m. The blue color represents state variables in the mobile zone, and the red color

represents state variables in immobile zones. The solid lines are the analytical solutions and the circle dot lines are the proposed numerical solutions.

2.3.2 Efficiency Analysis

The efficiency of the algorithm depends on the problem size n, the total number of unknowns of system equation (2.13) that equals to the number of mesh nodes times the number of components times the number of immobile zones plus one. In our problem, the matrix operation is the most time consuming. Both the computational cost of matrix multiplication and matrix inversion are $O(n^3)$.

Instead of solving system equation (2.13) globally, we solve it in blocks representing mobile and immobile zones separately, using equations (2.14) and (2.15). Since these two approaches are mathematically identical, the two will converge to the same solution within the same iterations. The advantage of the proposed block solution is that it reduces the size of the system to be the number of mesh nodes times the number of components.

We simulate an irreversible bimolecular reaction $A + B \rightarrow C$ for the number of immobile zones equal to 3, 10, 30, 50, 70 and 100, with a second-order kinetics $r_k = \kappa c_A c_B$. In Figure 2.5, we compare the CPU time of the proposed method (i.e., block solver) and full DSA on a log-log scale. As we can see, the CPU time of the block solver increases linearly with the number of immobile zones (N), while that of the full DSA increases much faster, approximating to N^3. Clearly, the block solver runs faster than full DSA for a higher number of immobile zones. For a small number of immobile zones, the full DSA runs faster because of the costs of building the more complicated structure of the block solver.

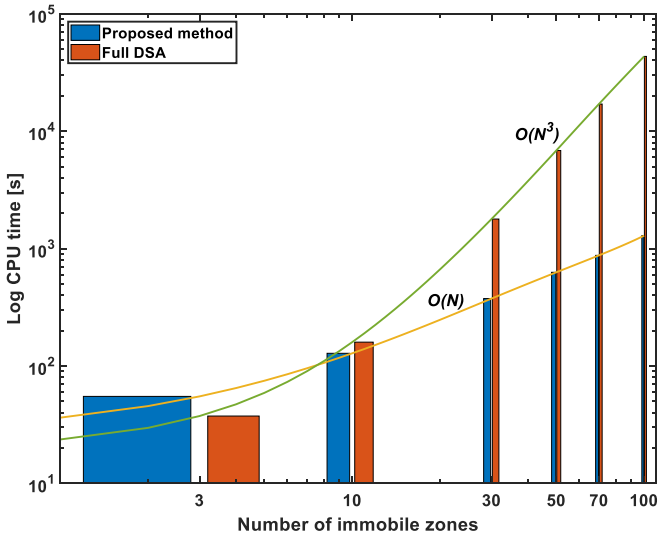

Figure 2.5 CPU time comparison between proposed method and full DSA for different number of immobile zones. The chemical systems are identical for all cases that is an irreversible bimolecular reaction $A + B \rightarrow C$, with a second-order kinetics $r_k = \kappa c_A c_B$.

2.4 Conclusions

The proposed method is effective and efficient for reactive transport modeling capable of accounting for numerous immobile zones. We formulate the general numerical solution of reactive transport with MRMT based on the Newton-Raphson method, which enables us to simulate complex chemical kinetics. For chemical systems, whatever it is in equilibrium or in kinetics, the convergent solution is efficiently solved within several iterations.

The proposed numerical solution is verified in case of passive solute transport, chemical equilibrium and chemical kinetics. In all cases the simulations agree very well with available analytical solutions and other numerical solutions. The full consistency between the proposed numerical solutions and available analytical solutions indicate that our proposed method is capable of reproducing the anomalous transport of reactive transport with MRMT.

The computational efficiency of the proposed algorithm is improved by solving system equations in block instead of full DSA, which eliminates the impact of the number of immobile zones on the computational complexity and decreases the size of the linear system to be the number of mesh nodes times the number of components. This may become particularly important for more complicated chemical models in combination with MRMT. In that case the full DSA can become prohibitively expensive in CPU and the block solver may be the only feasible method.

The advantage of the method increases with the number of immobile zones. Babey et al. (2015) concluded that five immobile zones (compared to one hundred in our models) are sufficient to address anomalous transport of non-reactive solutes. However, this may be different for reactive transport because of the broad range of residence times (Haggerty et al., 2000) and chemical localization (Soler-Sagarra et al., 2016). The number of immobile zones needed for proper reproduction of reactive processes requires further research.

2.5 Computer Code Availability

Name of code: Reactive Transport with Multirate Mass Transfer

Developer: Jingjing Wang

Contact detail: Department of Civil and Environmental Engineering, Universitat Politécnica de Catalunya (UPC), Jordi Girona 1-3, 08034 Barcelona, Spain

Email: jingjing.wang.xiang@gmail.com

Year first available: October, 2020

Hardware required: No specific hardware is required. However, the code has been developed on a computer with processor Intel® Core™ i5-6500 CPU @ 3.20GHz, 16GB Installed memory (RAM), 64-bit Operating System, x64-based processor.

Software development platform: Microsoft Visual Studio 2015

Program language: object-oriented programming FORTRAN 2003

Compiler: Intel Parallel Studio XE 2017 Cluster Edition for Windows*

Library: Intel® Math Kernel Library. To solve the system equation (2.14), we call routine dgbtrf() to compute the LU factorization of the left hand side matrix of system equation (2.14), then we call routine dgbtrs() to solve the linear system with the LU-factored square coefficient matrix returned by routine dgbtrf().

Program size: 4.39 MB

Details on how to access the open-source code: the source code can be freely download from GitHub on the public repository https://github.com/Jingjingwangxiang/RT_MRMT_DSA.

Our codes are developed in object-oriented instead of procedural-oriented which lacks flexibility and extensibility (Meysman et al., 2003a ; Meysman et al., 2003b). The object-oriented programming allows the code reusability and facilitates the implementation of reactive transport modeling. To simulate the reactions, two main modules are developed. The biochemical system module simulates the localized chemical reactions occurring in a (bio)chemical system, it contains procedures that are capable of constructing the stoichiometric matrix and component matrix. The local biochemistry module captures

(bio)chemical state variables at each mesh node, such as components, concentrations, equilibrium reaction rates, kinetics, as well as the derivatives of kinetics with respect to concentrations, etc. It encapsulates procedures of chemical calculations that are capable of computing the state variables at each mesh node by using the biochemistry system module. These two main developed modules are coupled with the transport equations in the reactive transport module, which enables the modeling of reactive transport.

3 On the localization of chemical reactions in multicontinuum media *

The objective of this work is to study the localization of reactions in different portions of the porous medium. For this we use the non-local MRMT model, which views the porous media as being composed of one mobile zone and many immobile zones. The localized physical and chemical heterogeneity are reflected by a distribution of residence times and reaction times in the different immobile zones, which can be incorporated in the governing equations through memory functions and reaction rate kernels, respectively. We show that the dimensionless form of governing equations is characterized by reaction times, transport times and distribution of residence times. To analyze the interplay between them, we simulated three cases: one without reactions, one with a single reaction and one with sequential reactions. The results indicate that reactions driven by species that are not present in the inflowing water but are the result of previous reactions will take place in immobile zones, whose residence time is comparable to reaction times. Furthermore, mobile zones with residence times much smaller than those for transport can be lumped together (assuming that very fast reactions are assumed in equilibrium), which greatly reduces computations.

* This chapter is based on the manuscript Wang et al., 2021. On the localization of chemical reactions in multicontinuum media, submitted to *Water*, under review.

3.1 Introduction

Characterization of reactive transport in heterogeneous media is important for environmental science and engineering problems, such as managed aquifer recharge, seawater intrusion, CO2 geological storage, and in situ bioremediation. Physical heterogeneity may induce chemical heterogeneity or localization of chemical reactions by which different reactions occur in different portions of the porous medium (Soler-Sagarra et al., 2016; Babaei & Islam, 2018). Dentz et al. (2011) concluded that transport under physical and chemical heterogeneity cannot be upscaled separately: upscaling reactions depends on physical heterogeneity and upscaling transport is affected by chemical heterogeneity. In addition, we acknowledge that the behavior of macroscale transport in the mobile zone of the porous medium is determined by the microscale transport process in immobile zones (Gouze et al., 2008). Yet, it is not so clear how the localized physical and chemical heterogeneity affects the distribution and evolution of reactive species in different portion of immobile zones and how these microscale processes in immobile zones govern the reactive transport in mobile zone?

It is well known that transport in heterogeneous porous media displays anomalous (non-Fickian) behavior (Kitanidis, 1988) both at field (Adams & Gelhar, 1992) and laboratory scales (Valocchi, 1985; Levy & Berkowitz, 2003; Berkowitz & Scher, 2009). Hence, the advection-dispersion-reaction equation (ADRE) is no longer appropriate. Many non-local methods have been developed to represent this anomalous transport, including continuous time random walks (CTRW) (Berkowitz & Scher, 1998; Dentz et al., 2004; Berkowitz et al., 2006; Berkowitz et al., 2006; Dentz et al., 2015), fractional advection-dispersion equations (fADE) (Benson et al., 2000; Schumer et al., 2003; Marseguerra & Zoia, 2008), multirate mass transfer (MRMT) (Haggerty & Gorelick, 1995; Wang et al., 2005; Salamon et al., 2006; Benson & Meerschaert, 2009; Dentz et al., 2011; Fernàndez-Garcia & Sanchez-Vila, 2015; De Dreuzy & Carrera, 2016), memory functions (Carrera et al., 1998; Haggerty et al., 2000; Willmann et al., 2008; Gouze et al., 2008) and so forth. Although these methods use different approaches, essentially they are equivalent (Dentz & Berkowitz, 2003; Silva et al., 2009; Neuman & Tartakovsky, 2009). Many studies focus on the behavior of breakthrough curves (BTCs) and conservative transport in heterogeneous porous media (Haggerty et al., 2000; Schumer et al., 2003; Willmann et al., 2008; Berkowitz & Scher, 2009; Dentz et al., 2015). Only few deals with reactive transport (Willmann et al., 2010; Dentz et al., 2011) probably due the complexity of reactive transport in heterogeneous porous media. For non-linear kinetic reactions, no analytical solutions exist in the Laplace domain which further limits the study of the problem.

Among the non-local methods, the MRMT formulation allows localized concentrations which simplifies the simulations of reactive transport in physical and chemical heterogeneous media (Dentz et al., 2011; Soler-Sagarra et al., 2016; Babaei & Islam, 2018). Moreover, the MRMT formulation for conservative transport can be extended to reactive transport, including nonlinear reactions (Willmann et al., 2010).

The objective of this work is to study the effects of localized physical and chemical heterogeneity on reactive transport based on the MRMT formulation. To do so, first, we establish the governing equations of reactive transport in multicontinuum media and deduce a dimensionless form of these equations. Then we present three models one without reactions, one with a single reaction, and one with two sequential reactions in section 3.3, whose results are analyzed in section 3.4. The last section is dedicated to the conclusions.

3.2 Methodology

We model reactive transport in heterogeneous porous medium by using the MRMT approach (Haggerty & Gorelick, 1995). Every point (representative elementary volume) is viewed as consisting of a mobile zone and a distribution of immobile zones characterized by their residence time. Each of these

exchanges solute mass with the mobile portion proportionally to the mass transfer rate, $\alpha[\mathrm{T}^{-1}]$. Therefore, it is natural to characterize this distribution by a probability density function (pdf) of mass transfer rates, $f(\alpha)$ (see Figure 3.1 left). To facilitate comparison to other non-local methods, we also characterize immobile zones by the distribution, $P(\tau_\alpha)$, of residence times, $\tau_\alpha \equiv 1/\alpha$ [T] (Haggerty et al., 2004) (see Figure 3.1 right). $P(\tau_\alpha)$ is given by (Dentz & Berkowitz, 2003; Dentz et al., 2011; Dentz et al., 2015)

$$P(\tau_\alpha) = \tau_\alpha^{-2} f(\alpha) \tag{3.1}$$

The residence time probability $P(\tau_\alpha)d\tau_\alpha$ is the frequency of the immobile zone, characterized by the residence time in the interval $[\tau_\alpha, \tau_\alpha + d\tau_\alpha]$. Obviously, it satisfies the condition $\int_0^\infty P(\tau_\alpha)\, d\tau_\alpha = 1$.

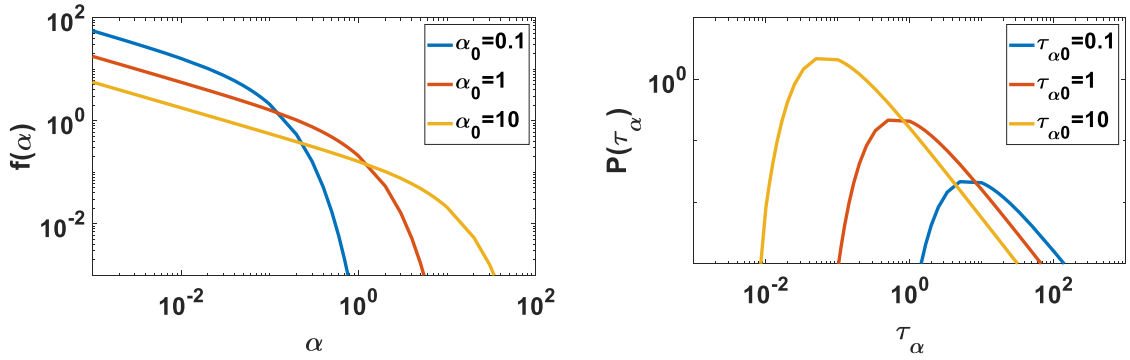

Figure 3.1 Pdf of exchange rates, α (Gamma distibution), and residence times, τ_α, plotted in log-log scale for several values of $\tau_{\alpha 0}$ and $\beta = 1/2$. Note that the maximum of latter is around $\tau_{\alpha 0}$ (the mode is $\tau_{\alpha 0}/(\beta+1)$ and the expected value $\tau_{\alpha 0}/(1-\beta)$). Its large τ_α slope is $\beta + 1$.

3.2.1 Governing equations

The transport of any reactive species in a medium that consists of a mobile continuum and multiple immobile continua can be expressed as (Donado et al., 2009; Willmann et al., 2010; Dentz et al., 2011)

$$\phi_m \frac{\partial c_m}{\partial t} = L_t[c_m] - \phi_{im} \int_0^\infty \frac{1}{\tau_\alpha} P(\tau_\alpha)[c_m(x,t) - c_{im}(x,\tau_\alpha,t)]\, d\tau_\alpha + \phi_m r_m \tag{3.2}$$

where $L_t[c_m] = -[q_m \nabla c_m] + \nabla \cdot [\phi_m D_m \nabla c_m]$ is the transport operator that describes advection and dispersion, q_m [LT^{-1}] is Darcy flux, D_m [$\mathrm{L}^2\mathrm{T}^{-1}$] is the hydrodynamic dispersion tensor; ϕ_m [-] and ϕ_{im} [-] are the porosities of mobile and immobile zones, which denote the volume fraction of the mobile pore zone and immobile pore zones over the bulk volume, respectively; c_m [ML^{-3}] and c_{im} [ML^{-3}] are concentrations in the mobile and immobile zone, which are expressed as mass per unit volume of mobile zone and mass per unit volume of immobile zone; r_m [$\mathrm{ML}^{-3}\mathrm{T}^{-1}$] is the sink-source term due to chemical reactions in mobile zone and corresponds to the mass removed by reactions in mobile zone per unit volume of mobile water per unit time.

Mass balance in each immobile zone is given by

$$\frac{\partial c_{im}(x,\tau_\alpha,t)}{\partial t} = \frac{1}{\tau_\alpha}[c_m(x,t) - c_{im}(x,\tau_\alpha,t)] + r_{im}(x,\tau_\alpha,t) \tag{3.3}$$

where r_{im} [$\mathrm{ML}^{-3}\mathrm{T}^{-1}$] is the reactions sink-source term in the immobile zone with residence time τ_α, which corresponds to the mass removed by reactions in the immobile zone per unit volume of immobile water per unit time.

The mass exchange between mobile and immobile zone is modeled by a first-order mass transfer mechanism, represented by the continuous variable τ_α and characterized by the distribution density function $P(\tau_\alpha)$ for the immobile zones. Thus, the total mass exchange is the weighted sum over all

immobile zones as expressed in the integral term of equation (3.2). Integrating equation (3.3) with weight $P(\tau_\alpha)$ in terms of τ_α, multiplying by ϕ_{im}, and substituting it into equation (3.2), yields the total solute mass balance,

$$\phi_m \frac{\partial c_m(x,t)}{\partial t} + \phi_{im} \int_0^\infty P(\tau_\alpha) \frac{\partial c_{im}(x,\tau_\alpha,t)}{\partial t} d\tau_\alpha = L_t[c_m(x,t)] + r(x,t) \tag{3.4}$$

in which, r is the total reaction rate (now per unit volume of bulk porous medium) that integrates reactions in both mobile and immobile zones,

$$r(x,t) = \phi_m r_m(x,t) + \phi_{im} \int_0^\infty P(\tau_\alpha) r_{im}(x,\tau_\alpha,t)\, d\tau_\alpha \tag{3.5}$$

If the reaction follows first-order kinetics, the reaction rate in mobile zone will be

$$r_m(x,t) = -k_m c_m(x,t) \tag{3.6}$$

where k_m is the reaction rate constant. Similarly, the local reaction rate in the τ_α immobile zone becomes

$$r_{im}(x,\tau_\alpha,t) = -k_{im}(\tau_\alpha) c_{im}(x,\tau_\alpha,t) \tag{3.7}$$

where $k_{im}(\tau_\alpha)$ [T^{-1}] is the local reaction rate constant. The reaction time in the immobile zone of τ_α is $\tau_r \equiv 1/k_{im}(\tau_\alpha)$, which is a variable dependent on the immobile zone.

By inserting equation (3.7) into (3.3), then solving equation (3.3), we obtain the concentration in the immobile zone of τ_α as a function of mobile concentration history

$$c_{im}(x,\tau_\alpha,t) = c_{im}(x,\tau_\alpha,t=0) e^{-[\alpha + k_{im}(\tau_\alpha)]t} + \int_0^t \varphi(t-t') c_m(x,t')\, dt' \tag{3.8}$$

in which, the definition of $\varphi(t)$ is

$$\varphi(t) = \frac{1}{\tau_\alpha} e^{-[\alpha + k_{im}(\tau_\alpha)]t} \tag{3.9}$$

Assuming that the initial concentration in the immobile zones is zero (i.e., $c_{im}(x,\tau_\alpha,t=0) = 0$), then by substituting equation (3.8) into equation (3.2) and rearranging terms, we obtain the total solute mass balance, as a sole function of c_m

$$\phi_m \frac{\partial c_m(x,t)}{\partial t} + \phi_{im} \frac{\partial}{\partial t} \int_0^t g(t-t') c_m(x,t') dt' = L_t[c_m(x,t)] - \int_0^t \kappa(t-t') c_m(x,t') dt' \tag{3.10}$$

where the memory function (Carrera et al., 1998; Haggerty et al., 2000) and reaction rate kernel (Dentz et al., 2011) are given by

$$g(t) = \int_0^\infty P(\tau_\alpha) \varphi(t) d\tau_\alpha \tag{3.11}$$

and

$$\kappa(t) = \phi_m(x) k_m \delta(t) + \phi_{im}(x) \int_0^\infty \frac{1}{\tau_r} P(\tau_\alpha) \varphi(t) d\tau_\alpha \tag{3.12}$$

respectively. In which, $\delta(t)$ is the Dirac delta. The memory function can be viewed as the rate of change of concentration in the immobile zone that is caused by a unit change of concentration in the mobile zone at initial time $t = 0$. In the presence of reactions, the memory function not only incorporates the

distribution of local mass transfer rates but also the distribution of local reaction rates. Similarly, the reaction rate kernel represents the local reactions in immobile zones, it integrates both the reactions in mobile and immobile zones, and accounts for the mass transfer between mobile and immobile zones.

Although the memory function is mainly controlled by the distribution of residence times in immobile zones, it is also affected by the local reaction times in immobile zones. Likewise, the reaction rate kernel is mainly controlled by the chemical reactions, but it is also affected by the distribution of residence times in immobile zones (Dentz et al., 2011).

Clearly, the governing equations of reactive transport under physical and chemical heterogeneity (3.10), (3.11) and (3.12) are controlled by the distribution of residence times and reaction times in immobile zones simultaneously. The physical and chemical heterogeneities interact with each other, and together they govern reactive transport (Dentz et al., 2011).

3.2.2 Dimensionless formulations

To characterize the governing equation (3.10), (3.11) and (3.12), we define the characteristic length as follows

$$L_c = \frac{\phi_m D_m}{q_m} \tag{3.13}$$

and the characteristic transport time as follows

$$t_c = \frac{L_c}{v_m} = \frac{\phi_m^2 D_m}{q_m^2} \tag{3.14}$$

Note, that in 1D, the characteristic length equals the longitudinal dispersivity α_L due to the definition of dispersion $D_m = \alpha_L v_m$, where $v_m = q_m/\phi_m$ is the mean fluid velocity in porous media. Introducing these definitions of characteristic length and characteristic transport time into equation (3.10), we obtain the dimensionless form of the governing equations, that is

$$\begin{aligned} &\frac{\partial c_{mD}}{\partial t_D} + \eta \frac{\partial}{\partial t_D} \int_0^{t_D} g(t_D - t_D') c_{mD}(t_D') dt_D' \\ &\qquad = -\nabla_D c_{mD} + \nabla_D \cdot \nabla_D c_{mD} - \int_0^{t_D} \kappa(t_D - t_D') c_{mD}(t_D') dt_D' \end{aligned} \tag{3.15}$$

with the following dimensional variables

$$c_{mD} = \frac{c_m}{c_c}, \qquad t_D = \frac{t}{t_c}, \qquad x_D = \frac{x}{L_c}, \qquad \eta = \frac{\phi_{im}}{\phi_m}, \qquad \tau_{\alpha_D} = \frac{\tau_\alpha}{t_c}, \qquad \tau_{r_D} = \frac{\tau_r}{t_c} \tag{3.16}$$

In the dimensionless formulations of governing equation (3.15), the physical and chemical heterogeneity are represented by the distribution of residence times and reaction times, respectively, and reflected simultaneously in the memory function and reaction rate kernel.

Obviously, in the situation where the characteristic length L_c and the dimensionless ratio of porosity of immobile zone to porosity of mobile zone η are invariables, the governing equation (3.15) in dimensionless form are totally governed by three characteristic times, that is the characteristic transport time t_c, the dimensionless residence time τ_{α_D} and the dimensionless reaction time τ_{r_D} in immobile zones.

The solution of governing equation (3.15) in Laplace domain is expressed as

$$\mathcal{L}\{c_{mD}\}(s) = exp\left[\frac{x_D}{2}\left(1 - \sqrt{1 + 4[s[1 + \eta\mathcal{L}\{g\}(s)] + \mathcal{L}\{\kappa\}(s)]}\right)\right] \tag{3.17}$$

where $\mathcal{L}\{\cdot\}(s)$ represents the Laplace transform of a function. The Laplace transform of the memory function and reaction rate kernel are defined as

$$\mathcal{L}\{g\}(s) = \int_0^\infty P(\tau_\alpha)\mathcal{L}\{\varphi\}(s)d\tau_{\alpha D} \tag{3.18}$$

and

$$\mathcal{L}\{\kappa\}(s) = k_m t_c + \eta \int_0^\infty \frac{1}{\tau_{r_D}} P\left(\tau_{\alpha_D}\right)\mathcal{L}\{\varphi\}(s)d\tau_{\alpha_D} \tag{3.19}$$

in which, the Laplace transform of $\varphi(t)$ is

$$\mathcal{L}\{\varphi\}(s) = \frac{\frac{1}{\tau_{\alpha D}}}{\frac{\tau_{\alpha D} + \tau_{rD}}{\tau_{\alpha D}\tau_{rD}} + s} \tag{3.20}$$

If we substitute s for $s[1 + \eta\mathcal{L}\{g\}(s)] + \mathcal{L}\{\kappa\}(s)$ in equation (3.17), then equation (3.17) becomes the solution of the transport equation in homogeneous media. Obviously, the retardation of localized physical heterogeneity on transport is reflected in the term $s\eta\mathcal{L}\{g\}(s)$, and the decay of localized chemical heterogeneity on reactive species is shown in the term $\mathcal{L}\{\kappa\}(s)$.

3.3 Solution method

To study the behavior of reactive transport in physically and chemically heterogeneous media, we simulated three cases using the formulation of section 3.2. For the calculation we used the code RT_MRMT_DSA (Wang et al., 2021, Chapter 2) which is an object-oriented code based on finite element method (FEM). The global solutions are solved by applying the iterative Newton-Raphson method.

3.3.1 Numerical setup

All the model are one-dimensional with the properties $\phi_m = 0.1$ [-], $\phi_{im} = 0.3$ [-], $\alpha_L = 1.0$ [L], $q_m = 1.0$ [LT^{-1}]. Thus we have $L_c = 1.0$ [L], $t_c = 0.1$ [T], $\eta = 3.0$. The length of the domain $L = 100L_c$, and the simulated time $T = 10^4 t_c$. The space interval $\Delta x_D = L_c$ and the time interval $\Delta t_D = t_c$.

Initial concentrations are set to zero both in mobile and immobile zones, that is $c_m(x, t = 0) = 0.0$ [ML^{-3}] and $\boldsymbol{c}_{im}(x, \tau_\alpha, t = 0) = 0.0$ [ML^{-3}], except for the first mobile node that has initial concentration $c_m(x = 0, t = 0) = 1.0$ [ML^{-3}].

At the inlet, we set a Cauchy boundary condition to express that no solute mass enters the domain

$$D_m\nabla c_m(x = 0, t)\cdot\mathbf{n} = q_m[c_e(x = 0, t) - c_m(x = 0, t)], \qquad q_m\cdot\mathbf{n} < 0 \tag{3.21}$$
$$c_e(x = 0, t) = 0.0$$

where c_e is the concentration of the inflowing water. The outlet is an open boundary condition

$$D_m\nabla c_m(x = L, t)\cdot\mathbf{n} = 0, \qquad q_m\cdot\mathbf{n} \geq 0 \tag{3.22}$$

where $\mathbf{n}$ is a unit vector which is normal to the boundary, and $\cdot$ represents the inner product operator.

In addition to the calculation of concentrations of this pulse injection, we also calculated the accumulative concentration until time t ($\int_{t=0}^{t=t} c dt$) for both mobile and immobile zones. This is equivalent to a continuous injection, simulated through a Cauchy boundary condition at the inlet (equation (3.21)) with c_e equal to the initial mass of the pulse injection divided by the flow rate ($c_e = 0.5\Delta x\phi_{im}c_m(x = 0, t = 0)/q_m = 0.05$).

3.3.2 Cases considered

We simulated three cases: a no reaction system (conservative transport), a single reaction system and a sequential reaction system. All models use the same gamma distribution of residence times with $\beta = 1/2$, $\tau_{\alpha_0 D} = 10^1$.

In the single reaction system, only one reaction $A \rightarrow B$ occurs, following a first-order rate law with $r_{k1} = k_1 c_A$. Thus, the degradation of species A follows $r_A = -k_1 c_A$, and the formation of species B, $r_B = k_1 c_A$. In the sequential reaction system, two sequential reactions $A \rightarrow B$ and $B \rightarrow C$ take place simultaneously. The reaction rates of both are first-order with $r_{k1} = k_1 c_A$, and $r_{k2} = k_2 c_B$. Thus, the degradation of species A follows $r_A = -k_1 c_A$, the formation and degradation of species B, $r_B = k_1 c_A - k_2 c_B$, and the formation of species C, $r_C = k_2 c_B$.

3.3.3 Steady state analytical solution

The final steady state is referred to the cumulative concentration of species in immobile and mobile zone, respectively. The ratio between them is given by

$$\int_0^\infty c_{imD}(x_D, \tau_{\alpha D}, t_D) dt_D \Big/ \int_0^\infty c_{mD}(x_D, t_D) dt_D = \mathcal{L}\{\varphi\}(s)|_{s=0} \tag{3.23}$$

as can be obtained from the Laplace transform of equation (3.8) and (3.9).

The concentration in immobile zone is the weighted integral of concentrations in all immobile zones, which is defined as

$$c_{imD}(x_D, t_D) = \int_0^\infty P(\tau_{\alpha D}) c_{im}(x_D, \tau_{\alpha D}, t_D)\, d\tau_{\alpha D} \tag{3.24}$$

From equation (3.8), we can obtain that

$$c_{imD}(x_D, t_D) = \int_0^{t_D} g(t_D - t'_D) c_m(x_D, t'_D) dt'_D \tag{3.25}$$

Then, the ratio between the cumulative concentrations in immobile and mobile zone becomes

$$\int_0^\infty c_{imD}(x_D, t_D) dt_D \Big/ \int_0^\infty c_{mD}(x_D, t_D) dt_D = \mathcal{L}\{g\}(s)|_{s=0} \tag{3.26}$$

For the sequential reaction case, the immobile region equations in steady state follow

$$\begin{aligned} 0 &= \alpha(c_{mA} - c_A) - k_1 c_A \\ 0 &= \alpha(c_{mB} - c_B) + k_1 c_A - k_2 c_B \\ 0 &= \alpha(c_{mC} - c_C) + k_2 c_B \end{aligned} \tag{3.27}$$

From equation (3.27) we can obtain

$$\begin{aligned} c_A &= \frac{\alpha c_{mA}}{(\alpha + k_1)} \\ c_B &= \frac{\alpha c_{mB} + k_1 c_A}{(\alpha + k_2)} \\ c_C &= \frac{\alpha c_{mC} + k_2 c_B}{\alpha} \end{aligned} \tag{3.28}$$

Assuming $c_{mB} = c_{mC} = 0$, from equation (3.28) we can obtain the analytical solution of each species in steady state

$$\frac{c_A}{c_{mA}} = \frac{\alpha}{(\alpha + k_1)} \tag{3.29}$$

$$\frac{c_B}{c_{mA}} = \frac{\alpha k_1}{(\alpha + k_1)(\alpha + k_2)}$$

$$\frac{c_C}{c_{mA}} = \frac{k_1 k_2}{(\alpha + k_1)(\alpha + k_2)}$$

In Figure 3.2, we present the steady state of species A, B and C in different immobile regions. Note that the sum of concentrations A, B and C equals one. This reflects the fact that this sum has a conservative behavior, because $r_A + r_B + r_C = -k_1 c_A + k_1 c_A - k_2 c_B + k_2 c_B = 0$ (see section 3.3.2) and the fact that in steady state the concentration of a conservative species in the mobile zones equals that in all immobile zones. Also note, that the species A (blue) can be found in immobile zones with residence times smaller than the characteristic reaction time of the first reaction ($\tau_\alpha < \tau_{r1} = 1/k_1$), species B (red) in those with residence times between the reaction times of the two reactions ($\tau_{r2} < \tau_\alpha < \tau_{r2} = 1/k_1$) and species C (yellow) in those with residence times larger than the reaction time of the second reactions ($\tau_\alpha < \tau_{r1}$). In fact, it resembles Figure 3.10. The only difference is that, in the latter the existence of either species is limited by the overall time, that is, species only exist at immobile zones smaller than the overall time ($\tau_\alpha < t$).

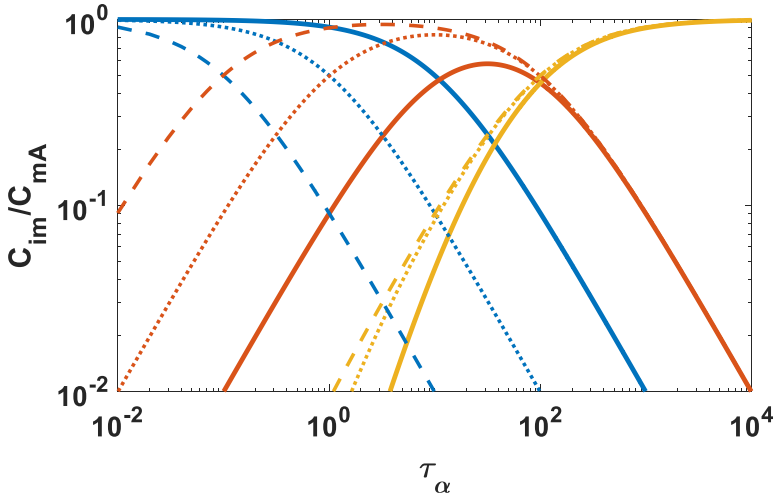

Figure 3.2 Steady state concentrations of species A (blue color), B (red color), and C (yellow color) as a function of residence time in immobile zones, τ_α[T], assuming that mobile concentrations of B and C are zero. First rate constant, k_1 [T^{-1}], for A→B transformation equals 0.1 (solid lines), 1 (dot lines), and 10 (dash lines). The rate constant, k_2 [T^{-1}], for B→C reaction is 0.01.

3.3.4 Model verification

The analytical solution is verified by the numerical results in section 3.4.2 (see Figure 3.3). It confirms that the final steady sate depends on the reaction time and the distribution of residence times in immobile regions simultaneously. In the regions $t_{rD} \gg \tau_{\alpha D}$, the ratios are almost one. In the regions $t_{rD} \approx \tau_{\alpha D}$, the ratios become to decrease from one to zero. In the regions $t_{rD} \ll \tau_{\alpha D}$, the ratios are almost zero.

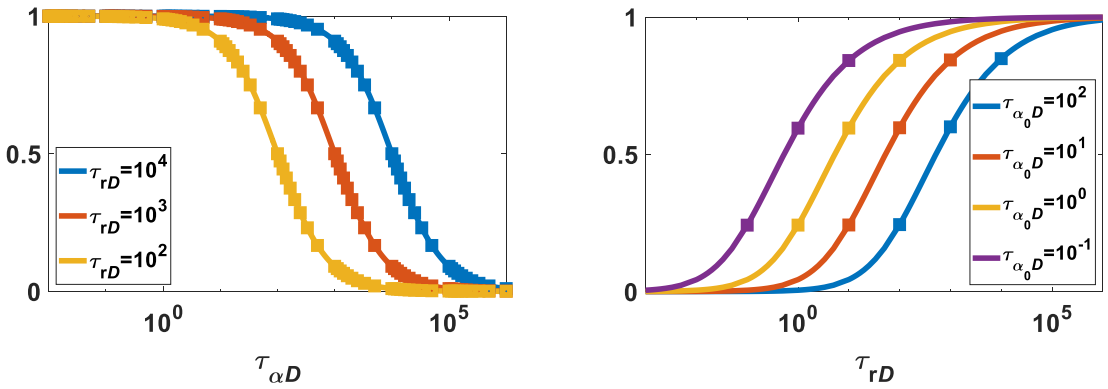

Figure 3.3 The ratios between the cumulative concentration in immobile zones and mobile zone for reactant species A (left) in immobile zones characterized by the residence times and (right) at different reaction times. The solid lines represent the analytical solutions, and the squares represent the numerical solutions.

3.4 Results

3.4.1 No reaction system

Results for the conservative transport case are summarized in Figure 3.4 and Figure 3.5. The breakthrough curves (Figure 3.4) are displayed both in arithmetic and logarithmic scale. The log-log scale is usually preferred for tracer test analysis, because it emphasizes tailing. The late time slope of the pulse BTC is that of the memory function plus 1. Therefore, by analyzing the BTC, modelers can gain insight into the nature of the immobile zones. Tailing can be also observed in the arithmetic scale plot by looking at the time of peak concentration. For slow exchange (low $\tau_{\alpha_0 D}$), most of the solute mass pulse flows in the mobile region. The opposite occurs for fast exchange, which allows equilibrating concentration in the mobile and immobile zones, so that the medium behaves as if the whole porosity was mobile. It is important to notice the above separation between fast and slow is relative to the advective transport time ($t_{Am} = Lq_m/\phi_m$, where L is the travel distance of solute). If $t_A \gg \tau_\alpha$, the immobile region becomes accessible to the solute and the actual travel time reflects the total porosity ($t_{AT} = Lq_m/\phi$, where $\phi = \phi_m + \phi_{im}$ is the total porosity).

The effect of tailing is somewhat less dramatic for a continuous injection (cumulative concentration of a pulse). The breakthrough curve approaches asymptotically the input concentration (c_e) with the bulk of solute arising at t_{Am}. This kind of observations may explain why non-local models are less popular in unconsolidated, granular, aquifers than in fractured media. Fractured media with diffusion lengths of the order of meters will display residence times of the order $t_D = L^2/D = (10m)^2/10^{-10}m^2/s \cong 10^{12}s \cong 3.10^5 years$. That is, diffusion is never exhausted. Diffusion lengths in porous media are less than 1cm, so that residence times in immobile zones will be of the order of $t_D = (10^{-2}m)^2/10^{-10}m^2/s = 10^6 s \sim 4\ months$. This time may be relevant for tracer tests, where travel time is of a few days, but is too short for natural groundwater flow. Support for this kind of observations is provided by Guimerà and Carrera (2000). They observed that the "advective porosity" (i.e. the porosity derived from the peak arrival time) calculated from a broad collection of tracer tests in fractured rocks correlates with the peak arrival time. This implies that the mobile porosity increases when the flow rate is reduced, which we take as indicative of fast immobile regions equilibrating with truly mobile zones. Increasing the travel time causes and increasing fraction of immobile regions to equilibrate with mobile zones, thus becoming effectively mobile.

Further insight into the behavior of conservative solutes can be gained from Figure 3.5, which displays the concentration in the immobile regions versus distance. The figure is somewhat misleading the

immobile porosity associated to small residence times (recall pdf of immobile zones for a gamma distribution). Still, as shown in Figure 3.2 the concentration in immobile regions is independent of their volumetric fraction. What Figure 3.5 shows is that concentrations in the immobile zones with short residence times (much shorter than travel time, 300 dimensionless units in Figure 3.5) are identical to concentrations in the mobile zone. On the other hand, concentration is negligible in the immobile zones whose residence time is much larger than travel time. This might suggest that slow immobile regions might be neglected, whereas fast immobile regions might be lumped with the mobile domain. While this may be appropriate for inert tracers, it may not for reacting tracers because reactivity is usually higher in the immobile regions, certainly in the case of biofilms (Taylor & Jaffé, 1990; Seifert & Engesgaard, 2007; Kone et al., 2014), which motivates our work.

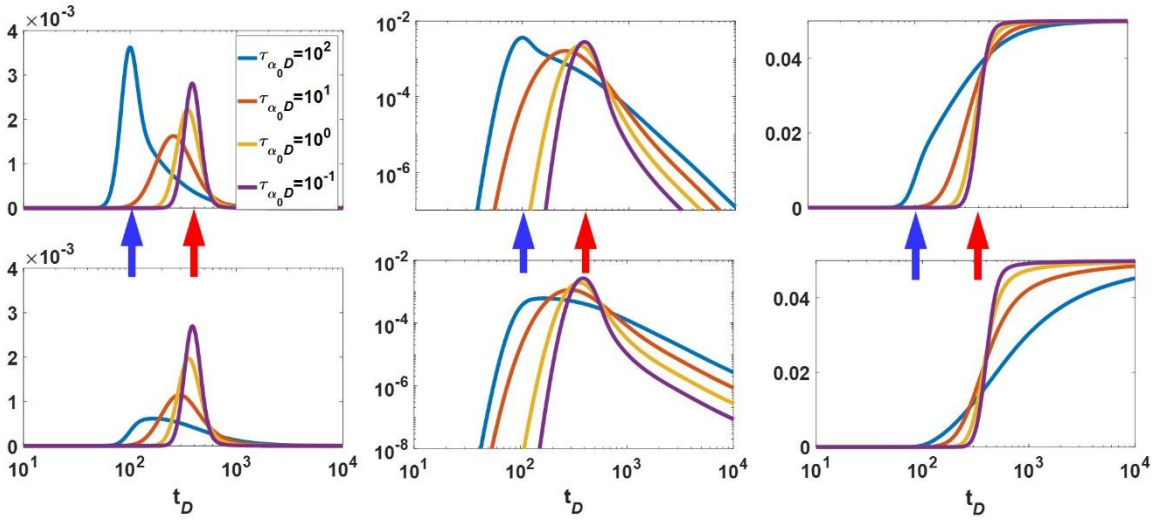

Figure 3.4 Mobile (top row) and average immobile (bottom row) concentrations versus time at $x_D = 100L_c$ in response to a pulse input (left in arithmetic scale, center in log scale) and to a continuous injection (right) for transport in a medium with a distribution residence times in immobile zones with $\beta = 1/2$, $\tau_{\alpha_0 D} = 10^2$, 10^1, 10^0, and 10^{-1}. The log-scale enhances the BTC tail (note vertical scale), which is only relevant in this case for $\tau_{\alpha_0 D} = 10^2$. When exchange with the immobile zones is slow (i.e, large $\tau_{\alpha_0 D}$), the BTC peaks at the advective time in the mobile zone ($t_D = 100$, indicated by blue arrows). The peak occurs at the advective time for the full porosity ($t_D = 400$, red arrows) when axchange is fast, which also reduces the time it takes for immobile zones to equilibrate with inflow water.

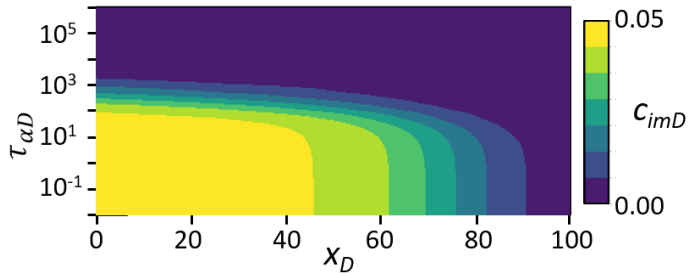

Figure 3.5 Cumulative immobile scaled concentration profiles versus dimensionless distance and dimensionless residence times (pdf with $\beta = 1/2$ and $\tau_{\alpha_0 D} = 10^{-1}$) at $t_D = 300$. Note that immobile concentrations are identical to mobile concentrations for $\tau_{\alpha D} < 10^{-1}$.

3.4.2 Single reaction system

Results for the case of two solutes, A and B, where B is produced by the degradation of A, are shown in Figure 3.6 and Figure 3.7 for several characteristic reaction times. The situation is now more

complicated than in the conservative transport case because two sets of characteristic times are involved (residence times in immobile regions and reaction times). The first immediate observation, is that BTC concentrations are reduced when the reaction rate is increased (i.e., when the characteristic reaction time is reduced). Note that BTC concentrations become negligible when transport time is much larger than the reaction time.

The behavior of concentrations in the immobile regions may be less intuitive (see Figure 3.8). Concentration of the parent species, A, is negligible in regions where residence time is much larger than the reaction time ($\tau_{\alpha D} \gg \tau_{rD}$) because the solute diffusing into these regions is degraded before a significant concentration can build up. On the other extreme, concentration in fast immobile regions is virtually equilibrated with the mobile concentration.

More interesting is the behavior of species B, which is washed away from the mobile region and fast immobile regions before it becomes significant. As a result, B concentrations are significant only in immobile regions where residence time is comparable to the characteristic reaction time.

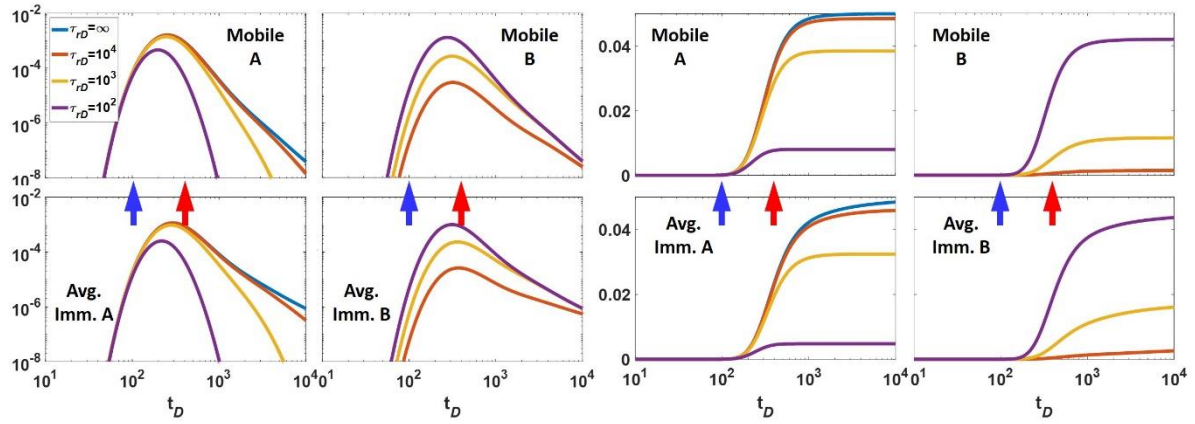

Figure 3.6 Mobile (top row) and average immobile (bottom row) concentrations of species A (first and third columns) and B (second and fourth columns) versus time at $x_D = 100L_c$ in response to a pulse input (left two columns) and to a continuous injection (right columns) for transport in a medium with a distribution residence times in immobile zones with $\beta = 1/2$, and $\tau_{\alpha_0 D} = 10^1$, and reaction times are uniformly distributed in immobile zones with $\tau_{rD} = \infty$, 10^4, 10^3 and 10^2. Species B is absent when no reaction occurs.

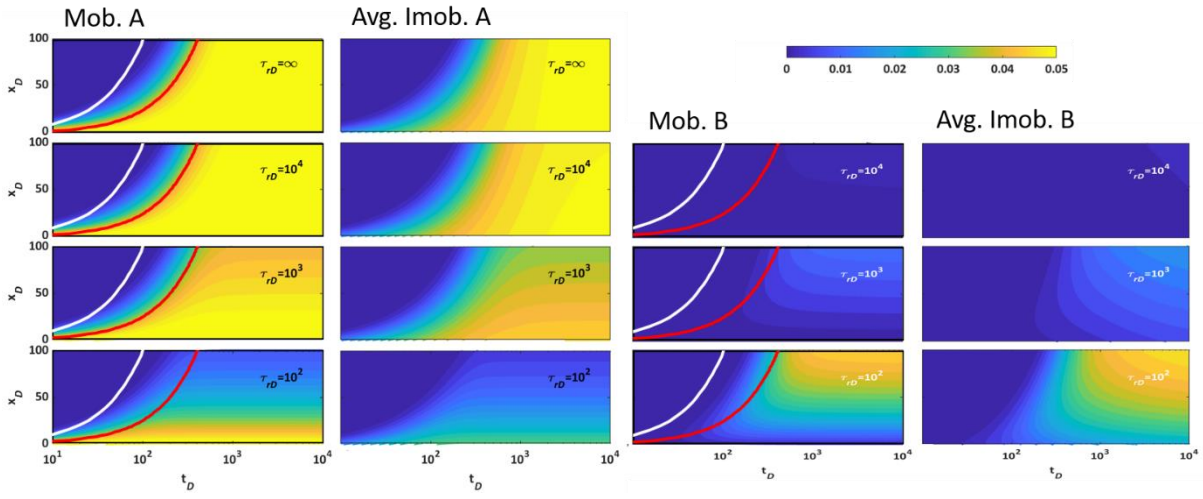

Figure 3.7 Cumulative mobile and averaged immobile concentration profiles versus dimensionless time and dimensionless distance for species A (left two columns) and B (right two columns). Species transport in a medium characterized by the immobile zones in which the residence time follows gamma

distribution with $\beta = 1/2$, $\tau_{\alpha_0 D} = 10^1$. The reaction times are uniform in immobile zones with $\tau_{rD} = \infty$, 10^4, 10^3 and 10^2 from top to bottom.

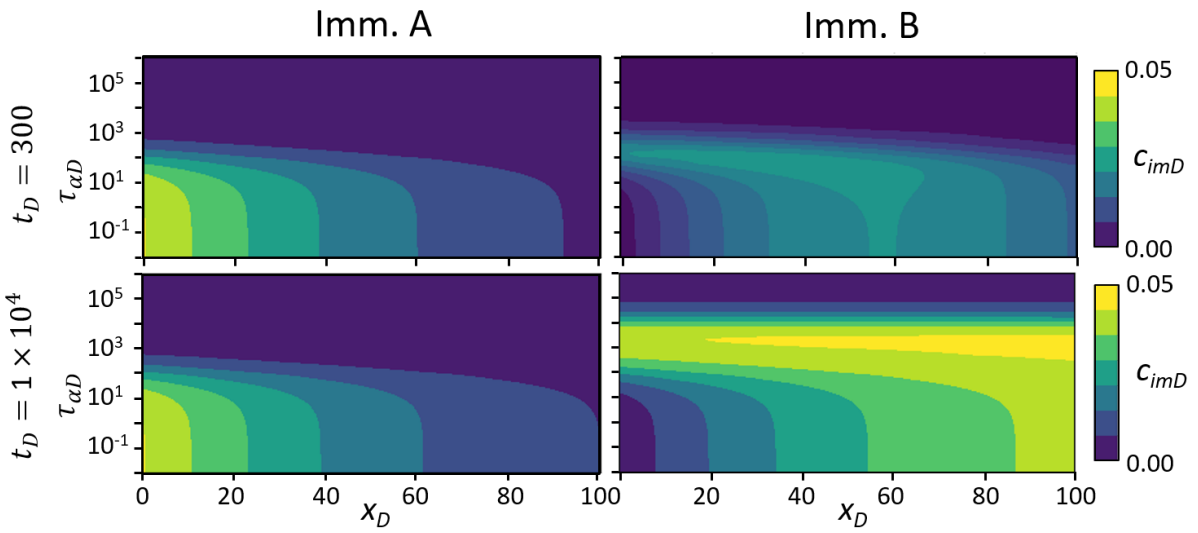

Figure 3.8 Cumulative concentration profiles versus dimensionless distance and dimensionless residence times for species A (left) and B (right) at $t_D = 300$ (above), and 1×10^4 (below) from top to bottom after continuous injection of A in a medium with immobile zones distributed with $\beta = 1/2$, $\tau_{\alpha_0 D} = 10^1$. Reaction A→B occurs with a characteristic time $\tau_{rD} = 10^2$.

3.4.3 Sequential reaction system

Results for the sequential reactions case (A→B and B→C) are summarized in Figure 3.9 and Figure 3.10. Figure 3.9 makes it clear that BTCs for mobile-immobile regions with short residence times are identical to BTCs where all the porosity is mobile. That is, immobile regions with short residence time (compared to transport time) can be lumped in the mobile region, if reactivity is the same in both types of regions. Otherwise (i.e., when reactions occur primarily in the immobile region), all fast reactions can be lumped into a simple immobile region (a complete set of BTCs for several τ_{rD} and $\tau_{\alpha 0 D}$ is presented in Appendix C).

The most significant observation derives from Figure 3.10, which displays immobile regions concentrations as a function of space and residence time. This figure makes it clear that C concentrations are only relevant in immobile regions with residence times comparable to characteristic reaction times, regardless of the transport time. Therefore, the three sets of times (transport time, reaction time, and residence times) are relevant when deciding the appropriate discretization of residence times.

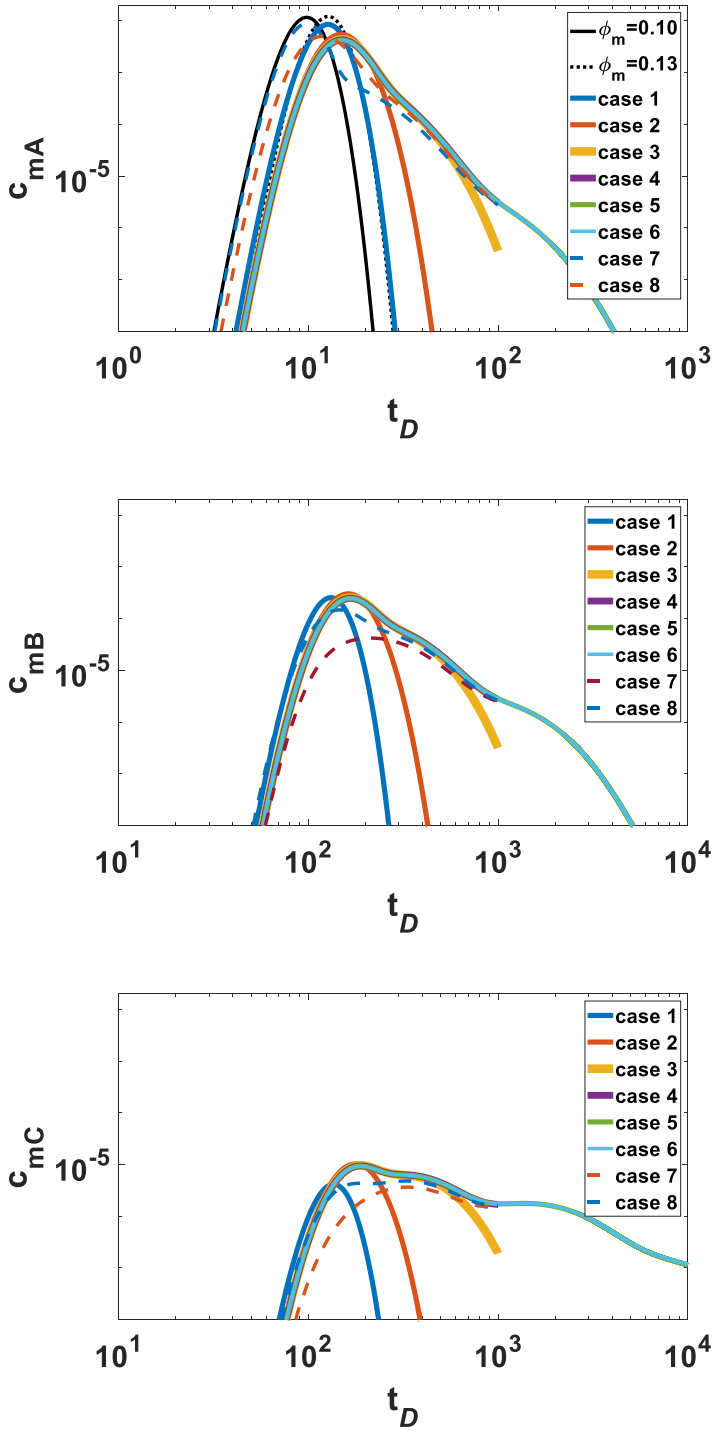

Figure 3.9 Breakthrough curves of species A, B and C in different cases for $\tau_{r1_D} = \tau_{r2_D} = 10^3$. The black lines represent results only with mobile zone. Case 1: $\tau_{\alpha D} = [10^0]$, case 2: $\tau_{\alpha D} = [10^0, 10^1]$, case 3: $\tau_{\alpha D} = [10^0, 10^1, 10^2]$, case 4: $\tau_{\alpha D} = [10^0, 10^1, 10^2, 10^3]$, case 5: $\tau_{\alpha D} = [10^0, 10^1, 10^2, 10^3, 10^4]$, case 6: $\tau_{\alpha D} = [10^0, 10^1, 10^2, 10^3, 10^4, 10^5, 10^6]$, case 7: $\tau_{\alpha D} = [10^2, 10^3]$ and case 8: $\tau_{\alpha D} = [10^1, 10^2, 10^3]$.

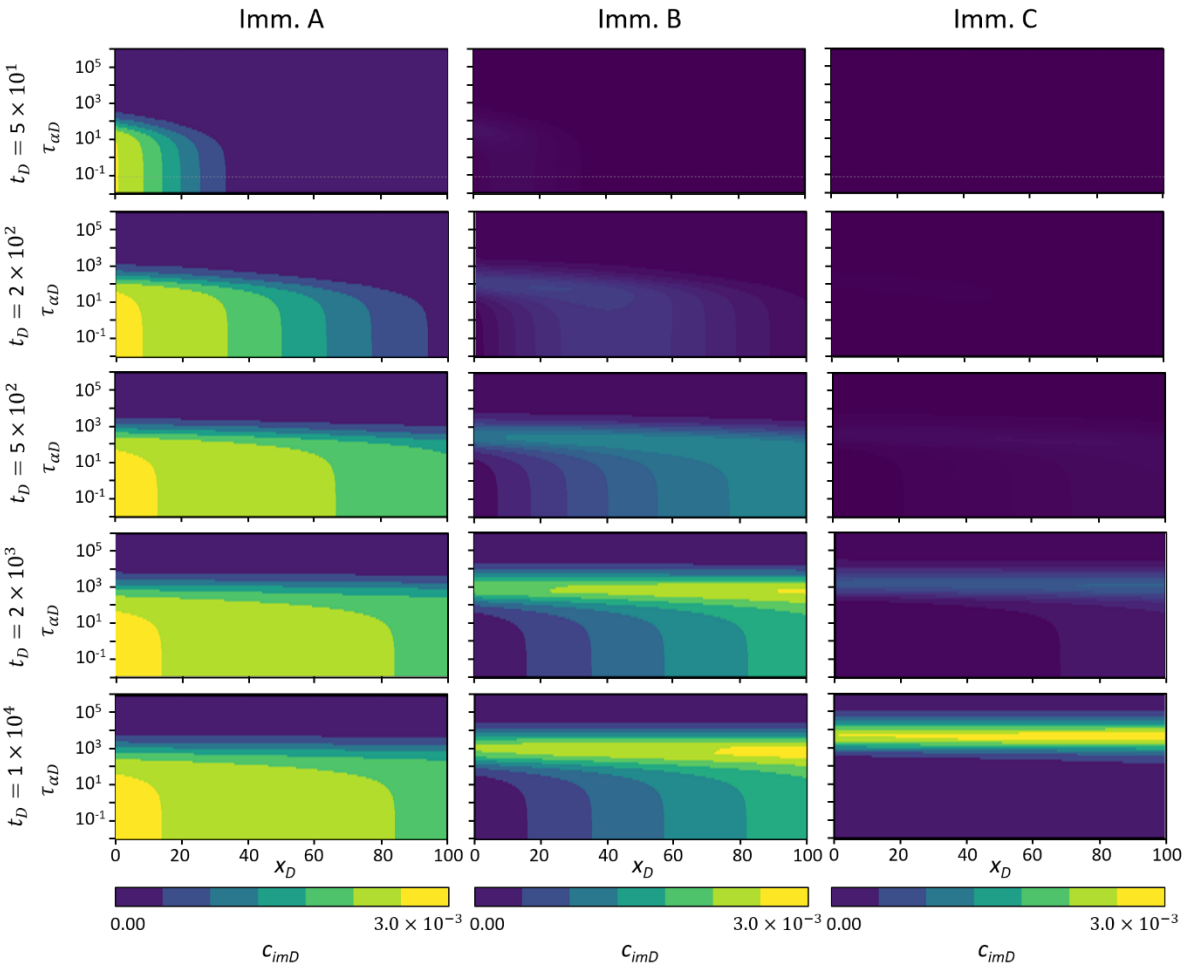

Figure 3.10 Cumulative concentration profiles versus dimensionless distance and dimensionless residence times for species (left) A, (middle) B and (right) C for $\tau_{r1_D} = \tau_{r2_D} = 10^3$ at $t_D = 50$, 200, 500, 2000 and 1×10^4 from top to bottom. Species transport in a medium characterized by the immobile zones in which the residence time follows gamma distribution with $\beta = 1/2$, $\tau_{\alpha_o D} = 10^1$.

3.5 Conclusions

Several conclusions can be drawn from the modeling exercise presented in this work

1) Some reactions may occur in immobile regions that would not occur if the entire medium was mobile. This is not surprising when the mineral composition is different in each immobile zone, as was discussed by Soler-Segarra et al (2016). What we show here is that, independently of the reactivity of mobile and immobile regions, the interplay between residence times and reaction times may cause some reactions to take place solely in the immobile region. This will occur whenever residence time is comparable to reaction time, and both are much longer than the transport time. It goes without saying that immobile region reactions will be enhanced if reactivity in immobile regions is higher than in the mobile region. This is the case for biofilms, where microbial mediated degradation reactions concentrate.
2) Regardless of reaction rates, concentrations in the fast immobile regions (i.e., regions where $\tau_\alpha \ll t_t = L\phi/q$) will tend to equilibrate with mobile concentrations. Therefore, little is gained by representing them explicitly in a model. All fast exchange immobile regions can be lumped into a zone with residence time slightly smaller than transport time.

3) Similarly, very slow immobile zones ($\tau_\alpha \gg t_t$) can be ignored because little mass will diffuse into them. Note that this conclusion is more relevant for laboratory experiments or short tracer tests, where transport forms are moderate. Under natural conditions, transport time can be very long (many years), so that most immobile regions are indeed accessible.

4 A conceptual model for reactive transport with dynamic biofilm growth in multicontinuum media *

Biofilm growth in porous media changes the hydrodynamic properties of the medium: porosity and permeability are reduced, and dispersivity increases. However, the first arrival of breakthrough curves (BTCs) is more reduced than derived from the reduction in porosity, and the BTC tail becomes heavier. These observations suggest the need of multicontinuum models (Multirate-Mass-Transfer, MRMT) that evolve dynamically with the biofilm. The MRMT model is capable of representing reactive transport in heterogeneous porous media which facilitates the simulation of localized reactions often observed within biofilms. In this work, we present a conceptual model of reactive transport with dynamic biofilm growth based on MRMT formulations. It incorporates the microbial growth according to the stoichiometry and kinetic rate laws of biological reactions. The physical, including not only porosity, but also the distribution of residence times in immobile zones, and chemical properties are updated after the reactive transport simulations at each time. This model has been tested on laboratory data.

* This chapter is based on the manuscript Wang et al., 2021. A conceptual model for reactive transport with dynamic biofilm growth in multicontinuum media, in preparation for *Water Resource Research*.

4.1 Introduction

Biofilm growth in porous media is important for many natural and engineered environmental applications such as wastewater treatment (Nicolella et al., 2000; Lewandowski & Boltz, 2011), aquifer recharge (Kim et al., 2010), enhanced oil recovery (Raiders et al., 1989; Van Hamme et al., 2003) and in situ bioremediation of soil and aquifer contamination (Cunningham et al., 2003; Sethi & Di Molfetta, 2019). Biofilm consists of living and reproducing microbial communities. It forms when microbes adhering to the surface of grains excrete extracellular polymeric substance (EPS). EPS is a fibrous gel-type matrix composed of polysaccharides, lipids, proteins, and DNA materials (Flemming et al., 2007; Flemming & Wingender, 2010). Biofilm mainly consists of water. Microbial cells, which account for less than 10% of the dry mass, and the EPS matrix, which can account for over 90% (Satpathy et al., 2016). Microorganisms in biofilms catalyze chemical reactions (Flemming & Wingender, 2010). The metabolism of microorganisms leads to the modification of biofilm surface structure and the deposition of microbes (Esperanza Cortés et al., 2011). The complex biofilm structure and metabolism gives the biofilm a function similar to tissues in higher organisms (Costerton et al., 1995).

Models usually take microbes as an independent phase to account for biofilm growth (Chen-Charpentier, 1999; Von Der Schulenburg et al., 2009; Shafahi & Vafai, 2009). These models assume that biochemical reactions take place in the bulk mobile pore water. In reality, however, these reactions are catalyzed by microbes residing within the immobile biofilm. Moreover, the biofilm structure is very heterogeneous in space and evolves with biomass growth (Picioreanu et al., 1998; Eberl et al., 2000; Picioreanu et al., 2004). Biofilm growth is known to change the hydrodynamic properties in porous media such as reduction of porosity and permeability (Taylor et al., 1990; Cunningham et al., 1991; Von Der Schulenburg et al., 2009; Cunningham et al., 2003; Thullner, 2010), retention curve (Carles Brangarí et al., 2017), as well as dispersivity (Taylor & Jaffé, 1990b; Kone et al., 2014). As a result, it impacts the reactive transport processes, which in turn affects biofilm growth. Experimental results demonstrate that biofilm growth induces heterogeneities that affect the transport in porous media (Seifert & Engesgaard, 2007; Kone et al., 2014).

To properly simulate biofilm growth and its effects on reactive transport, a model is needed that accounts for these heterogeneities. However, biofilm growth modeling is complex, because it requires coupling it with reactive transport. The challenges include how to model reactive transport in heterogeneous media, how to model the biofilm growth, and how to couple these two processes reasonably.

As the hydraulic conductivity of biofilm is very low (Deng et al., 2013), exchange of solutes between pore water and biofilm is controlled by diffusion. Models of biofilm growth on a flat surface in constantly stirred tanks take this into account (Picioreanu et al., 2004). In porous media this has to be combined with the heterogeneity of the pore and biofilm sizes. This makes the MRMT a promising tool to model the dynamical interaction between solute transport and biofilm growth. In fact, diffusion models of mass transfer between mobile and immobile zones can also be described by a set of first-order mass transfer models (Haggerty & Gorelick, 1995).

The non-local MRMT formulation has been widely used to represent transport in heterogeneous media (Haggerty & Gorelick, 1995; Wang et al., 2005; Salamon et al., 2006; Benson & Meerschaert, 2009; Dentz et al., 2011; Fernàndez-Garcia & Sanchez-Vila, 2015; De Dreuzy & Carrera, 2016). In addition, Willmann et al. (2010) obtained quite accurate agreement between 2D heterogeneity and 1D MRMT, which demonstrates that the non-local MRMT formulation of conservative transport can be extended to reactive transport. The MRMT model allows the localized modeling of reactive transport in physical and chemical heterogeneous porous media (Soler-Sagarra et al., 2016; Babaei & Islam, 2018). The physical and chemical heterogeneity are characterized by a distribution of mass transfer rates and reactions rates (or residence times and reaction times) in immobile zones.

The major challenge is that biofilm growth causes the heterogeneity of porous media to change. In fact, it is clear that velocity distributions in the medium evolve as the biofilm grows. The velocity distribution becomes broad, which suggests an increase in channeling and immobile zones (Maxence Carrel et al., 2018; M. Carrel et al., 2018). Hence, the evolution of biomass distribution should be represented by the change of mass transfer rates and reaction rates in biofilm.

The objective of this work is to build a concept model of biofilm growth in the framework of MRMT. We focus on the study of biofilm growth induces effects on transport.

4.2 Conceptual models

In our concept model, we assume a biofilm consists of water and biomass i.e., EPS & microbial cells (Seifert & Engesgaard, 2007). The biofilm is represented by the various immobile zones of the MRMT approach. Solutes diffuse into biofilm and provide nutrients for the metabolism of microbes residing in the biofilm. Reactions mediated by microbes only occur in the biofilm, not in mobile water. Here, we explain the reactive transport formulation of the abiotic chemical species, and the incorporation of biofilm.

4.2.1 Reactive transport with MRMT

In MRMT model, reactive transport in mobile zone is expressed as

$$\phi_m \frac{\partial \boldsymbol{c}_m}{\partial t} = L_t[\boldsymbol{c}_m] - \sum_{j=1}^{N} \phi_{im,j}\, \alpha_j \left(\boldsymbol{c}_m - \boldsymbol{c}_{im,j}\right) + \phi_m \boldsymbol{f}_{Qm} \tag{4.1}$$

in which, ϕ_m [-], porosity of mobile water and ϕ_{im} [-], porosity of immobile water , denote the volume fraction of the mobile and immobile pore water over the total volume, respectively; $\boldsymbol{c}_m$ [ML^{-3}] and $\boldsymbol{c}_{im,j}$ [ML^{-3}], arrays of concentrations of all aqueous species in the mobile and jth immobile zone, denote the mass of a species per unit volume of mobile water and immobile water. $L_t[\boldsymbol{c}_m] = -\boldsymbol{q}_m \nabla \boldsymbol{c}_m + \nabla \cdot (\phi_m \boldsymbol{D}_m \nabla \boldsymbol{c}_m)$ is the transport operator that describe the advection and dispersion processes, $\boldsymbol{q}_m$ [LT^{-1}] is Darcy flux, $\boldsymbol{D}_m$ [L^2T^{-1}] is the hydrodynamic dispersion tensor that includes the molecular diffusion and the mechanical dispersion. The second term on the right-hand side of equation (4.1) describes the mass transfer between mobile water and immobile water. α_j [T^{-1}] is a first-order mass transfer rate between the mobile and jth immobile zone. $\phi_{im,j} = \phi_{im} p_j$, where p_j is the probability of the jth immobile zone. The sum of p_j of all immobile zones should be equal to one, that is, $\sum_{j=1}^{N} p_j = 1.0$. $\boldsymbol{f}_{Q_m}$ [$ML^{-3}T^{-1}$] is the sink-source term due to reactions in the mobile zone which is the mass removed $\boldsymbol{f}_{Q_m} < 0$ or added $\boldsymbol{f}_{Q_m} > 0$ by reactions per unit volume of mobile water per unit of time.

In the immobile zone, the mass balance is described by

$$\frac{\partial \boldsymbol{c}_{im,j}}{\partial t} = \alpha_j \left(\boldsymbol{c}_m - \boldsymbol{c}_{im,j}\right) + \boldsymbol{f}_{Q_{im,j}} \quad j = 1, \cdots, N \tag{4.2}$$

in which, $\boldsymbol{f}_{Q_{im,j}}$ [$ML^{-3}T^{-1}$] is the sink-source term of the jth immobile zone and corresponds to the mass removed or added by biochemical reactions per unit volume of immobile water and per unit of time, and N is the number of immobile zones.

Equations (4.1) and (4.2) need to be complemented with the mass balance of non-mobile species (biomass, minerals, sorbed species). These additional mass balances are identical to those of aqueous species, but neglecting transport terms (advections, diffusion, and exchange)

The basic equations for biochemical sink/sources can be expressed as a function of reaction rates (Steefel & MacQuarrie, 1996; Saaltink et al., 1998)

$$\boldsymbol{r} = \boldsymbol{S}_e^T \boldsymbol{r}_e + \boldsymbol{S}_k^T \boldsymbol{r}_k \tag{4.3}$$

where $\boldsymbol{S}_e$ is the stoichiometric matrix for equilibrium reactions, and $\boldsymbol{S}_k$ is the stoichiometric matrix for kinetic reactions, $\boldsymbol{r}_e$ and $\boldsymbol{r}_k$ represent the vectors of reaction rates for equilibrium and kinetic reactions, respectively. Note that these matrices contain the full description of the chemical system, as every row contains the stoichiometric coefficients of all species (columns) participating in the reaction. In the case of biofilm growth, these species may include biomass, whose level of detail depends on the specific model, as well as electron acceptors and donors.

Solving the system of equations (4.1), (4.2) and (4.3), including the mass balance of non-mobile species, require complementing these equations with the Mass Action Law for equilibrium reactions and empirical expressions. Solution can be complex, but it is greatly simplified by introducing the component matrix $\boldsymbol{U}$ to eliminate the equilibrium reactions and reduce the number of unknowns in the governing equations (4.1) and (4.2). It is the kernel of $\boldsymbol{S}_e^T$, defined as $\boldsymbol{U}\boldsymbol{S}_e^T = \boldsymbol{0}$ (Saaltink et al., 1998; Molins et al., 2004). Multiplying equation (4.1) and (4.2) by the component matrix $\boldsymbol{U}$, we obtain the governing equations of the components, $\boldsymbol{u} = \boldsymbol{U}\boldsymbol{c}$ that is

$$\phi_m \frac{\partial \boldsymbol{u}_m}{\partial t} = L_t[\boldsymbol{u}_m] - \sum_{j=1}^{N} \phi_{im,j}\, \alpha_j \left(\boldsymbol{u}_m - \boldsymbol{u}_{im,j}\right) + \phi_m \boldsymbol{U}\boldsymbol{S}_k^T \boldsymbol{r}_{k,m} \tag{4.4}$$

$$\frac{\partial \boldsymbol{u}_{im,j}}{\partial t} = \alpha_j \left(\boldsymbol{u}_m - \boldsymbol{u}_{im,j}\right) + \boldsymbol{U}\boldsymbol{S}_k^T \boldsymbol{r}_{k,im,j} \quad j = 1, \cdots, N \tag{4.5}$$

4.2.2 Biofilm growth

In this study we simplify the biochemistry by two kinetic reactions: the growth of microbes or biomass (*b*) through a redox reaction involving an electron donor (*D*) and acceptor (*A*) and the death of biomass. Other chemical species, such as inorganic carbon, are not considered. Then, the stoichiometric matrix for kinetic reactions becomes:

$$\boldsymbol{S}_k = [-S_D \quad -S_A] \tag{4.6}$$

where S_D and S_A are stoichiometric coefficients. We do not consider equilibrium reactions, which means that matrix $\boldsymbol{U}$ equals the identity matrix.

The mass balances of non-mobile species. The metabolism of microbes in biofilm induces the growth and decay of biofilm which is given by

$$\rho_b \frac{\partial \phi_{b,im,j}}{\partial t} = r_{b,im,j} \phi_{b,im,j} \tag{4.7}$$

where ρ_b [ML^{-3}] is the molar density of biomass (biomass per unit volume of biofilm), $\phi_{b,im,j} = \phi_{im,j}/\theta_b$ [-] is the volume of biofilm in the jth immobile zone per unit volume of porous medium, θ_b is the volume ratio of immobile water in the biofilm, and $r_{b,im,j}$ [$ML^{-3}T^{-1}$] is the growth rate of microbes corresponding to the mass growth of microbes per unit volume of biofilm per unit of time that can be expressed as (Cirpka et al., 1999; Rodríguez-Escales et al., 2016)

$$r_{b,im,j} = Y r_{k,im,j} - d\rho_b \tag{4.8}$$

where Y [-] is the yield coefficient which denotes the production of microbes per unit mass of substrate (electron donor), d [T^{-1}] is the death rate, $r_{k,im,j}$ [$ML^{-3}T^{-1}$] is the degradation rate of substrate (electron acceptor) catalyzed by microbes, which can be represented by the Monod kinetics equation (Rodríguez-Escales et al., 2016)

$$r_{k,im,j} = \mu \frac{c_{D,im,j}}{K_D + c_{D,im,j}} \frac{c_{A,im,j}}{K_A + c_{A,im,j}} \rho_b \tag{4.9}$$

where μ [T^{-1}] is the maximum growth rate, $c_{D,im,j}$ [ML^{-3}] and $c_{A,im,j}$ [ML^{-3}] are the concentrations of electron donor and electron acceptor in biofilm, K_D [ML^{-3}] and K_A [ML^{-3}] are the half saturation constants for species of electron donor and electron acceptor, respectively.

The solution of equation (4.7) is

$$\phi_{b,im,j}(t) = \phi_{b,im,j}(t=0) e^{\frac{r_{b,im,j}}{\rho_b} t} \tag{4.10}$$

It is an exponential function with its exponent depending on the microbial growth rate and molar density that equals to

$$\frac{r_{b,im,j}}{\rho_b} = Y\mu \frac{c_{D,im,j}}{K_D + c_{D,im,j}} \frac{c_{A,im,j}}{K_A + c_{A,im,j}} - d \tag{4.11}$$

4.3 Simulation methods

The simulation follows a time marching scheme. At each time step, it mainly consists of two steps: reactive transport simulation and model update caused by biofilm growth.

4.3.1 Reactive transport

We use the finite element method (FEM) to discretize the governing equations (4.4) and (4.5). Then we apply the Newton-Raphson method to solve the global non-linear equations (Wang et al., 2021, Chapter2). The reactive transport simulation is implemented by the code RT_MRMT_DSA developed by Wang et al. (2021, Chapter 2), which is coupled to biofilm growth by updating the hydrodynamic properties of porous media and the local residence time in the different portions of the biofilm. These two simulations are run sequentially. The reactive transport simulation solves the state variables of c_m, $c_{im,j}$, $r_{k,m}$, $r_{k,im,j}$ and $r_{b,im,j}$ at each mesh node.

4.3.2 Model update

At each time step, the growth of the volume fraction of biofilm is updated according to equation (4.7), that is

$$\Delta\phi_{b,im,j} = \phi_{b,im,j}(t) \frac{r_{b,im,j}(t)}{\rho_b} \Delta t \quad j = 1, \cdots, N \tag{4.12}$$

The increase of the volume fraction of the jth immobile water is the contribution of all microbial species in which,

$$\Delta\phi_{im,j} = \theta_b \sum_{b=1}^{N_b} \Delta\phi_{b,im,j} \quad j = 1, \cdots, N \tag{4.13}$$

where N_b is the number of microbial species.

At each mesh node, the increase of the total volume fraction of immobile water is the sum of all the fractions of the volume of immobile water, which is

$$\Delta\phi_{im} = \sum_{j=1}^{N} \Delta\phi_{im,j} \tag{4.14}$$

The total volume fraction of the mobile water and biofilm in porous media is a constant which equals to

$$\phi = \phi_m(t=0) + \frac{\phi_{im}(t=0)}{\theta_b} \tag{4.15}$$

Therefore, the reduction of the mobile porosity induced by the biofilm growth equals the increase of the volume fraction of the biofilm, which leads to

$$\Delta\phi_m(t+\Delta t) = -\frac{\Delta\phi_{im}}{\theta_b} \tag{4.16}$$

In essence, the MRMT is defined by the distribution of residence times in immobile zones $f_\tau(\tau)$ or, equivalently, by the distribution of exchanging rates $f_\alpha(\alpha)$, where $\alpha = 1/\tau$. The point is that, as the biofilm grows, the residence times in immobile zones increases, not only because the fraction of medium occupied by biofilm increases, but also because its thickness increases. Therefore, defining the change in $f_\alpha(\alpha)$ implies describing how is the geometrix growth pattern. We propose a model based of form sequential but superimposed stages (see Appendix D and Figure 4.1).

Stage I- Lateral growth (Figure 4.1a). Initially, where biofilm only occupies a small portion of the medium, the dominant growth is lateral. This implies that the residence time hardly changes and its distribution is controlled by the pore structure (dead end pores and the like).

Stage II- Spherical growth (Figure 4.1b). We conjecture that microbial communities near grain meniscus may tend to join, both because they are subject to less shear and because there is an increased probability of EPS filaments in adjacent pores to contact. This leads to a 2/3 power low increase in residence time (see Appendix D)

Stage III- (Figure 4.1c) Increase in thickness. As the biofilm grows laterally and spherically, the majority of the growth concentrates in increasing the biofilm thickness, which causes a quadratic increase in residence time.

Stage IV- (Figure 4.1d) clogging. Its stated earlier, the permeability of the biofilm is very low, which reflects its fibrous gel nature. Therefore, when pores get filled, they become barriers to flow. At this stage, permeability is greatly reduced, which causes the flow to become highly channelized (Maxence Carrel et al., 2018; M. Carrel et al., 2018). The result is that the velocity distribution broadens, with large portions of the pore space virtually immobile, and the whole flux concentrating in the rest. Since exchange between channels is minimized, the emerging flow pattern might be best represented by a multi-advective regime. Moreover, diffusion distances increase dramatically which leads to a dramatic increase in residence time.

The resulting growth model is best expressed in terms of residence time as:

$$\tau_j(t) = \tau_j(t=0)\left[1 + \left(\frac{\phi_{im}}{\phi_{II}}\right)^{\frac{2}{3}} + \left(\frac{\phi_{im}}{\phi_{III}}\right)^{2} + \left(\frac{\phi_{im}}{\phi_{IV}}\right)^{5}\right] \tag{4.17}$$

Where each term represents a growth stage, ϕ_{II}, ϕ_{III}, and ϕ_{IV} are the immobile porosities at which each stage becomes relevant. In practice, we do not need to separate them explicitly, as each of them becomes naturally dominant at different times as the biofilm grows (Figure 4.2). Note that there is a degree of discretionality in the choice of parameters. Therefore, for now, we just tried, updating the exchange rates as

$$\alpha_j(t+\Delta t) = \alpha_j(t=0)\left(\frac{\phi_{im,j}(t+\Delta t)}{\phi_{im,j}(t=0)}\right)^{-\gamma} \quad j = 1,\cdots,N \tag{4.18}$$

in which, γ is a shape parameter that varies between 0 and 2 depending on shape of the biofilm and the manner of biofilm growth (see Appendix D). Many studies assume a constant specific surface area of biofilm, where biofilm growth leads to an increase of thickness (Tiwari & Bowers, 2001; Gaebler & Eberl, 2018; Lopez-Peña et al., 2019). According to Appendix D this gives $\gamma = 2$. However, biofilm

patterns and shape may vary and depend on the bacterial species, the characteristics of the porous structure, and the prevailing hydrodynamic and nutritional conditions (Kapellos et al., 2015). They may also depend on the biofilm volume fraction. We can divide the biofilm growth into four stages (see Figure 4.1) with each stage having a different value for γ. This can be represented by a relationship between mass transfer rate, α_j (or $\tau_{\alpha_j} = 1/\alpha_j$), and biofilm volume fraction, $\phi_{im,j}$. Of course, if all pores are occupied by biofilm, α_j will drop dramatically and γ will go to infinity (see Figure 4.2).

The corresponding probability of each immobile water is updated according to the formulation below

$$p_j(t+\Delta t) = \frac{\phi_{im,j}(t+\Delta t)}{\phi_{im}(t+\Delta t)} \quad j = 1, \cdots, N \tag{4.19}$$

which also imposes the condition $\sum_{j=1}^{N} p_j = 1.0$.

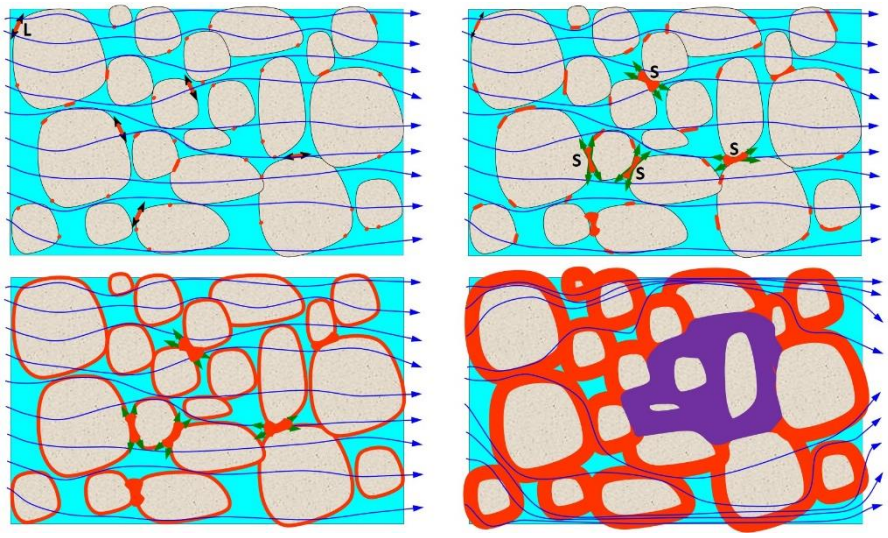

Figure 4.1 Proposed stages in ideal biofilm growth. Stage I (upper left) represent the initial situation, where a few isolated colonies (red points) tend to grow laterally (as indicated by black arrows at points L). Lateral growth continues during stage II (upper right), but spherical growth (arrows at points S) dominates in some portions. Stage III (lower left) emerges as the biofilm covers all the grains, and growth occurs primarily by thickening (red arrows at points S), although spherical growth may still occur in some places. Eventually, biofilm tends to clog the system (stage IV, lower right), so that flow lines tend to crowd the few open paths. This causes a dramatic reduction in permeability and increase in diffusion times into immobile zones, which may starve (purple zones). Changes in flow path geometries are moderate during stages I through III, although permeability may be reduced as a part of the pores is occupied by the biofilm, thus reducing its size.

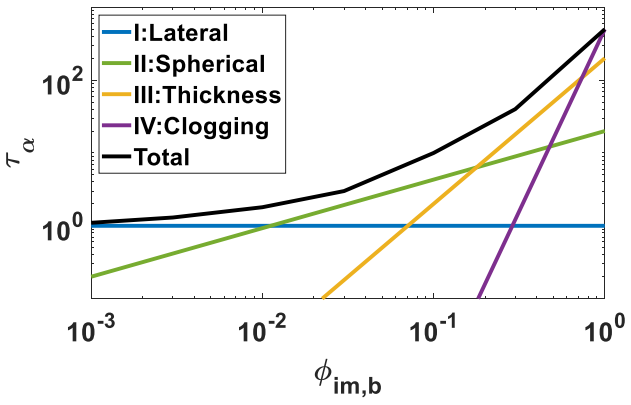

Figure 4.2 Relationship between residence time and the fraction of porous medium occupied by biofilm.

4.3.3 Algorithms

The algorithm can be explained in pseudocode as follows:

do time loop

1) do reactive transport simulations
   solve $\boldsymbol{c}_m$, $\boldsymbol{c}_{im,j}$, $\boldsymbol{r}_{k,m}$ and $\boldsymbol{r}_{k,im,j}$
   solve $\boldsymbol{r}_{b,im,j}$
2) compute the change of volume fractions $\Delta\phi_{b,im,j}$, $\Delta\phi_{im,j}$ and $\Delta\phi_m$
3) update hydrodynamic properties $\phi_{im,j}$, ϕ_{im} and ϕ_m
4) update local mass transfer rates α_j and the corresponding probability p_j
5) renew time, $t \leftarrow t + \Delta t$

end do

4.4 Applications

We used our conceptual model to analyze two small (cm to dm scale) laboratory experiments (Kone et al., 2014; Seifert & Engesgaard, 2007). Both experiments consist of porous medium columns where biofilm growth is induced by adding an electron acceptor and donor to the inlet water. At several times of the experiments, tracer tests were performed and breakthrough curves measured. The time scales of the trace tests (less than an hour) are much shorter than those for biofilm growth during the whole experiment (several tenths of days). This permits us to evaluate the changes in the mass transfer coefficients (α_j).

For the modeling of these two experiments we calibrated the rate law parameters (μ, K_D , K_A) and initial immobile porosity and mass transfer coefficients. Other parameters (θ_b, ρ_b, Y, d) are taken from literature (Satpathy et al., 2016; Bakke et al., 1984; Rittmann & McCarty, 2001). We used a constant value for γ of 2/3, which corresponds to a stage II biofilm growth.

4.4.1 Experimental data of Kone (2014)

To validate our model, we run simulations and calibrate the results with the experimental data of Kone et al. (2014). The parameters are set as shown in Table 4-1. In Figure 4.3, we present the evolution of biofilm in space and time. It shows that the biofilm grows with time and the distribution of biofilm is almost uniform in distance, which indicates the reaction rates along space are uniform as well. This distribution reflects that the input flux of electron donors and acceptors are much larger than the reaction rate in the whole system, so that the reaction rates are uniform within the immobile zones.

Figure 4.4, displays the evolution of the biofilm at x = 9 cm and plot it both in linear and semi-log scale. In the semi-log scale, the volume fraction of biofilm varies linearly over time, which confirms that biofilm growth is exponential. At 29 days, the volume fraction of biofilm reaches 0.2, which is consistent with the experiment data of Kone et al. (2014). A tracer test was performed. After the biofilm growth at 29 days, the results are shown in Figure 4.5. At first sight the model does not seem to reproduce well the experimental data of Kone et al. (2014). In fact, the mean arrival time displayed by the BTCs of Kone et al. (2014) appears to increase with residence time. This is inconsistent, the mean arrival time is given by $V_p\phi_t/Q$, where V_p is the volume of the porous medium, $\phi_t = \phi_m + \phi_{im}$ is the total porosity and Q is the flow rate. V_p and Q are constant and ϕ_t should be reduced. Therefore, the mean residence time should decrease. This mismatch might due to adsorption that could have occurred, but was not modeled. This creates additional retardation of the breakthrough curve. Note, that if we multiply the time scale of the modeled results by a factor of around 1.4, the fit would be much better. Therefore, we think that the model reproduces correctly the effect of biofilm growth on transport. Both

model and experimental results show that the biofilm growth causes the tailing of breakthrough curves. Figure 6 shows that Biofilm grows equally for all portions of immobile zones. This is due to the abundance of electron acceptors and donors in this experiment. As a result, biofilm growth is not limited by transport of these species and does not depend on the transport parameters, specific for each mobile zone.

Table 4-1 Model setup for transport and biofilm growth

Parameter	Symbol	Value
Length	L	10 cm
Initial porosity of mobile water	ϕ_m	0.39
Initial porosity of immobile water	$\phi_{b,im}$	0.01
Darcy flux	q_m	0.0133 cm/s
Longitudinal dispersivity	α_L	0.0301 cm
Initial mass transfer rates	α_j	1.0×10^{-3}, 5.0×10^{-3}, 0.02, 0.05, 0.2 s^{-1}
Initial probabilities	p_j	3.0454e-04, 0.0034, 0.0272, 0.1077, 0.8614
Coefficient	γ	2/3
Volume ratio	θ_b	0.9
Molar density of microbes	ρ_b	8.8496e-04 mol/cm^3
Yield coefficient	Y	0.3
Maximum growth rate	μ	5.4e-04 s^{-1}
Half saturation constant for ED	K_D	1.0e-02 mol/cm^3
Half saturation constant for EA	K_A	1.0e-03 mol/cm^3
Death rate	d	1.0e-07 s^{-1}
Inlet concentration for ED	c_D	1.0e-03 mol/cm^3
Inlet concentration for EA	c_A	1.0e-04 mol/cm^3

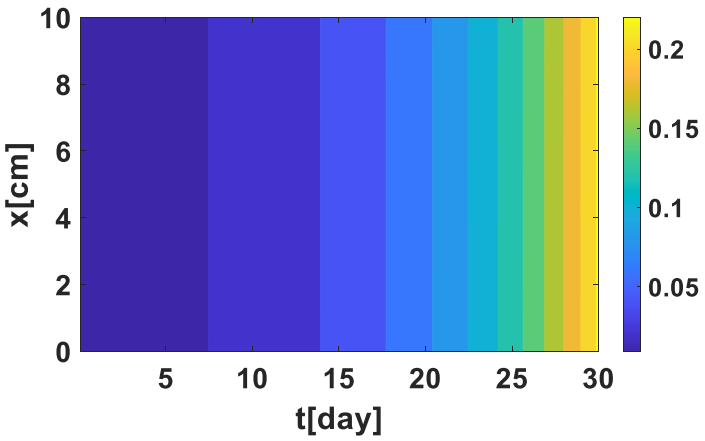

Figure 4.3 The evolution and distribution of the volume fraction of biofilm in porous media.

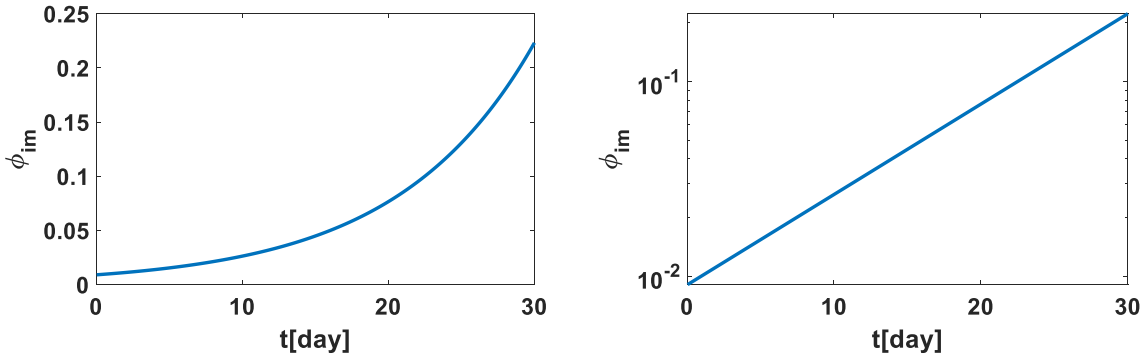

Figure 4.4 Biofilm growth curve plotted as a function of time at x = 9 cm, (left) plotted on linear scale and (right) semi-log scale.

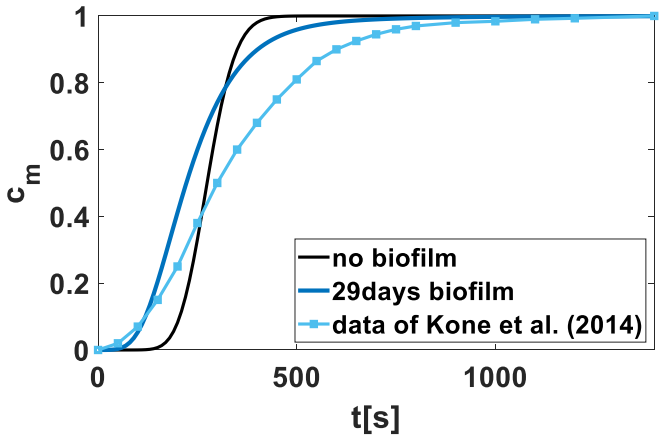

Figure 4.5 Breakthrough curves of solute at x = 9cm for continuous injection at t =29 days.

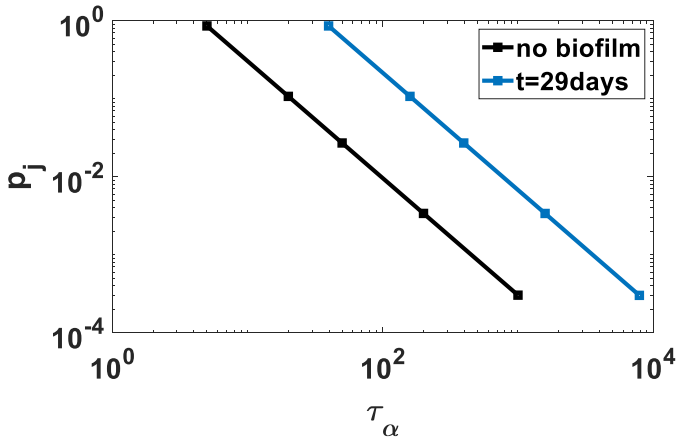

Figure 4.6 The evolution of residence times and probabilities in different portions of immobile zones during biofilm growth at t = 29 days.

4.4.2 Experimental data of Seifert (2007)

We use the experimental data of Seifert (2007) to calibrate our model. The parameters are set as shown in Table 4-2. In this model, the volume fraction of biofilm increases with time, but is not uniform in distance (see Figure 4.7).Tracer tests were performed after 13, 62 and 113 days. Our results are in agreement with the experimental data of Seifert (2007), as shown in Figure 4.8. Meanwhile, it confirms that the biofilm growth leads to the increase of residence times in immobile zones (see Figure 4.9). In

this model, the increase of residence times mainly occurs in the immobile zones with the residence times between 5 and 20 min. This is because the residence times of these immobile zones are comparable to the transport time (the time solute travel through the column) which facilitates the biofilm growth (see Figure 4.10).

Table 4-2 Model setup for transport and biofilm growth

Parameter	Symbol	Value
Length	L	5 cm
Initial porosity of mobile water	ϕ_m	0.35
Initial porosity of immobile water	$\phi_{b,im}$	0.05
Darcy flux	q_m	0.1262 cm/min
Longitudinal dispersivity	α_L	0.16 cm
Initial mass transfer rates	α_j	0.001, 0.005, 0.02, 0.05, 0.2 min^{-1}
Initial probabilities	p_j	3.0454e-04, 0.0034, 0.0272, 0.1077, 0.8614
Coefficient	γ	2/3
Volume ratio	θ_b	0.9
Molar density of microbes	ρ_b	8.8496e-04 mol/cm^3
Yield coefficient	Y	0.3
Maximum growth rate	μ	1.0e-01 min^{-1}
Half saturation constant for ED	K_D	1.0e-06 mol/cm^3
Half saturation constant for EA	K_A	1.0e-06 mol/cm^3
Death rate	d	1.0e-07 min^{-1}
Inlet concentration for ED	c_D	1.5e-07 mol/cm^3
Inlet concentration for EA	c_A	3.0e-07 mol/cm^3

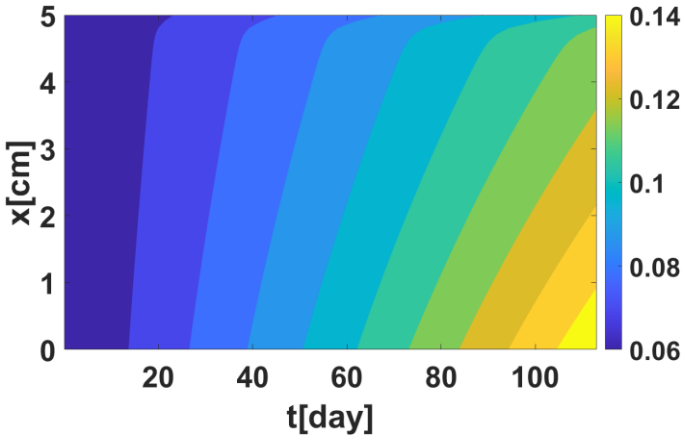

Figure 4.7 The evolution and distribution of the volume fraction of biofilm in porous media.

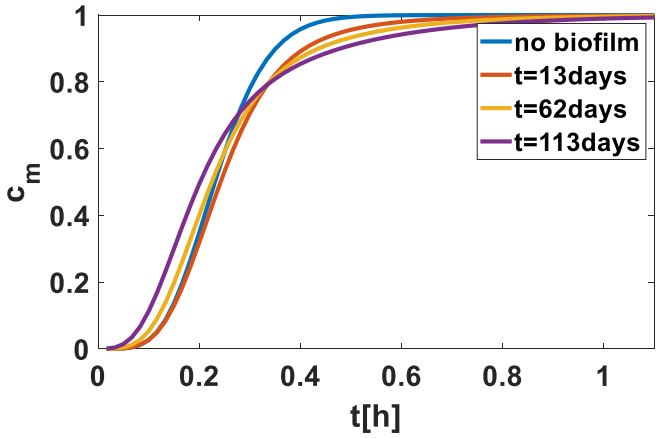

Figure 4.8 Breakthrough curves of solute at x = 5cm for continuous injection at t=13, 62 and 113 days.

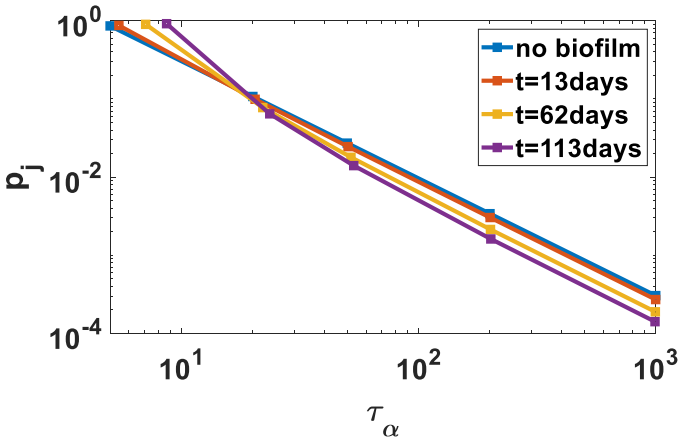

Figure 4.9 The evolution of residence times and probabilities in different portion of immobile zones during biofilm growth at x = 5cm and t = 13, 62 and 113 days.

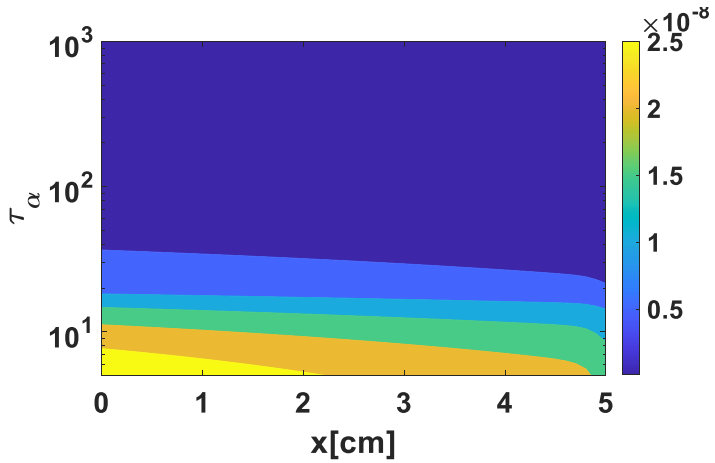

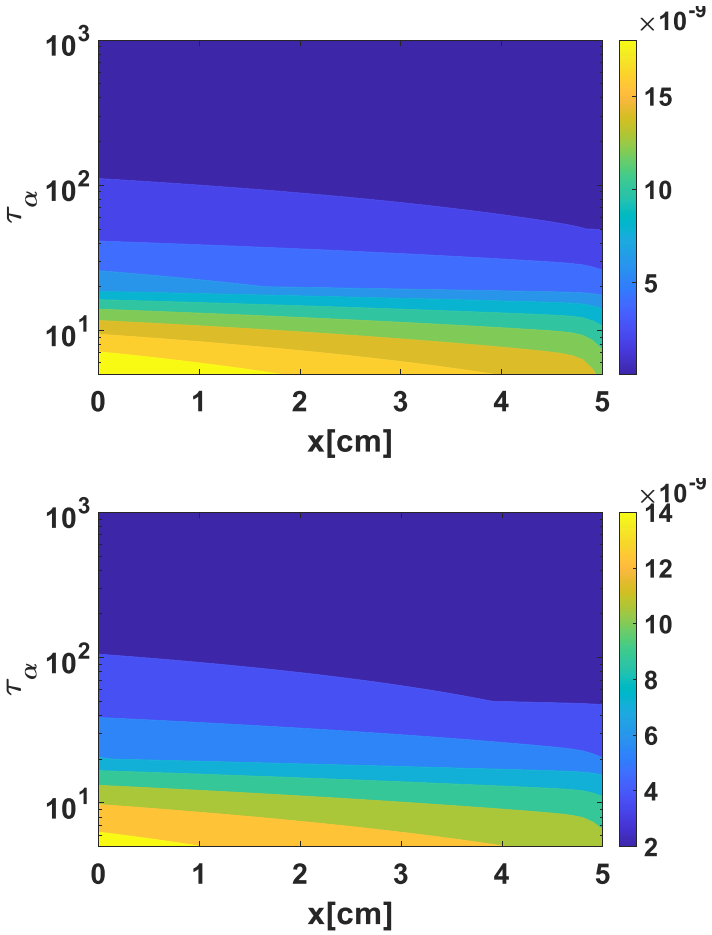

Figure 4.10 The distribution of reaction rates in space and immobile zones at t = 13, 62 and 113 days from top to bottom.

4.5 Conclusions

We have developed a conceptual model for biofilm growth based on the non-local MRMT formulation, which takes into account the changes in transport characteristics. Clearly, biofilm growth affects transport. This is shown by both the conceptual model and the experiments we used to validate the models. Although the modeled results do not agree perfectly the experiments, the model can reproduce the change in transport behavior due to biofilm growth.

We modeled two experiments, which revealed some interesting differences between the two. In the experiment of Kone et al. (2014) the abundance of electron acceptors and donors made the biofilm growth independent of transport. This caused an equal change for all immobile zone, that is, the probability density function p only shifts, but does not change its form. On the other hand, in the experiment of Seifert and Engesgaard (2007) biofilm growth is dependent on transport behavior. This causes a change probability density function p with a larger effect on the immobile zones with smaller residence time and a tendency to decrease the heterogeneity.

For both models we used a constant shape parameter $\gamma = 2/3$. This leads to an exponential biofilm growth with time. This can be seen clearly for the experiment of Kone et al. (2014), but is also true for that of Seifert and Engesgaard (2007). Obviously, the shape parameter will increase, when biofilm volume fraction approach values equal to the porosity during clogging. In that case, models should consider changes in shape parameter.

5 Conclusions

Each chapter of this thesis is independent and contains the relevant conclusions. Therefore, here I simply summarize the most salient conclusions.

In chapter 2, I presented a novel method to solve MRMT reactive transport models. The method takes advantage of the sparse nature of the system matrix that results in MRMT problems. This allows solving immobile concentrations as a function of mobile concentrations, so that the final system is only a function of mobile concentrations. The method turns out to be extremely efficient.

In chapter 3, We analyzed the interplay between characteristic reaction times, transport times and distribution of residence times. We conclude that reactions driven by species that are not present in the inflow water but are the result of previous reactions will take place in immobile zones, whose residence time is comparable to reaction times. Furthermore, immobile zones with residence times much smaller than those for transport can be lumped together (assuming that very fast reactions are assumed in equilibrium), which greatly reduces computations.

Finally, a biofilm growth model was presented in Chapter 4. The singularity of this model lies in its ability to represent the changes in residence time distributions as a result of biofilm growth. The model has been successful in reproducing tracer test experiments extracted from the literature performed in the laboratory at different stages of biofilm growth.

A. Numerical discretization of governing equations

In practice, MRMT model is substituted by a finite number of immobile zones. In this way, the continuous governing equation (2.7) and (2.8) are discretized as follows,

$$\phi_m \frac{\partial \boldsymbol{u}_m(x,t)}{\partial t} = L_t[\boldsymbol{u}_m(x,t)] - \sum_{j=1}^{N} \boldsymbol{F}_j + \phi_m \boldsymbol{R}_m(x,t) \tag{A.1}$$

$$\boldsymbol{F}_j = \phi_{im,j}\alpha_j\big[\boldsymbol{u}_m(x,t) - \boldsymbol{u}_{im,j}(x,t)\big] \tag{A.2}$$

$$\boldsymbol{R}_m(x,t) = \boldsymbol{U}\boldsymbol{S}_k^T \boldsymbol{r}_{k,m}\big(\boldsymbol{u}_m(x,t)\big) \tag{A.3}$$

$$\frac{\partial \boldsymbol{u}_{im,j}(x,t)}{\partial t} = \alpha_j\big[\boldsymbol{u}_m(x,t) - \boldsymbol{u}_{im,j}(x,t)\big] + \boldsymbol{R}_{im,j}(x,t), \qquad j = 1,\cdots,N \tag{A.4}$$

$$\boldsymbol{R}_{im,j}(x,t) = \boldsymbol{U}\boldsymbol{S}_k^T \boldsymbol{r}_{k,im,j}\left(\boldsymbol{u}_{im,j}(x,t)\right) \tag{A.5}$$

where $\boldsymbol{F}_j$ is the mass exchange between mobile and jth immobile zone, $\phi_{im,j} = \phi_{im}p_j$ is the weighted porosity in jth immobile zone, p_j is the probability for mass exchange rate α_j accounting in the jth immobile zone, N is the number of immobile zones.

To obtain the numerical discretization of the system equations, a forward finite difference method is used to discretize the first derivative in time, and the finite element method is applied to discretize the governing partial difference equations. Meanwhile, state variables are evaluated at some time between time step k and $k+1$.

The resulting discretized system equations are given below,

$$(\boldsymbol{g}_m)^i = \left(\frac{\boldsymbol{G}}{\Delta t} + \theta_t \boldsymbol{E}\right)\left(\boldsymbol{u}_m^{k+1}\right)^i - \left(\frac{\boldsymbol{G}}{\Delta t} - (1-\theta_t)\boldsymbol{E}\right)\boldsymbol{u}_m^k + \frac{\boldsymbol{G}}{\phi_m}\sum_{j=1}^{N}\left(\boldsymbol{F}_j^{k+\theta_t}\right)^i - \boldsymbol{G}\left(\boldsymbol{R}_m^{k+\theta_r}\right)^i = 0 \tag{A.6}$$

$$\left(\boldsymbol{g}_{im,j}\right)^i = \frac{\left(\boldsymbol{u}_{im,j}^{k+1}\right)^i - \boldsymbol{u}_{im,j}^k}{\Delta t} - \alpha_j\left[\left(\boldsymbol{u}_m^{k+\theta_t}\right)^i - \left(\boldsymbol{u}_{im,j}^{k+\theta_t}\right)^i\right] - \left(\boldsymbol{R}_{im,j}^{k+\theta_r}\right)^i = 0, \qquad j = 1,\cdots,N \tag{A.7}$$

in which, $\boldsymbol{E}$ is the global matrix accounting for advection and dispersion, $\boldsymbol{G}$ is the global matrix that assembles porosity in the mobile zone, i is the iteration number at each time step, $\theta_t \in [0,1]$ is a temporal weight factor for transport, and $\theta_r \in [0,1]$ is a weight factor for kinetics.

The entries of Jacobian matrix are formulated as follows,

$$\left(\frac{\partial \boldsymbol{g}_m}{\partial \boldsymbol{u}_m^{k+1}}\right)^i = \left(\frac{\boldsymbol{G}}{\Delta t} + \boldsymbol{E}\theta\right) \otimes \boldsymbol{I}_{N_u} + (\boldsymbol{G}/\phi_m)\sum_{j=1}^{N}\phi_{im,j}\alpha_j\,\theta_t \boldsymbol{I}_{N_n} \otimes \boldsymbol{I}_{N_u} - \boldsymbol{G}\theta_r\left(\frac{\partial \boldsymbol{R}_m^{k+1}}{\partial \boldsymbol{u}_m^{k+1}}\right)^i \tag{A.8}$$

$$\left(\frac{\partial \boldsymbol{g}_m}{\partial \boldsymbol{u}_{im,j}^{k+1}}\right)^i = -\phi_{im,j}\alpha_j\theta_t(\boldsymbol{G}/\phi_m)\boldsymbol{I}_{N_n} \otimes \boldsymbol{I}_{N_u} \tag{A.9}$$

$$\left(\frac{\partial \boldsymbol{g}_{im,j}}{\partial \boldsymbol{u}_m^{k+1}}\right)^i = -\alpha_j\,\theta_t \boldsymbol{I}_{N_n} \otimes \boldsymbol{I}_{N_u} \tag{A.10}$$

$$\left(\frac{\partial \boldsymbol{g}_{im,j}}{\partial \boldsymbol{u}_{im,j}^{k+1}}\right)^{i} = \left(\frac{1}{\Delta t} + \alpha_j \theta_t\right) \boldsymbol{I}_{N_n} \otimes \boldsymbol{I}_{N_u} - \theta_r \left(\frac{\partial \boldsymbol{R}_{im,j}^{k+1}}{\partial \boldsymbol{u}_{im,j}^{k+1}}\right)^{i} \tag{A.11}$$

in which, N_n is the number of mesh nodes, N_u is the number of components, $\otimes$ represents Kronecker product, $\boldsymbol{I}_{N_n}$ and $\boldsymbol{I}_{N_u}$ are identity matrix with dimensions equal to $N_n \times N_n$ and $N_u \times N_u$, respectively.

The derivatives of reaction rates with respect to components at each node are calculated according to the chain rule, that is

$$\left(\frac{\partial \boldsymbol{R}_{m}^{k+1}}{\partial \boldsymbol{u}_{m}^{k+1}}\right)^{i} = \boldsymbol{U}\boldsymbol{S}_K^T \left(\frac{\partial \boldsymbol{r}_{k,m}^{k+1}}{\partial \boldsymbol{u}_{m}^{k+1}}\right)^{i} = \boldsymbol{U}\boldsymbol{S}_K^T \left(\frac{\partial \boldsymbol{r}_{k,m}^{k+1}}{\partial \boldsymbol{c}_{\boldsymbol{1}m}^{k+1}}\right)^{i} \left[\left(\frac{\partial \boldsymbol{u}_{m}^{k+1}}{\partial \boldsymbol{c}_{\boldsymbol{1}m}^{k+1}}\right)^{i}\right]^{-1} \tag{A.12}$$

$$\left(\frac{\partial \boldsymbol{R}_{im,j}^{k+1}}{\partial \boldsymbol{u}_{im,j}^{k+1}}\right)^{i} = \boldsymbol{U}\boldsymbol{S}_K^T \left(\frac{\partial \boldsymbol{r}_{k,im,j}^{k+1}}{\partial \boldsymbol{u}_{im,j}^{k+1}}\right)^{i} = \boldsymbol{U}\boldsymbol{S}_K^T \left(\frac{\partial \boldsymbol{r}_{k,im,j}^{k+1}}{\partial \boldsymbol{c}_{\boldsymbol{1}im,j}^{k+1}}\right)^{i} \left[\left(\frac{\partial \boldsymbol{u}_{im,j}^{k+1}}{\partial \boldsymbol{c}_{\boldsymbol{1}im,j}^{k+1}}\right)^{i}\right]^{-1} \tag{A.13}$$

both are matrices of size $N_u \times N_u$.

B. Analytical solution of reactive transport in multicontinuum media for first-order kinetics in the Laplace Domain

For a chemical system satisfies $\boldsymbol{US}_k^T \boldsymbol{r}_{k,m}(x,t) = -\boldsymbol{r}_{k,m}(x,t)$, $\boldsymbol{US}_k^T \boldsymbol{r}_{k,im}(x,\alpha,t) = -\boldsymbol{r}_{k,im}(x,\alpha,t)$, and the chemical kinetics follows first-order decay, $\boldsymbol{r}_{k,m}(x,t) = \kappa \boldsymbol{u}_m(x,t)$, $\boldsymbol{r}_{k,im}(x,\alpha,t) = \kappa \boldsymbol{u}_{im}(x,\alpha,t)$, then the governing equation (2.7) and (2.8) in mobile and immobile domains simplify to be linear, that is,

$$\phi_m \frac{\partial \boldsymbol{u}_m(x,t)}{\partial t} = L_t[\boldsymbol{u}_m(x,t)] - \phi_{im} \int_0^\infty \alpha[\boldsymbol{u}_m(x,t) - \boldsymbol{u}_{im}(x,\alpha,t)] f(\alpha)\, d\alpha - \phi_m \kappa \boldsymbol{u}_m(x,t) \tag{B.1}$$

$$\frac{\partial \boldsymbol{u}_{im}(x,\alpha,t)}{\partial t} = \alpha[\boldsymbol{u}_m(x,t) - \boldsymbol{u}_{im}(x,\alpha,t)] - \kappa \boldsymbol{u}_{im}(x,\alpha,t) \tag{B.2}$$

Inserting equation (B.2) into (B.1) leads to the total governing equation, written as

$$\phi_m \frac{\partial \boldsymbol{u}_m(x,t)}{\partial t} + \phi_{im} \int_0^\infty f(\alpha) \frac{\partial \boldsymbol{u}_{im}(x,\alpha,t)}{\partial t} d\alpha = L_t[\boldsymbol{u}_m(x,t)] - \boldsymbol{r}_k(x,t) \tag{B.3}$$

in which, $\boldsymbol{r}_k(x,t)$ is the total reaction rate that integrates reactions in both mobile and immobile zones,

$$\boldsymbol{r}_k(x,t) = \phi_m \kappa \boldsymbol{u}_m(x,t) + \phi_{im} \int_0^\infty f(\alpha) \kappa \boldsymbol{u}_{im}(x,\alpha,t)\, d\alpha \tag{B.4}$$

Solving equation (B.2), we get the solution of components in the immobile zone, it is given by

$$\begin{aligned} \boldsymbol{u}_{im}(x,\alpha,t) &= \boldsymbol{u}_{im}^0 e^{-\lambda t} + \int_0^t \alpha e^{-\lambda(t-\tau)} \boldsymbol{u}_m(x,\tau)\, d\tau \\ &= \boldsymbol{u}_{im}^0 e^{-\lambda t} + \alpha e^{-\lambda t} * \boldsymbol{u}_m(x,t) \end{aligned} \tag{B.5}$$

in which, $\boldsymbol{u}_{im}^0$ is the initial condition in immobile zones, $\lambda = \alpha + \kappa$ is the decay rate that accounts for both mass exchange rate and kinetic rate.

Assuming $\boldsymbol{u}_{im}^0 = 0$, then substituting equation (B.5) into the total governing equation (B.3), we obtain the total governing equation with respect to component only in mobile zone, that is

$$\phi_m \frac{\partial \boldsymbol{u}_m(x,t)}{\partial t} = L_t[\boldsymbol{u}_m(x,t)] - \phi_{im} \left[g^0 \boldsymbol{u}_m(x,t) + \frac{\partial g(t)}{\partial t} * \boldsymbol{u}_m(x,t) + \kappa g(t) * \boldsymbol{u}_m(x,t) \right] - \phi_m \kappa \boldsymbol{u}_m(x,t) \tag{B.6}$$

in which, $g(t) = \int_0^\infty f(\alpha)\, \alpha e^{-\lambda t} d\alpha$ represents the memory function (Carrera et al., 1998).

To characterize the total governing equation (B.6), we define characteristic length and characteristic transport time, written as

$$L_c = \frac{\phi_m D}{q} \tag{B.7}$$

and

$$t_c = \frac{L_c}{v} = \frac{\phi_m^2 D}{q^2} \tag{B.8}$$

In one dimensional, the characteristic length is the longitudinal dispersivity, i.e. $L_c = \alpha_L$, due to the mechanical dispersion equals to longitudinal dispersivity multiply fluid velocity, i.e. $D = \alpha_L v$.

Introducing these characteristics into equation (B.6), the dimensionless form of the total governing equation (B.6) is obtained, it is given by

$$\begin{aligned} \frac{\partial \boldsymbol{u}_m(x_D, t_D)}{\partial t_D} = & \frac{\partial^2 \boldsymbol{u}_m(x_D, t_D)}{\partial x_D^2} - \frac{\partial \boldsymbol{u}_m(x_D, t_D)}{\partial x_D} \\ & - \eta \left[g^0 \boldsymbol{u}_m(x_D, t_D) + \frac{\partial g(t_D)}{\partial t_D} * \boldsymbol{u}_m(x_D, t_D) + \kappa_D g(t_D) * \boldsymbol{u}_m(x_D, t_D) \right] \\ & - \kappa_D \boldsymbol{u}_m(x_D, t_D) \end{aligned} \tag{B.9}$$

with the definition of dimensionless variables as

$$\eta = \frac{\phi_{im}}{\phi_m}, \qquad t_D = \frac{t}{t_c}, \qquad x_D = \frac{x}{L_c}, \qquad \kappa_D = \kappa t_c, \qquad \alpha_D = \alpha t_c, \qquad \lambda_D = \lambda t_c \tag{B.10}$$

Given the initial and boundary conditions,

$$\begin{gathered} \boldsymbol{u}_m(x_D, t_D = 0) = 0, \qquad x_D \geq 0 \\ \boldsymbol{u}_m(x_D = 0, t_D) = \boldsymbol{u}\,, \qquad \boldsymbol{u}_m(x_D = \infty, t_D) = 0, \qquad t_D > 0 \end{gathered} \tag{B.11}$$

The solution of equation (B.9) is obtained in the Laplace domain, that is

$$\mathcal{L}\{\boldsymbol{u}_m\} = \frac{\boldsymbol{u}}{s} exp\left\{ \left[1 - \sqrt{1 + 4(s + \kappa_D)(1 + \eta \mathcal{L}\{g\})} \right] \frac{x_D}{2} \right\} \tag{B.12}$$

in which, $\mathcal{L}\{\boldsymbol{u}_m\}$ and $\mathcal{L}\{g\}$ indicate the Laplace transform of $\boldsymbol{u}_m(x_D, t_D)$ and $g(t_D)$, respectively.

C. Breakthrough curves of species A, B and C for sequential reactions

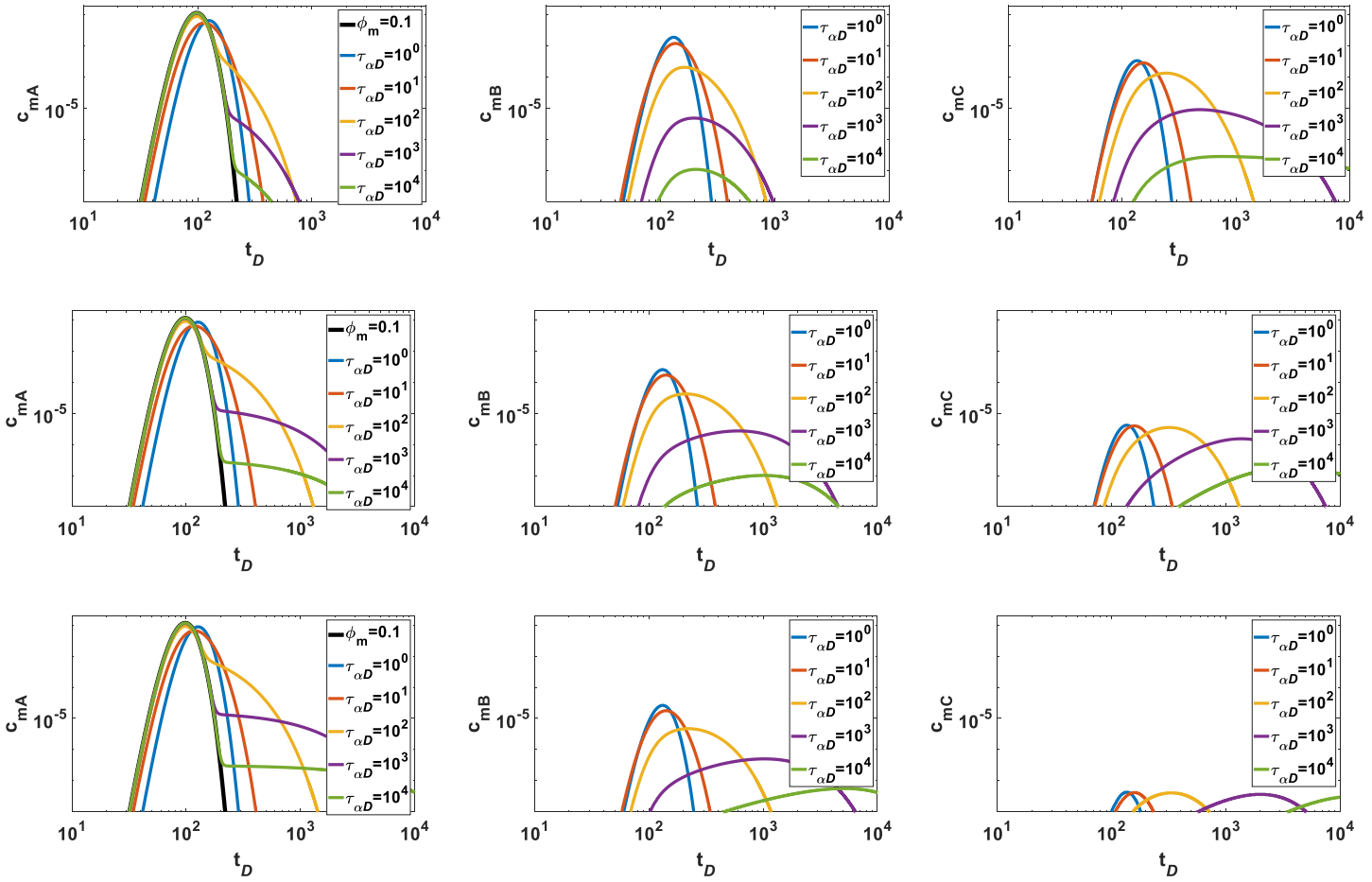

Figure C.1 Breakthrough curves of species A, B and C for $q_m = 1.0$ [LT^{-1}], thus $t_c = 0.1$ [T^{-1}], $\tau_{r1_D} = \tau_{r2_D} = 10^2$, 10^3 and 10^4 from top to bottom.

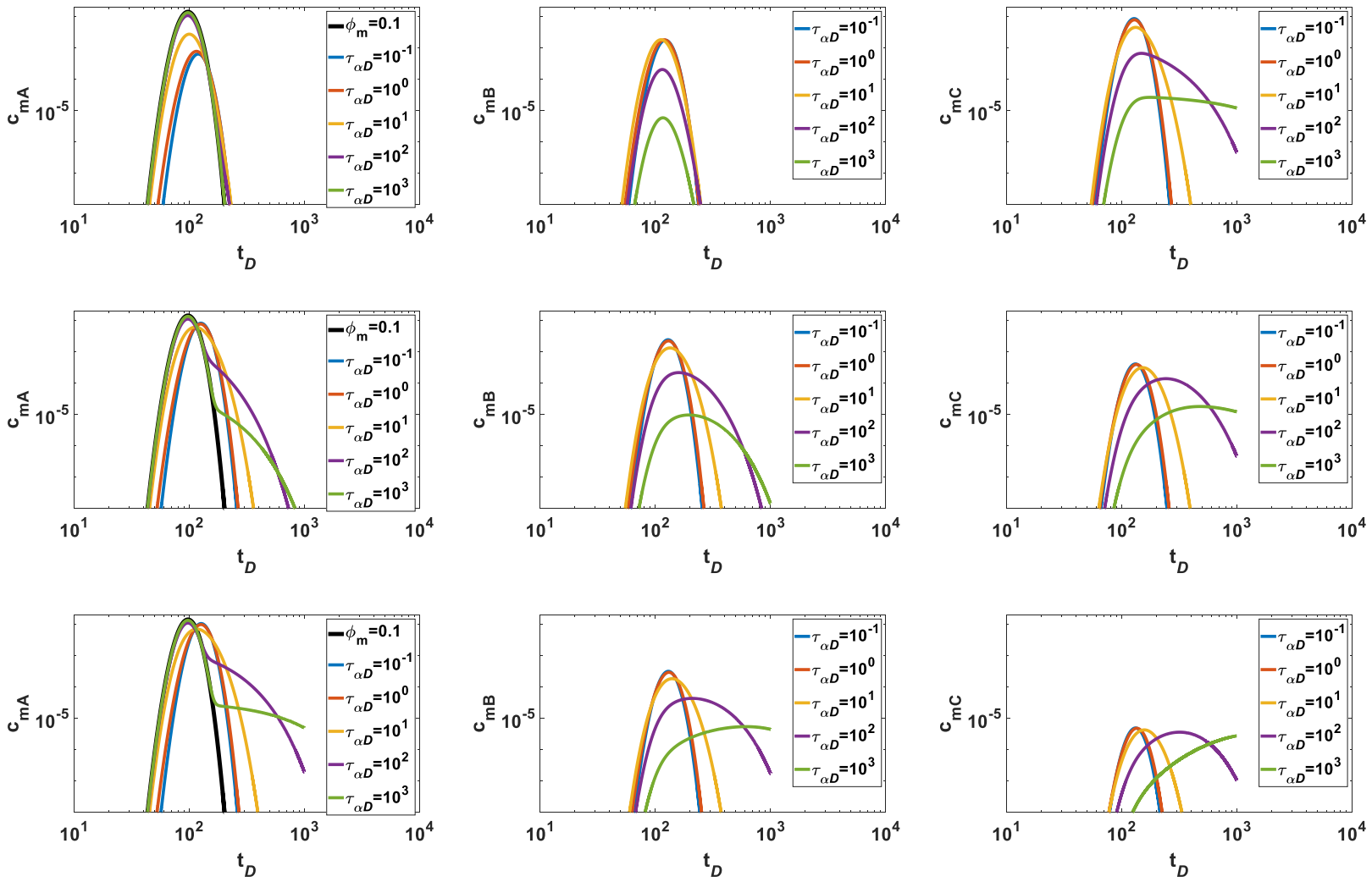

Figure C.2. Breakthrough curves of species A, B and C for $q_m = 0.1$ [LT^{-1}], thus $t_c = 1.0$ [T^{-1}], $\tau_{r1_D} = \tau_{r2_D} = 10^1$, 10^2 and 10^3 from top to bottom.

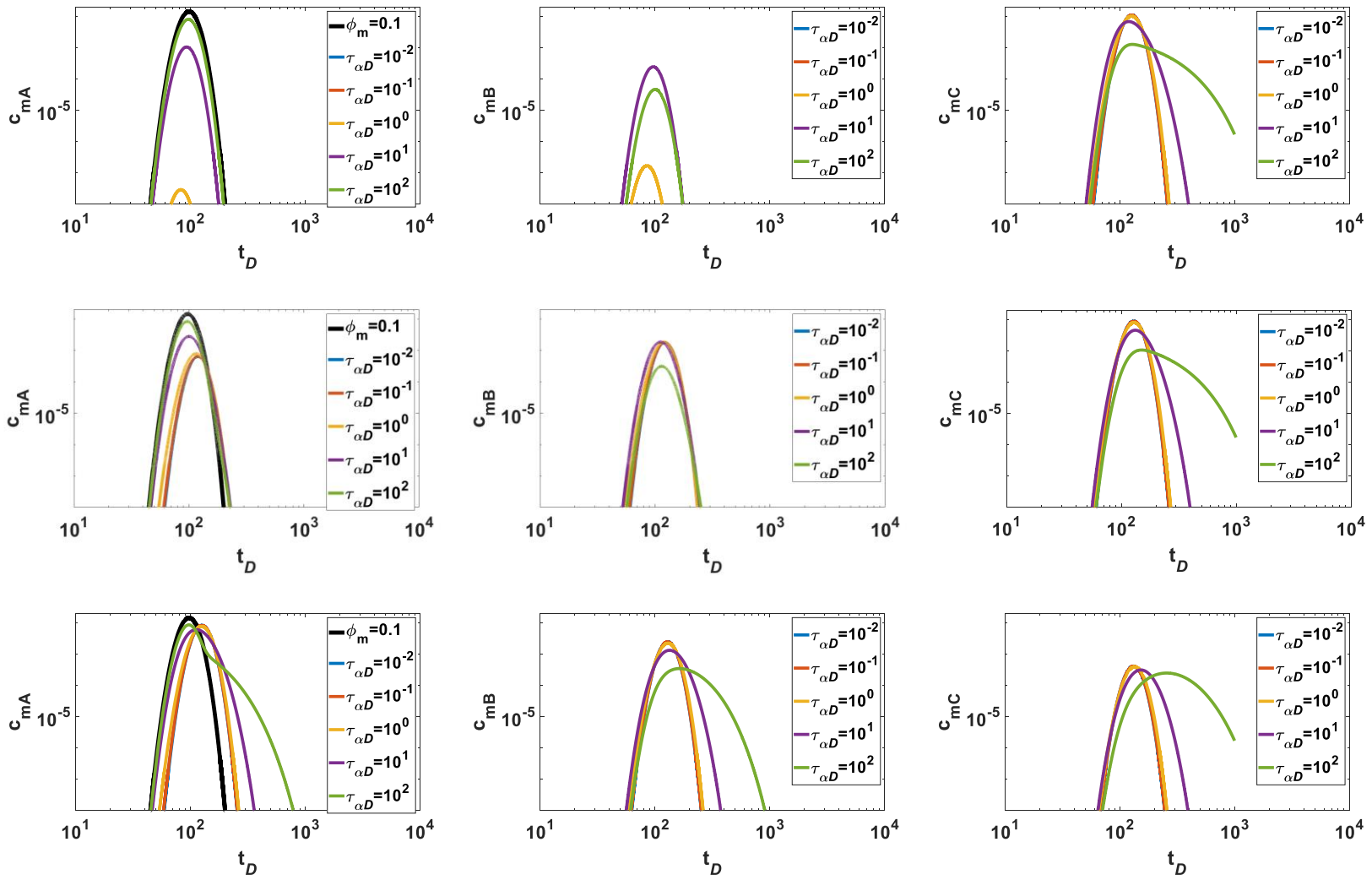

Figure C.3. Breakthrough curves of species A, B and C for $q_m = 0.01$ [LT^{-1}], thus $t_c = 10.0$ [T^{-1}], $\tau_{r1_D} = \tau_{r2_D} = 10^0$, 10^1 and 10^2 from top to bottom.

D. The relationship between the mass transfer rates and the volume fraction of immobile zones

The mass transfer rate coefficient, α_j, can be quantified by considering diffusion in the biofilm, that depends on its size and shape. In general, α_j, can be expressed as:

$$\alpha_j = D_b \frac{\sigma_b}{b\phi_{b,im,j}} \tag{D.1}$$

where D_b [L^2T^{-1}] is the diffusion coefficient of biofilm, σ_b [L^2L^{-3}] is the specific surface area of biofilm which is the surface area of biofilm divided by the total volume, b [L] is the size (thickness or radius) of biofilm, and $\phi_{b,im,j}$ is the fraction of the volume of biofilm over the total volume, which is expressed as

$$\phi_{b,im,j} = b\sigma_b \tag{D.2}$$

Various relations between α_j and $\phi_{b,im,j}$ can be deduced, depending on the stage of biofilm growth. For stage I (lateral growth) we assume b to be constant. The biofilm grows by increasing the specific surface area. Then the specific surface area of biofilm can be expressed as a function of the volume fraction of biofilm, that is

$$\sigma_b = \frac{\phi_{b,im,j}}{b} \tag{D.3}$$

Substituting equation (A3) into (A1) gives

$$\alpha_j = \frac{D_b}{b^2} \tag{D.4}$$

It shows that α_j is constant, which means $\alpha_j \propto \phi^0_{b,im,j}$ or $\tau_{\alpha_j} \propto \phi^0_{b,im,j}$.

For stage II (spherical growth), we assume the biofilm to consist of spheres and the number of spheres per total volume n to be constant. The biofilm grows by increasing the size of the spheres not their number. Then, the volume fraction and the specific surface of biofilm are given by

$$\phi_{b,im,j} = n\frac{4}{3}\pi b^3 \tag{D.5}$$

$$\sigma_b = n4\pi b^2 \tag{D.6}$$

According to equation (A5), the size of biofilm can be expressed as a function of n and $\phi_{b,im,j}$

$$b = \left(\frac{3\phi_{b,im,j}}{n4\pi}\right)^{1/3} \tag{D.7}$$

in which, n can be calculated from a referenced biofilm size b_{ref} and volume fraction $\phi_{b,ref}$

$$n = \frac{3\phi_{b,ref}}{4\pi b^3_{ref}} \tag{D.8}$$

Substituting equation (A6) into (A1), gives

$$\alpha_j = D_b \frac{n4\pi b}{\phi_{b,im,j}} \tag{D.9}$$

Then by substituting (A7) and (A8) into (A9), we obtain

$$\alpha_j = 3D_b \frac{1}{b_{ref}^2} \left(\frac{\phi_{b,ref}}{\phi_{b,im,j}} \right)^{2/3} \tag{D.10}$$

As D_b, b_{ref} and $\phi_{b,ref}$ are constant, $\alpha_j \propto {\phi_{b,im,j}}^{-2/3}$ or $\tau_{\alpha_j} \propto \phi_{b,im,j}^{2/3}$.

For stage III we assume σ_b to be constant. The biofilm grows by increasing the thickness of biofilm. Then the thickness of biofilm can be expressed as a function of the volume fraction of biofilm, that is

$$b = \frac{\phi_{b,im,j}}{\sigma_b} \tag{D.11}$$

Substituting equation (A11) into (A1), gives

$$\alpha_j = D_b \frac{\sigma_b^2}{\phi_{b,im,j}^2} \tag{D.12}$$

As D_b and σ_b are constants, $\alpha_j \propto \phi_{b,im,j}^{-2}$ or $\tau_{\alpha_j} \propto \phi_{b,im,j}^2$.

E. Publications and Conference presentations

Publications in scientific journals

Wang, J., Carrera, J. & Saaltink, M. W., (June 2021). On the localization of chemical reactions in multicontinuum media *Water*. In preparation for submission.

Wang, J., Carrera, J., Saaltink, M. W., & Valhondo, C., (October 2020). A general and efficient numerical solution of reactive transport with multirate msass transfer. *Computes & Geosciences*. Under second review, Manuscript number: CAGEO-D-20-00371R1.

Valhondo, C., Carrera, J., Martínez-Landa, L., Wang, J., Amalfitano, S., Levantesi, C., & Diaz-Cruz, M. S., (2020). Reactive barriers for renaturalization of reclaimed water during soil aquifer treatment. *Water (Switzerland)*. https://doi.org/10.3390/W12041012

Presentations in Conferences

Wang, J., Saaltink, M. W. & Carrera, J., Conceptual model of reactive transport incorporated with dynamic microbial growth in immobile biofilms. *InterPore 2021 online*, May 2021, Edinburgh, United Kingdom.

Wang, J., Carrera, J., Saaltink, M. W., Valhondo, C., Reactive Transport Modeling of Microbial-mediated degradation in MAR. *Goldschmidt*, August 2019, Barcelona, Spain.

Wang, J., Carrera, J., Saaltink, M. W., Valhondo, C. & Soler, J., An objective-oriented tool to model biogeochemical degradation of emerging organic contaminants in porous media. *EGU General Assembly*, April 2019, Vienna, Austria.

Presentations in Seminar

Wang, J., Carrera, J., Saaltink, M. W. A general and efficient numerical solution of reactive transport with multirate mass transfer. *GHS Seminar*, October 2020, Barcelona, Spain, oral presentation.

Wang, J., Carrera, J., Saaltink, M. W., Valhondo, C. Incorporate biofilm into reactive transport modeling in porous media. *GHS Seminar*, September 2019, Barcelona, Spain, oral presentation.

Bibliography

Adams, E. E., & Gelhar, L. W. (1992). Field study of dispersion in a heterogeneous aquifer: 2. Spatial moments analysis. *Water Resources Research*. https://doi.org/10.1029/92WR01757

Babaei, M., & Islam, A. (2018). Convective-Reactive CO2 Dissolution in Aquifers With Mass Transfer With Immobile Water. *Water Resources Research*. https://doi.org/10.1029/2018WR023150

Babey, T., de Dreuzy, J. R., & Casenave, C. (2015). Multi-Rate Mass Transfer (MRMT) models for general diffusive porosity structures. *Advances in Water Resources*. https://doi.org/10.1016/j.advwatres.2014.12.006

Bakke, R., Trulear, M. G., Robinson, J. A., & Characklis, W. G. (1984). Activity of Pseudomonas aeruginosa in biofilms: Steady state. *Biotechnology and Bioengineering*, *26*(12). https://doi.org/10.1002/bit.260261204

Bea, S. A., Carrera, J., Ayora, C., Batlle, F., & Saaltink, M. W. (2009). CHEPROO: A Fortran 90 object-oriented module to solve chemical processes in Earth Science models. *Computers and Geosciences*. https://doi.org/10.1016/j.cageo.2008.08.010

Beisman, J. J., Maxwell, R. M., Navarre-Sitchler, A. K., Steefel, C. I., & Molins, S. (2015). ParCrunchFlow: an efficient, parallel reactive transport simulation tool for physically and chemically heterogeneous saturated subsurface environments. *Computational Geosciences*. https://doi.org/10.1007/s10596-015-9475-x

Benson, D. A., & Meerschaert, M. M. (2009). A simple and efficient random walk solution of multi-rate mobile/immobile mass transport equations. *Advances in Water Resources*. https://doi.org/10.1016/j.advwatres.2009.01.002

Benson, D. A., Wheatcraft, S. W., & Meerschaert, M. M. (2000). The fractional-order governing equation of Levy motion. *Water Resources Research*. https://doi.org/10.1029/2000WR900032

Berkowitz, B., Cortis, A., Dentz, M., & Scher, H. (2006). Modeling Non-fickian transport in geological formations as a continuous time random walk. *Reviews of Geophysics*. https://doi.org/10.1029/2005RG000178

Berkowitz, B., Emmanuel, S., & Scher, H. (2008). Non-Fickian transport and multiple-rate mass transfer in porous media. *Water Resources Research*. https://doi.org/10.1029/2007WR005906

Berkowitz, B., & Scher, H. (1998). Theory of anomalous chemical transport in random fracture networks. *Physical Review E - Statistical Physics, Plasmas, Fluids, and Related Interdisciplinary Topics*. https://doi.org/10.1103/PhysRevE.57.5858

Berkowitz, B., & Scher, H. (2009). Exploring the nature of non-Fickian transport in laboratory experiments. *Advances in Water Resources*. https://doi.org/10.1016/j.advwatres.2008.05.004

Bilke, L., Flemisch, B., Kalbacher, T., Kolditz, O., Helmig, R., & Nagel, T. (2019). Development of Open-Source Porous Media Simulators: Principles and Experiences. *Transport in Porous Media*. https://doi.org/10.1007/s11242-019-01310-1

Brangarí, A. C., Fernàndez-Garcia, D., Sanchez-Vila, X., & Manzoni, S. (2018). Ecological and soil hydraulic implications of microbial responses to stress – A modeling analysis. *Advances in Water Resources*, *116*. https://doi.org/10.1016/j.advwatres.2017.11.005

Carles Brangarí, A., Sanchez-Vila, X., Freixa, A., M. Romaní, A., Rubol, S., & Fernàndez-Garcia, D. (2017). A mechanistic model (BCC-PSSICO) to predict changes in the hydraulic properties for bio-amended variably saturated soils. *Water Resources Research*, *53*(1). https://doi.org/10.1002/2015WR018517

Carrel, M., Morales, V. L., Dentz, M., Derlon, N., Morgenroth, E., & Holzner, M. (2018). Pore-Scale Hydrodynamics in a Progressively Bioclogged Three-Dimensional Porous Medium: 3-D Particle Tracking Experiments and Stochastic Transport Modeling. *Water Resources Research*, *54*(3). https://doi.org/10.1002/2017WR021726

Carrel, Maxence, Morales, V. L., Beltran, M. A., Derlon, N., Kaufmann, R., Morgenroth, E., & Holzner, M. (2018). Biofilms in 3D porous media: Delineating the influence of the pore network geometry, flow and mass transfer on biofilm development. *Water Research*, *134*. https://doi.org/10.1016/j.watres.2018.01.059

Carrera, J., Sánchez-Vila, X., Benet, I., Medina, A., Galarza, G., & Guinerà, J. (1998). On matrix diffusion: Formulations, solution methods and qualitative effects. *Hydrogeology Journal*. https://doi.org/10.1007/s100400050143

Chen-Charpentier, B. (1999). Numerical simulation of biofilm growth in porous media. *Journal of Computational and Applied Mathematics*. https://doi.org/10.1016/S0377-0427(98)00240-4

Christensen, T. H., Kjeldsen, P., Bjerg, P. L., Jensen, D. L., Christensen, J. B., Baun, A., Albrechtsen, H. J., & Heron, G. (2001). Biogeochemistry of landfill leachate plumes. In *Applied Geochemistry* (Vol. 16, Issues 7–8). https://doi.org/10.1016/S0883-2927(00)00082-2

Cirpka, O. A., Frind, E. O., & Helmig, R. (1999). Numerical simulation of biodegradation controlled by transverse mixing. *Journal of Contaminant Hydrology*, *40*(2). https://doi.org/10.1016/S0169-7722(99)00044-3

Cortis, A., & Berkowitz, B. (2004). Anomalous Transport in "Classical" Soil and Sand Columns. *Soil Science Society of America Journal*. https://doi.org/10.2136/sssaj2004.1539

Costerton, J. W., Lewandowski, Z., Caldwell, D. E., Korber, D. R., & Lappin-Scott, H. M. (1995). Microbial biofilms. In *Annual Review of Microbiology*. https://doi.org/10.1146/annurev.mi.49.100195.003431

Cunningham, A. B., Characklls, W. G., Abedeen, F., & Crawford, D. (1991). Influence of Biofilm Accumulation on Porous Media Hydrodynamics. *Environmental Science and Technology*. https://doi.org/10.1021/es00019a013

Cunningham, A. B., Sharp, R. R., Hiebert, R., & James, G. (2003). Subsurface biofilm barriers for the containment and remediation of contaminated groundwater. *Bioremediation Journal*. https://doi.org/10.1080/713607982

De Dreuzy, J. R., Rapaport, A., Babey, T., & Harmand, J. (2013). Influence of porosity structures on mixing-induced reactivity at chemical equilibrium in mobile/immobile Multi-Rate Mass Transfer (MRMT) and Multiple INteracting Continua (MINC) models. *Water Resources Research*. https://doi.org/10.1002/2013WR013808

De Dreuzy, Jean Raynald, & Carrera, J. (2016). On the validity of effective formulations for transport through heterogeneous porous media. *Hydrology and Earth System Sciences*. https://doi.org/10.5194/hess-20-1319-2016

Deng, H., & Spycher, N. (2019). Modeling reactive transport processes in fractures. *Reviews in Mineralogy and Geochemistry*, *85*(1). https://doi.org/10.2138/rmg.2019.85.3

Deng, W., Cardenas, M. B., Kirk, M. F., Altman, S. J., & Bennett, P. C. (2013). Effect of permeable biofilm on micro-and macro-scale flow and transport in bioclogged pores. *Environmental Science and Technology*. https://doi.org/10.1021/es402596v

Dentz, M., & Berkowitz, B. (2003). Transport behavior of a passive solute in continuous time random walks and multirate mass transfer. *Water Resources Research*. https://doi.org/10.1029/2001WR001163

Dentz, M., Cortis, A., Scher, H., & Berkowitz, B. (2004). Time behavior of solute transport in heterogeneous media: Transition from anomalous to normal transport. *Advances in Water Resources*. https://doi.org/10.1016/j.advwatres.2003.11.002

Dentz, M., Gouze, P., & Carrera, J. (2011). Effective non-local reaction kinetics for transport in physically and chemically heterogeneous media. *Journal of Contaminant Hydrology*. https://doi.org/10.1016/j.jconhyd.2010.06.002

Dentz, M., Kang, P. K., & Le Borgne, T. (2015). Continuous time random walks for non-local radial solute transport. *Advances in Water Resources*. https://doi.org/10.1016/j.advwatres.2015.04.005

Donado, L. D., Sanchez-Vila, X., Dentz, M., Carrera, J., & Bolster, D. (2009). Multicomponent reactive transport in multicontinuum media. *Water Resources Research*. https://doi.org/10.1029/2008WR006823

Eberl, H. J., Picioreanu, C., Heijnen, J. J., & Van Loosdrecht, M. C. M. (2000). Three-dimensional numerical study on the correlation of spatial structure, hydrodynamic conditions, and mass transfer and conversion in biofilms. *Chemical Engineering Science*. https://doi.org/10.1016/S0009-2509(00)00169-X

Esperanza Cortés, M., Consuegra Bonilla, J., & Dario Sinisterra, R. (2011). Biofilm formation, control and novel strategies for eradication. In *Science against microbial pathogens: communicating current research and technological advances*.

Fernàndez-Garcia, D., & Sanchez-Vila, X. (2015). Mathematical equivalence between time-dependent single-rate and multirate mass transfer models. *Water Resources Research*. https://doi.org/10.1002/2014WR016348

Flemming, H. C., Neu, T. R., & Wozniak, D. J. (2007). The EPS matrix: The "House of Biofilm Cells." In *Journal of Bacteriology*. https://doi.org/10.1128/JB.00858-07

Flemming, H. C., & Wingender, J. (2010). The biofilm matrix. In *Nature Reviews Microbiology*. https://doi.org/10.1038/nrmicro2415

Flemming, H. C., & Wuertz, S. (2019). Bacteria and archaea on Earth and their abundance in biofilms. *Nature Reviews Microbiology*, *17*(4). https://doi.org/10.1038/s41579-019-0158-9

Gaebler, H. J., & Eberl, H. J. (2018). A simple model of biofilm growth in a porous medium that accounts for detachment and attachment of suspended biomass and their contribution to substrate degradation. *European Journal of Applied Mathematics*, *29*(6). https://doi.org/10.1017/S0956792518000189

Gouze, P., Le Borgne, T., Leprovost, R., Lods, G., Poidras, T., & Pezard, P. (2008). Non-Fickian dispersion in porous media: 1. Multiscale measurements using single-well injection withdrawal tracer tests. *Water Resources Research*. https://doi.org/10.1029/2007WR006278

Gouze, Philippe, Melean, Y., Le Borgne, T., Dentz, M., & Carrera, J. (2008). Non-Fickian dispersion in porous media explained by heterogeneous microscale matrix diffusion. *Water Resources Research*. https://doi.org/10.1029/2007WR006690

Guimerà, J., & Carrera, J. (2000). A comparison of hydraulic and transport parameters measured in low- permeability fractured media. *Journal of Contaminant Hydrology*, *41*(3–4), 261–281. https://doi.org/10.1016/S0169-7722(99)00080-7

Haggerty, R., & Gorelick, S. M. (1995). Multiple-Rate Mass Transfer for Modeling Diffusion and Surface Reactions in Media with Pore-Scale Heterogeneity. *Water Resources Research*. https://doi.org/10.1029/95WR10583

Haggerty, R., Harvey, C. F., Von Schwerin, C. F., & Meigs, L. C. (2004). What controls the apparent timescale of solute mass transfer in aquifers and soils? A comparison of experimental results. *Water Resources Research*. https://doi.org/10.1029/2002WR001716

Haggerty, R., McKenna, S. A., & Meigs, L. C. (2000). On the late-time behavior of tracer test breakthrough curves. *Water Resources Research*. https://doi.org/10.1029/2000WR900214

Haggerty, R., Wondzell, S. M., & Johnson, M. A. (2002). Power-law residence time distribution in the hyporheic zone of a 2nd-order mountain stream. *Geophysical Research Letters*.

https://doi.org/10.1029/2002GL014743

Hammond, G. E., Lichtner, P. C., & Mills, R. T. (2014). Evaluating the performance of parallel subsurface simulators: An illustrative example with PFLOTRAN. *Water Resources Research*. https://doi.org/10.1002/2012WR013483

Iraola, A., Trinchero, P., Karra, S., & Molinero, J. (2019). Assessing dual continuum method for multicomponent reactive transport. *Computers and Geosciences*. https://doi.org/10.1016/j.cageo.2019.05.007

Kapellos, G. E., Alexiou, T. S., & Pavlou, S. (2015). Fluid-Biofilm Interactions in Porous Media. In *Heat Transfer and Fluid Flow in Biological Processes*. https://doi.org/10.1016/B978-0-12-408077-5.00008-0

Kim, J. W., Choi, H., & Pachepsky, Y. A. (2010). Biofilm morphology as related to the porous media clogging. *Water Research*. https://doi.org/10.1016/j.watres.2009.05.049

Kitanidis, P. K. (1988). Prediction by the method of moments of transport in a heterogeneous formation. *Journal of Hydrology*. https://doi.org/10.1016/0022-1694(88)90111-4

Kolditz, O., Bauer, S., Bilke, L., Böttcher, N., Delfs, J. O., Fischer, T., Görke, U. J., Kalbacher, T., Kosakowski, G., McDermott, C. I., Park, C. H., Radu, F., Rink, K., Shao, H., Shao, H. B., Sun, F., Sun, Y. Y., Singh, A. K., Taron, J., … Zehner, B. (2012). OpenGeoSys: An open-source initiative for numerical simulation of thermo-hydro-mechanical/chemical (THM/C) processes in porous media. *Environmental Earth Sciences*. https://doi.org/10.1007/s12665-012-1546-x

Kolditz, Olaf, Görke, U.-J., Shao, H., & Wang, W. (2012). Thermo-Hydro-Mechanical-Chemical Processes in Porous Media: Benchmarks and Examples. In *Springer*.

Kone, T., Golfier, F., Orgogozo, L., Oltéan, C., Lefèvre, E., Block, J. C., & Buès, M. A. (2014). Impact of biofilm-induced heterogeneities on solute transport in porous media. *Water Resources Research*. https://doi.org/10.1002/2013WR015213

Kosakowski, G., Berkowitz, B., & Scher, H. (2001). Analysis of field observations of tracer transport in a fractured till. *Journal of Contaminant Hydrology*. https://doi.org/10.1016/S0169-7722(00)00140-6

Le Borgne, T., & Gouze, P. (2008). Non-Fickian dispersion in porous media: 2. Model validation from measurements at different scales. *Water Resources Research*. https://doi.org/10.1029/2007WR006279

Le Borgne, Tanguy, Dentz, M., & Carrera, J. (2008). Lagrangian statistical model for transport in highly heterogeneous velocity fields. *Physical Review Letters*, *101*(9). https://doi.org/10.1103/PhysRevLett.101.090601

Levy, M., & Berkowitz, B. (2003). Measurement and analysis of non-Fickian dispersion in heterogeneous porous media. *Journal of Contaminant Hydrology*. https://doi.org/10.1016/S0169-7722(02)00204-8

Lewandowski, Z., & Boltz, J. P. (2011). Biofilms in Water and Wastewater Treatment. In *Treatise on Water Science*. https://doi.org/10.1016/B978-0-444-53199-5.00095-6

Liu, P., Zhang, T., & Sun, S. (2019). A tutorial review of reactive transport modeling and risk assessment for geologic CO 2 sequestration. In *Computers and Geosciences*. https://doi.org/10.1016/j.cageo.2019.02.007

Lopez-Peña, L. A., Meulenbroek, B., & Vermolen, F. (2019). A network model for the biofilm growth in porous media and its effects on permeability and porosity. *Computing and Visualization in Science*, *21*(1–6). https://doi.org/10.1007/s00791-019-00316-y

Marseguerra, M., & Zoia, A. (2008). Monte Carlo evaluation of FADE approach to anomalous kinetics. *Mathematics and Computers in Simulation*. https://doi.org/10.1016/j.matcom.2007.03.001

Meysman, F. J. R., Middelburg, J. J., Herman, P. M. J., & Heip, C. H. R. (2003a). Reactive transport in

surface sediments. I. Model complexity and software quality. *Computers and Geosciences*. https://doi.org/10.1016/S0098-3004(03)00006-2

Meysman, F. J. R., Middelburg, J. J., Herman, P. M. J., & Heip, C. H. R. (2003b). Reactive transport in surface sediments. II. Media: an object-oriented problem-solving environment for early diagenesis. *Computers & Geosciences*. https://doi.org/10.1016/s0098-3004(03)00007-4

Molins, S., Carrera, J., Ayora, C., & Saaltink, M. W. (2004). A formulation for decoupling components in reactive transport problems. *Water Resources Research*. https://doi.org/10.1029/2003WR002970

Morales, V. L., Parlange, J. Y., & Steenhuis, T. S. (2010). Are preferential flow paths perpetuated by microbial activity in the soil matrix? A review. *Journal of Hydrology*, *393*(1–2). https://doi.org/10.1016/j.jhydrol.2009.12.048

Neuman, S. P., & Tartakovsky, D. M. (2009). Perspective on theories of non-Fickian transport in heterogeneous media. *Advances in Water Resources*. https://doi.org/10.1016/j.advwatres.2008.08.005

Nicolella, C., Van Loosdrecht, M. C. M., & Heijnen, J. J. (2000). Wastewater treatment with particulate biofilm reactors. In *Journal of Biotechnology*. https://doi.org/10.1016/S0168-1656(00)00229-7

Nordström, A., Hellman, M., Hallin, S., & Herbert, R. B. (2021). Microbial controls on net production of nitrous oxide in a denitrifying woodchip bioreactor. *Journal of Environmental Quality*, *50*(1). https://doi.org/10.1002/jeq2.20181

Nordström, A., & Herbert, R. B. (2017). Denitrification in a low-temperature bioreactor system at two different hydraulic residence times: laboratory column studies. *Environmental Technology (United Kingdom)*. https://doi.org/10.1080/09593330.2016.1228699

Nordström, A., & Herbert, R. B. (2018). Determination of major biogeochemical processes in a denitrifying woodchip bioreactor for treating mine drainage. *Ecological Engineering*, *110*. https://doi.org/10.1016/j.ecoleng.2017.09.018

Nordström, A., & Herbert, R. B. (2019). Identification of the temporal control on nitrate removal rate variability in a denitrifying woodchip bioreactor. *Ecological Engineering*, *127*. https://doi.org/10.1016/j.ecoleng.2018.11.015

Parkhurst, D. L., & Appelo, C. A. J. (2013). Description of Input and Examples for PHREEQC Version 3 — A Computer Program for Speciation , Batch-Reaction , One-Dimensional Transport , and Inverse Geochemical Calculations. In *U.S. Geological Survey Techniques and Methods, book 6, chapter A43*.

Picioreanu, C., Kreft, J. U., & Van Loosdrecht, M. C. M. (2004). Particle-based multidimensional multispecies biofilm model. *Applied and Environmental Microbiology*. https://doi.org/10.1128/AEM.70.5.3024-3040.2004

Picioreanu, C., Van Loosdrecht, M. C. M., & Heijnen, J. J. (1998). Mathematical modeling of biofilm structure with a hybrid differential- discrete cellular automaton approach. *Biotechnology and Bioengineering*, *58*(1), 101–116. https://doi.org/10.1002/(SICI)1097-0290(19980405)58:1<101::AID-BIT11>3.0.CO;2-M

Prommer, H., Barry, D. A., & Zheng, C. (2003). MODFLOW/MT3DMS-based reactive multicomponent transport modeling. *Ground Water*. https://doi.org/10.1111/j.1745-6584.2003.tb02588.x

Prommer, H., Barry, D., & Zheng, C. (2001). PHT3D-A MODFLOW/MT3DMS based reactive multi-component transport model. *MODFLOW 2001 and Other Modeling Odysseys*.

Pruess, K., & Narasimhan, T. N. (1985). PRACTICAL METHOD FOR MODELING FLUID AND HEAT FLOW IN FRACTURED POROUS MEDIA. *Society of Petroleum Engineers Journal*.

Raiders, R. A., Knapp, R. M., & McInerney, M. J. (1989). Microbial selective plugging and enhanced

oil recovery. *Journal of Industrial Microbiology*. https://doi.org/10.1007/BF01574079

Rapaport, A., Rojas-Palma, A., De Dreuzy, J. R., & Ramirez, H. C. (2017). Equivalence of Finite Dimensional Input-Output Models of Solute Transport and Diffusion in Geosciences. *IEEE Transactions on Automatic Control*. https://doi.org/10.1109/TAC.2017.2701150

Rittmann, B. E., & McCarty, P. L. (2001). Environmental biotechnology : principles and applications. *Current Opinion in Biotechnology*, *7*(3).

Rodríguez-Escales, P., Folch, A., van Breukelen, B. M., Vidal-Gavilan, G., & Sanchez-Vila, X. (2016). Modeling long term Enhanced in situ Biodenitrification and induced heterogeneity in column experiments under different feeding strategies. *Journal of Hydrology*, *538*. https://doi.org/10.1016/j.jhydrol.2016.04.012

Saaltink, M. W., Batlle, F., Ayora, C., Carrera, J., & Olivella, S. (2004). RETRASO, a code for modeling reactive transport in saturated and unsaturated porous media. *Geologica Acta*. https://doi.org/10.1344/105.000001430

Saaltink, Maarten W., Ayora, C., & Carrera, J. (1998). A mathematical formulation for reactive transport that eliminates mineral concentrations. *Water Resources Research*. https://doi.org/10.1029/98WR00552

Saaltink, Maarten W., Carrera, J., & Ayora, C. (2001). On the behavior of approaches to simulate reactive transport. *Journal of Contaminant Hydrology*. https://doi.org/10.1016/S0169-7722(00)00172-8

Salamon, P., Fernàndez-Garcia, D., & Gómez-Hernández, J. J. (2006). Modeling mass transfer processes using random walk particle tracking. *Water Resources Research*. https://doi.org/10.1029/2006WR004927

Satpathy, S., Sen, S. K., Pattanaik, S., & Raut, S. (2016). Review on bacterial biofilm: An universal cause of contamination. In *Biocatalysis and Agricultural Biotechnology*. https://doi.org/10.1016/j.bcab.2016.05.002

Schumer, R., Benson, D. A., Meerschaert, M. M., & Baeumer, B. (2003). Fractal mobile/immobile solute transport. *Water Resources Research*. https://doi.org/10.1029/2003WR002141

Seifert, D., & Engesgaard, P. (2007). Use of tracer tests to investigate changes in flow and transport properties due to bioclogging of porous media. *Journal of Contaminant Hydrology*, *93*(1–4). https://doi.org/10.1016/j.jconhyd.2007.01.014

Sethi, R., & Di Molfetta, A. (2019). Remediation of Contaminated Groundwater. In *Springer Tracts in Civil Engineering*. https://doi.org/10.1007/978-3-030-20516-4_17

Shafahi, M., & Vafai, K. (2009). Biofilm affected characteristics of porous structures. *International Journal of Heat and Mass Transfer*. https://doi.org/10.1016/j.ijheatmasstransfer.2008.07.013

Silva, O., Carrera, J., Dentz, M., Kumar, S., Alcolea, A., & Willmann, M. (2009). A general real-time formulation for multi-rate mass transfer problems. *Hydrology and Earth System Sciences*. https://doi.org/10.5194/hess-13-1399-2009

Soler-Sagarra, J., Luquot, L., Martínez-Pérez, L., Saaltink, M. W., De Gaspari, F., & Carrera, J. (2016). Simulation of chemical reaction localization using a multi-porosity reactive transport approach. *International Journal of Greenhouse Gas Control*. https://doi.org/10.1016/j.ijggc.2016.01.026

Steefel, C. I., Appelo, C. A. J., Arora, B., Jacques, D., Kalbacher, T., Kolditz, O., Lagneau, V., Lichtner, P. C., Mayer, K. U., Meeussen, J. C. L., Molins, S., Moulton, D., Shao, H., Šimůnek, J., Spycher, N., Yabusaki, S. B., & Yeh, G. T. (2015). Reactive transport codes for subsurface environmental simulation. *Computational Geosciences*. https://doi.org/10.1007/s10596-014-9443-x

Steefel, C. I., & Lasaga, A. C. (1994). A coupled model for transport of multiple chemical species and kinetic precipitation/dissolution reactions with application to reactive flow in single phase hydrothermal systems. *American Journal of Science*. https://doi.org/10.2475/ajs.294.5.529

Steefel, Carl I., & MacQuarrie, K. T. B. (1996). Approaches to modeling of reactive transport in porous media. *Reviews in Mineralogy*, *34*.

Taylor, S. W., & Jaffé, P. R. (1990a). Biofilm growth and the related changes in the physical properties of a porous medium: 1. Experimental investigation. *Water Resources Research*. https://doi.org/10.1029/WR026i009p02153

Taylor, S. W., & Jaffé, P. R. (1990b). Biofilm growth and the related changes in the physical properties of a porous medium: 3. Dispersivity and model verification. *Water Resources Research*. https://doi.org/10.1029/WR026i009p02171

Taylor, S. W., Milly, P. C. D., & Jaffé, P. R. (1990). Biofilm growth and the related changes in the physical properties of a porous medium: 2. Permeability. *Water Resources Research*. https://doi.org/10.1029/WR026i009p02161

Thullner, M. (2010). Comparison of bioclogging effects in saturated porous media within one- and two-dimensional flow systems. *Ecological Engineering*. https://doi.org/10.1016/j.ecoleng.2008.12.037

Tiwari, S. K., & Bowers, K. L. (2001). Modeling biofilm growth for porous media applications. *Mathematical and Computer Modelling*, *33*(1–3). https://doi.org/10.1016/S0895-7177(00)00246-6

Valhondo, C., Carrera, J., Martínez-Landa, L., Wang, J., Amalfitano, S., Levantesi, C., & Diaz-Cruz, M. S. (2020). Reactive barriers for renaturalization of reclaimed water during soil aquifer treatment. *Water (Switzerland)*. https://doi.org/10.3390/W12041012

Valhondo, C., Martinez-Landa, L., Carrera, J., Ayora, C., Nödler, K., & Licha, T. (2018). Evaluation of EOC removal processes during artificial recharge through a reactive barrier. *Science of the Total Environment*, *612*. https://doi.org/10.1016/j.scitotenv.2017.08.054

Valhondo, C., Martínez-Landa, L., Carrera, J., Díaz-Cruz, S. M., Amalfitano, S., & Levantesi, C. (2020). Six artificial recharge pilot replicates to gain insight into water quality enhancement processes. *Chemosphere*, *240*. https://doi.org/10.1016/j.chemosphere.2019.124826

Valocchi, A. J. (1985). Validity of the Local Equilibrium Assumption for Modeling Sorbing Solute Transport Through Homogeneous Soils. *Water Resources Research*. https://doi.org/10.1029/WR021i006p00808

Van Hamme, J. D., Singh, A., & Ward, O. P. (2003). Recent Advances in Petroleum Microbiology. *Microbiology and Molecular Biology Reviews*. https://doi.org/10.1128/mmbr.67.4.503-549.2003

Von Der Schulenburg, D. A. G., Pintelon, T. R. R., Picioreanu, C., Van Loosdrecht, M. C. M., & Johns, M. L. (2009). Three-dimensional simulations of biofilm growth in porous media. *AIChE Journal*. https://doi.org/10.1002/aic.11674

Wang, P. P., Zheng, C., & Gorelick, S. M. (2005). A general approach to advective-dispersive transport with multirate mass transfer. *Advances in Water Resources*. https://doi.org/10.1016/j.advwatres.2004.10.003

Willmann, M., Carrera, J., & Sánchez-Vila, X. (2008). Transport upscaling in heterogeneous aquifers: What physical parameters control memory functions? *Water Resources Research*. https://doi.org/10.1029/2007WR006531

Willmann, M., Carrera, J., Sanchez-Vila, X., Silva, O., & Dentz, M. (2010). Coupling of mass transfer and reactive transport for nonlinear reactions in heterogeneous media. *Water Resources Research*. https://doi.org/10.1029/2009WR007739

Wu, Y., Cai, P., Jing, X., Niu, X., Ji, D., Ashry, N. M., Gao, C., & Huang, Q. (2019). Soil biofilm formation enhances microbial community diversity and metabolic activity. *Environment International*, *132*. https://doi.org/10.1016/j.envint.2019.105116

Zhang, Y., Benson, D. A., & Baeumer, B. (2007). Predicting the tails of breakthrough curves in

regional-scale alluvial systems. *Ground Water*. https://doi.org/10.1111/j.1745-6584.2007.00320.x

Zinn, B., Meigs, L. C., Harvey, C. F., Haggerty, R., Peplinski, W. J., & Von Schwerin, C. F. (2004). Experimental visualization of solute transport and mass transfer processes in two-dimensional conductivity fields with connected regions of high conductivity. *Environmental Science and Technology*. https://doi.org/10.1021/es034958g